Universidade de Aveiro Departamento de Química
2010

Patrícia Ferreira Lito

Caracterização de Novas Membranas de Titanossilicatos Microporosos por Ensaios de Permeabilidade

Universidade de Aveiro Departamento de Química
2010

Patrícia Ferreira Lito

Caracterização de Novas Membranas de Titanossilicatos Microporosos por Ensaios de Permeabilidade

Dissertação apresentada à Universidade de Aveiro para cumprimento dos requisitos necessários à obtenção do grau de Doutor em Engenharia Química, realizada sob a orientação científica do Doutor Carlos Manuel Santos da Silva, Professor Auxiliar do Departamento de Química da Universidade de Aveiro

Apoio financeiro da FCT e do FSE no âmbito do III Quadro Comunitário de Apoio.

Dedico este trabalho à minha irmã e aos meus pais pelo incansável apoio.

o júri

Presidente	Professor João Manuel Nunes Torrão Professor Catedrático da Universidade de Aveiro
Vogais	Professor João Paulo Serejo Goulão Crespo Professor Catedrático da Faculdade de Ciências e Tecnologia da Universidade Nova de Lisboa
	Professor José Joaquim Costa Cruz Pinto Professor Catedrático da Universidade de Aveiro
	Professor João Carlos Matias Celestino Gomes da Rocha Professor Catedrático da Universidade de Aveiro
	Prof[a]. Doutora Alexandra Maria Pinheiro da Silva Ferreira Rodrigues Pinto Professora Associada da Faculdade de Engenharia da Universidade do Porto
	Prof. Doutor Carlos Manuel Santos da Silva Professor Auxiliar da Universidade de Aveiro (orientador)

agradecimentos

Desejo expressar o meu profundo agradecimento a todas as pessoas que, directa ou indirectamente, contribuíram para a realização deste trabalho, em especial:

Ao meu orientador, Doutor Carlos Manuel Silva, pela preciosa orientação científica, pela disponibilidade e apoio incondicional e amizade prestados ao longo da realização deste trabalho.

Ao Doutor Francisco Avelino Silva, pelo apoio e disponibilidade que sempre me demonstrou, bem como pela sua contagiante boa disposição.

À Doutora Ana Sofia Santiago, pela ajuda incondicional, apoio, força, motivação e amizade fundamentais para a conclusão deste trabalho.

À Engenheira Ana Luísa Magalhães e ao Engenheiro Rui Silva pela amizade e incansável ajuda que muito contribuiu para a realização deste trabalho.

A todos os meus colegas, em especial à Doutora Cláudia Passos, por todo o seu apoio e amizade demonstrados.

Ao Professor João Rocha e ao Doutor Zhi Lin, pela colaboração na discussão de resultados, essencial ao desenvolvimento deste trabalho, e pela síntese das membranas estudadas,.

À FCT, pelo apoio financeiro que tornou possível a realização desta tese, através da bolsa SFRH/BD/25580/2006.

Finalmente, um agradecimento muito especial aos meus queridos pais e irmã pelo apoio incondicional, incentivo, paciência e compreensão, carinho e força que sempre me desmonstraram.

A todos, os meus sinceros agradecimentos.

palavras-chave

Membranas, Titanossilicatos, Permeação Gasosa, Mecanismos de Transporte, Maxwell-Stefan, Modelação, Permuta Iónica.

Resumo

O interesse crescente das membranas inorgânicas deve-se à potencial aplicação em novas áreas de investigação e da indústria, e em alternativa a operações mais convencionais. Em particular, as membranas de titanossilicatos oferecem vantagens importantes sobre as de zeólitos, pois podem ser sintetizadas sem agentes estruturantes orgânicos, para evitar a calcinação subsequente usualmente responsável por defeitos irreversíveis, exibem novas possibilidades de substituição isomórfica da matriz, permitindo um ajuste mais fino das propriedades catalíticas e de adsorção, e são capazes de separar misturas com base em diferenças de afinidade e tamanho molecular (efeito de peneiro).

Os objectivos principais deste trabalho foram: i) a caracterização dinâmica de membranas do tipo zeolítico sintetizadas no Laboratório Associado CICECO, realizando-se experiências de permeação com gases puros e misturas; ii) o desenvolvimento e validação de novos modelos para a transferência de massa multicomponente através de membranas porosas pela abordagem de Maxwell-Stefan, tendo em conta os mecanismos específicos encontrados, particularmente a contribuição por difusão superficial; e iii) a modelação dos pontos experimentais medidos, bem como dados compilados da literatura.

De forma a realizar os ensaios de permeação, desenhou-se, montou-se e testou-se uma instalação experimental. Para gases puros, os objectivos principais foram a medição de permeâncias a temperatura constante, por variação da pressão transmembranar (ΔP), e de permeâncias a temperatura programada, conduzidas a ΔP constante. Seguidamente, calcularam-se as selectividades ideais. Em relação a misturas, a determinação de selectividades reais requer as fracções molares no permeado e no retido. Na globalidade, estudaram-se três suportes diferentes (aço inoxidável e $\alpha-$alumina) e dezanove membranas de AM-3, ETS-10, ZSM-5 e zeólito 4A, utilizando-se H_2, He, N_2, CO_2, e O_2. A primeira avaliação exploratória da qualidade das membranas foi feita permeando azoto à temperatura ambiente. Assim, permeâncias superiores a 10^{-6} mol/m^{2}s.Pa evidenciavam defeitos grosseiros, levando-nos a efectuar cristalizações adicionais sobre as primeiras camadas. Este procedimento foi implementado com oito membranas. Um trabalho experimental mais detalhado foi conduzido com cinco membranas.

Membranas com curvas permeância-temperatura ($\Pi - T$) decrescentes indicam tipicamente transporte viscoso e de Knudsen, i.e. meso e macrodefeitos. Por exemplo, a membrana nº 3 de AM-3 exibiu este comportamento com H_2, He, N_2 e CO_2 puros. A contribuição de Knudsen foi confirmada pela relação linear encontrada entre as permeâncias e o inverso da raiz quadrada da massa molar. O mecanismo viscoso foi também identificado, pois as permeâncias eram inversamente proporcionais à viscosidade do gás ou, atendendo a equações do tipo de Chapman-Enskog, directamente proporcionais a $d_k^2/M^{0.5}$ (onde d_k é o diâmetro cinético e M a massa molar).

Um comportamento de permeação distinto observou-se com a membrana nº 5 de AM-3. As permeâncias registadas a temperatura programada eram aproximadamente constantes para o N_2, CO_2 e O_2, enquanto com o H_2 cresciam significativamente. Conjuntamente elas evidenciam a ocorrência de macro, meso e microdefeitos intercristalinos. O transporte gasoso activado através dos microporos compensa o impacto diminuidor dos meso e macroporos. Ao contrário do N_2, CO_2 e O_2, o pequeno diâmetro do hidrogénio torna-lhe possível permear através dos microporos intracristalinos, o que lhe adiciona um mecanismo de transferência responsável por esse crescimento.

No que respeita à difusão superficial, o sistema CO_2/ZSM-5 pode ser tomado como um exemplo paradigmático. Uma vez que este zeólito adsorve o CO_2, as permeâncias diminuem com o crescimento de ΔP, em virtude de as concentrações no sólido aumentarem de forma não linear e tenderem para a saturação. Os resultados contrastantes obtidos com azoto realçam ainda mais o mecanismo superficial, pois o N_2 não é adsorvido e as permeâncias medidas são constantes.

Globalmente, as selectividades ideais calculadas (α^*) variam de cerca de 1 a 4.2. Este parâmetro foi também utilizado para discriminar as melhores membranas, uma vez que baixos valores de α^* denotam o escoamento viscoso não-selectivo típico de macrodefeitos. Por exemplo, o H_2/CO_2 na membrana nº 3 de AM-3 apresentou $\alpha^* = 3.6 - 4.2$ para 40–120ºC, enquanto que na membrana nº 5 de AM-3 originou $\alpha^* = 2.6 - 3.1$. Estes resultados corroboraram as observações anteriores, segundo as quais a membrana nº 5 era melhor do que a nº 3. Alguns ensaios foram realizados com membranas saturadas com água para aumentar a selectividade: as medições mostraram claramente uma melhoria inicial seguida de uma redução consistente de α^* com o aumento da temperatura, devido à remoção das moléculas de água responsáveis pela obstrução de alguns poros. Em relação às selectividades reais de misturas contendo hidrogénio, devem ser realizadas mais experiências e a quantificação do hidrogénio deve ser melhorada.

No que concerne à modelação, novos factores termodinâmicos de Maxwell-Stefan foram derivados para as isotérmicas mono e multicomponente de Nitta, Langmuir-Freundlich e Toth, tendo sido testadas com dados de equilíbrio e de permeação da literatura. (É importante realçar que só estão publicadas equações para Langmuir e Dual-Site Langmuir de componentes puros e misturas). O procedimento de validação adoptado foi exigente: i) as isotérmicas multicomponente foram previstas a partir das de gás puro; ii) os parâmetros de difusão dos componentes puros foram ajustados a dados de permeação de cada gás; iii) depois, as difusividades cruzadas de Maxwell-Stefan foram estimadas pela relação de Vignes; finalmente, v) as novas equações foram testadas usando-se estes parâmetros, tendo sido capazes de estimar com sucesso fluxos binários.

Paralelamente ao enfoque principal do trabalho, derivou-se um novo modelo para permuta iónica em materiais microporosos baseado nas equações de Maxwell-Stefan. Este foi validado com dados experimentais de remoção de Hg^{2+} e Cd^{2+} de soluções aquosas usando ETS-4. A sua capacidade preditiva foi também avaliada, sendo possível concluir que se comporta muito bem. Com efeito, conseguiram-se boas previsões com parâmetros optimizados a partir de conjuntos de dados independentes. Este comportamento pode ser atribuído aos princípios físicos sólidos da teoria de Maxwell-Stefan.

keywords Membranes, Titanosilicates, Gas Permeation, Transport Mechanisms, Maxwell-Stefan, Modelling, Ion Exchange.

Abstract

The growing interest on inorganic membrane applications is due to their potential in new industrial and research fields, and as alternative processes to more conventional operations. In particular, titanosilicate membranes offer important benefits over the classical zeolite ones, since they may be synthesised without organic templates, to avoid the subsequent calcination usually responsible for irreversible defects, exhibit novel possibilities of isomorphous framework substitution, allowing for fine-tuning catalytic and adsorption properties, and are able to separate mixtures based on differences in affinity and sieving effect.

The main objectives of this work were: i) the dynamic characterization of the zeolite type membranes synthesised in our Associated Laboratory CICECO, by carrying out permeation experiments with pure gases and mixtures; ii) the development and validation of new models for the multicomponent mass transport across porous membranes by Maxwell-Stefan approach, taking into account the specific mechanisms found, particularly the surface diffusion contribution; and iii) modelling the experimental points measured, as well as data compiled from literature.

In order to carry out the permeation essays, an experimental set-up has been designed, assembled, and tested. For pure gases, the main targets were the measurement of permeances at constant temperature, by varying the transmembrane pressure drop (ΔP), and permeances at programmed temperature, by fixing ΔP. After that, the ideal selectivites were computed. With respect to mixtures, the determination of the real selectivities demanded the mole fractions in permeate and retentate. In the whole, three distinct supports (stainless-steel and α-alumina) and nineteen membranes of AM-3, ETS-10, ZSM-5, and zeolite 4A have been studied, employing H_2, He, N_2, CO_2, and O_2. The first exploratory evaluation of membrane quality was accomplished by permeating nitrogen at room temperature. Accordingly, permeances higher than 10^{-6} mol/m^{2}s.Pa pointed out rough defects, inducing us to perform additional crystallizations over the first layers. This procedure has been implemented with eight membranes. The more detailed experimental programme was carried out with five membranes.

Membranes with decreasing permeance-temperature ($\Pi - T$) curves indicate typically transport by Knudsen and viscous flows, i.e. meso and macrodefects. For instance, the AM-3 membrane number 3 exhibited such behaviour with pure H_2, He, N_2, and CO_2. The Knudsen contribution was confirmed by the linear trend found between permeances and the inverse of the square root of the molecular weights. The viscous mechanism was also identified, since permeances were inversely proportional to gas viscosity or, attending to Chapman-Enskog based equations, directly proportional to $d_k^2/M^{0.5}$ (where d_k is the kinetic diameter and M the molecular weight).

A dissimilar permeation behaviour observed in this work involved AM-3 membrane number 5. The registered permeances at programmed temperature were approximately constant for N_2, CO_2 and O_2, while for H_2 increases significantly. In conjunction they evidence the simultaneous incidence of macro, meso and intercrystalline microdefects. The activated gaseous transport across micropores compensates the lowering impact of meso and macropores. In contrast to N_2, CO_2 and O_2, the small hydrogen diameter makes it possible to permeate through the intracrystalline micropores, which superimposes an additional transfer mechanism responsible for such increasing.

With respect to surface diffusion, the CO_2/ZSM-5 system may be taken as a paradigmatic example. Once this zeolite adsorbs CO_2 the permeances decrease with increasing ΔP, because the surface loading concentrations increase non-linearly tending to the saturation. The contrasting results obtained for nitrogen emphasizes even more this mechanism, since N_2 does not adsorb and exhibited constant permeances.

Globally, the calculated ideal selectivites (α^*) ranged from ca. 1 to 4.2. This parameter was also utilized to discriminate the best membranes, since low values denote the non-selective viscous flow typical of macrodefects. For instance, H_2/CO_2 in AM-3 membrane No 3 presented $\alpha^* = 3.6 - 4.2$ for 40–120ºC, while in AM-3 No 5 originated $\alpha^* = 2.6 - 3.1$. These results corroborated previous findings that AM-3-5 is better than AM-3-3. Some essays were carried out with membranes saturated with water to increase selectivity: the measurements clearly showed an initial enhancement followed by a consistent reduction with rising temperature, due to the removal of the water molecules responsible for the blockage of some pores. With respect to real selectivities of hydrogen-containing mixtures, more experiments must be performed, and the analytical quantification of hydrogen should be improved.

Concerning modelling, new expressions for Maxwell-Stefan thermodynamic factors were derived for pure and multicomponent Nitta, Langmuir-Freundlich, and Toth isotherms, being tested with equilibrium and permeation data from literature. (It is worth noting that only pure and binary classical and dual site Langmuir equations are available). The validation procedure adopted was very stringent: i) the multicomponent isotherms were predicted from pure gas data; ii) the diffusion parameters of pure components were fitted to single permeation data; iii) then, the Maxwell-Stefan crossed diffusivities were estimated by the Vignes relation; finally, iv) the new equations were tested using these parameters, and were able to estimate successfully binary fluxes.

In parallel to the main focus of gas permeation, a new Maxwell-Stefan based model has been also derived for ion-exchange in microporous materials. The model was validated with data for Hg^{2+} and Cd^{2+} removal from aqueous solution using ETS-4. Its predicting ability has been also analyzed, being possible to conclude it performs very successfully. In effect, good predictions were accomplished with parameters optimized from independent sets of data. Such performance may be attributed to the sound physical principles of Maxwell-Stefan theory.

Index

Figures List

Tables List

Nomenclature

A	Surface area (m^2)
$AARD$	Average absolute relative deviation (%)
B	Mobility of diffusing gas (mol m^2 J^{-1} s^{-1})
B_0	Medium permeability (m^2)
$[B]$	Square matrix of inverted Maxwell-Stefan diffusivities (m^2 s)
BPR	Back pressure regulator
b	Equilibrium adsorption constant (Pa^{-1})
b_0	Equilibrium adsorption constant ate the reference temperature T_0 (Pa^{-1})
c	Concentration of diffusing species (mol m^{-3})
D	Self-diffusion coefficient (m^2 s^{-1})
D_{ij}	Interdiffusion coefficient (m^2 s^{-1})
$Đ$	Maxwell-Stefan (MS) diffusivity (m^2 s^{-1})
DGM	Dusty gas model
DSL	Dual-site Langmuir
d_k	Kinetic diameter (m)
d_p	Pore diameter or particle diameter (m)
E_a	Activation energy (J mol^{-1})
F	Faraday constant (C mol^{-1})
f	Fugacity (Pa)
g	Geometrical factor
GC	Gas chromatograph
ΔH_{ads}	Enthalpy of adsorption (J mol^{-1})
IAS	Ideal adsorbed solution
IT	Irreversible thermodynamics
J	Molar diffusion flux (mol $m^{-2}s^{-1}$)
K	Henry's constant (mol kg^{-1} Pa^{-1})
K_F	Freundlich parameter

k_1	Rate constant of the first order sorption (s^{-1})
k_2	Rate constant of the second order sorption (m^3 mol^{-1} s^{-1})
k_f	Convective mass transfer coefficient (m s^{-1})
L	Onsager coefficients or $[L]=[B]^{-1}$
l_d	Diffusion length (m)
M	Molecular weight (kg mol^{-1})
MFC	Mass flow controller
MFM	Mass flow meter
MS	Maxwell-Stefan
N	Molar flux (mol $m^{-2}s^{-1}$)
NP	Nernst-Planck
n	Number of sites occupied by one adsorbed molecule
n_F	Freundlich parameter
P	Total pressure (Pa)
P_M	Membrane permeability (mol $m^{-1}s^{-1}Pa^{-1}$)
P_m	Arithmetic mean pressure (Pa)
p	Partial pressure (Pa)
PT	Pressure transducer
Q	Ion exchanger capacity (eq m^{-3}) or Isoteric heat adsorption (J mol^{-1}) or volumetric flow rate (cm^3 min^{-1})
Q_{st}	Isosteric adsorption energy (J mol^{-1})
q	Molar concentration of adsorbed species in the solid (mol kg^{-1} or mol m^{-3})
$\overline{q}$	Average loading per unit particle volume (mol m^{-3})
R	Particle Radius (m)
$\Re$	Gas constant (J $mol^{-1}K^{-1}$)
r	Radial position (m)
Re	Reynolds number
Sc	Schmidt number
Sh	Sherwood number
T	Temperature (K)

t	Time (s) or Toth isotherm parameter
TC	Temperature controller
TCD	Thermal conductivity detector
u	Adsorbate-adsorbate interaction parameter or velocity of diffusing species (m s^{-1})
$\bar{u}$	Mean velocity of diffusing species (m s^{-1})
$\bar{V}$	Partial molar volume (cm^3 mol^{-1})
V_L	Volume of liquid phase (m^3)
V_s	Volume of solid phase (m^3)
WK	Wicke-Kallenback
X	Generalized force (kg m^2 s^{-2})
x	Molar fractions in the retentate
y	Molar fractions in the permeate or molar fraction of fixed charged groups
Z	Number of adjacent sites
z	Distance coordinate (m) or electrochemical valence or number of adjacent sites

Greek letters

α	Separation factor or constant parameter for Langmuir-Freundlich and Toth isotherms
α^*	Ideal selectivity
α'	Viscous selectivity factor
Γ	Thermodynamic factor
γ	Activity coefficient
δ	Membrane thickness (m)
δ_{ij}	Delta of Kronecker
ε	Porosity or mixed power input per unit of fluid mass
η	Viscosity (Pa s)
θ	Fractional occupancy
λ	Mean free path (m)

μ	Chemical potential (J mol^{-1})
ν	Jump frequency (s^{-1}) or kinematic viscosity (Pa s)
ξ	$= P_P / P_F$
Π	Permeance (mol $m^{-2}s^{-1}Pa^{-1}$)
π	Spreading pressure (Pa)
ρ , ρ_p	Solid density (kg m^{-3})
σ	Rate of entropy production (J m^{-3} s^{-1} K^{-1})
τ	Tortuosity
ϕ	Electrostatic potential (V)
χ	Constant parameter
Ψ	Dissipation function (J m^{-3} s^{-1})

Subscripts

0	Reference condition
e	Equilibrium
F	Freundlich
f	Feed
g	Activated gaseous diffusion
Kn	Knudsen diffusion
L	Langmuir
LF	Langmuir-Freundlich
N	Nitta
p	Permeate
R	Retentate or particle radius
s	Solid or surface diffusion
sat	Saturation
sol	Bulk solution
sup	Support
T	Toth
T,P	Derivative at constant temperature and pressure

t	Total
w	Aqueous solution
v	Viscous flow

Superscripts

i,j	Species i and j
o	Reference condition
s	Surface diffusion

I. Introduction

Nowadays, membrane technology is applied in a variety of industries offering a number of important benefits over classical separation processes. For instance, membrane processes for gas separation play an increasingly role in reducing the environmental impact and energy costs of industrial processes. Moreover, membrane units require a small layout, comprising also a low mechanical complexity.

New application fields have high demands and expectations regarding the thermal and chemical stability of membranes. The polymeric ones are the most widely used due to their relatively low manufacturing cost, but stability could limit their applications under harsh environment. Proper inorganic membranes may be robust under such conditions, which allied to high selectivities make them promising alternatives to more conventional and/or inefficient processes.

The synthesis of inorganic membranes is an important research area of the Associated Laboratory CICECO (University of Aveiro). For instance, new microporous titanosilicates, such as AM-*n* materials, have been firstly synthesized by CICECO teams. Similarly to zeolites, titanosilicates exhibit a well-defined three-dimensional crystalline structure with molecular dimensions, being able to separate mixtures based on differences in affinity and sieving effect. Furthermore, titanosilicate membranes offer important benefits over the classical zeolite ones, including the possibility of synthesis without organic templates, which avoids subsequent calcination treatments responsible for irreversible defects, and exhibit novel possibilities of isomorphous framework substitution, allowing for fine-tuning catalytic and adsorption properties.

The performance of a given membrane is primarily associated with its selectivity and permeance. In order to obtain a high selective membrane, the separation layer crystals must form a continuous thin film, where the intra-crystalline pores are the unique available pathways for gas permeation. The synthesis procedure of inorganic membranes is based on a cyclic trial and error approach: membranes are prepared and characterized; then, preparation conditions are continuously optimised until a good quality membrane is obtained. With this information, the ideal preparation conditions to promote an efficient intergrowth between crystals may be reached. CICECO owns the relevant equipment to carry out a detailed structural and morphological characterization. Beyond this characterization, the study of their permeation properties is indispensable. Membrane quality should be assessed by measuring permeances of individual gases as well as mixture separation factors. Accordingly, this work is focused on the dynamic characterization by permeability tests of microporous titanosilicate membranes synthesized by CICECO, in order to optimize their synthesis conditions.

Modelling is fundamental to interpret experimental data, predict the dynamic behaviour of any process, optimize its operating conditions, and scale up from laboratory to commercial size. Prediction of the separation performance of a given membrane requires the knowledge of multicomponent diffusion, adsorption, and structure parameters, which may be determined by experimental methods combined with adequate modelling of equilibrium and transport phenomena. The Maxwell-Stefan formalism is the most advisable and physically sound approach to describe multicomponent diffusion. It is exceptionally versatile, being successfully applied in this work to describe permeation as well as ion exchange through molecular sieves.

In the following, the structure of the present thesis will be summarily described. This document is divided into eight chapters. In Chapter II, the main fundaments of membrane technology are briefly boarder. Firstly, an overview of the main membrane processes, advantages and applications are presented; afterward, a more detailed discussion around inorganic membranes is provided, detaching microporous zeolite and titanosilicate membranes. Finally, some membrane structural and dynamic characterization methods are described. This chapter aims a simple elucidation of the main topics covered throughout the present work.

Chapter III describes mass transport phenomena occurring in microporous membranes. The transport mechanisms for single gases in porous media are firstly explained and the corresponding equations presented; subsequently, multicomponent mass transport relations are derived based on the Maxwell-Stefan equations and on Irreversible Thermodynamics theory. This chapter is fundamental for the interpretation of the experimental data obtained in this work and compiled from literature, whose results are discussed in Chapter VI.

Chapter IV focuses the modelling of ion exchange with microporous titanosilicates based on the Maxwell-Stefan equations. Initially, a brief description of the more classical kinetic models and Nernst-Planck equations is presented. Finally, a detailed model based on the Maxwell-Stefan equations is derived to describe batch ion exchange process using microporous materials. The model is validated using data for metal ions removal from aqueous solution using a microporous titanosilicate.

Chapter V is the experimental section, where the set-up and all procedures adopted for the dynamic characterization of membranes are described in detail.

In Chapter VI, modelling and experimental data are presented and discussed. New expressions for Maxwell-Stefan thermodynamic factors are derived for pure and multicomponent Nitta, Langmuir-Freundlich, and Toth isotherms, being tested with equilibrium and permeation data from literature. The permeation measurements in AM-3, ETS-10, ZSM-5, and zeolite 4A membranes, at fixed and programmed temperatures, are also given. Data are modelled based on the gas transport mechanisms described in Chapter III.

The major conclusions of this thesis are pointed out in Chapter VII, along with some suggestions for future work.

II. Fundamentals of Membrane Processes

1. Introduction

Membrane technology is becoming a very promising field of separation processes. In recent years the development of this technology has being expanding and the number of potential applications growing rapidly, mainly owing to the availability of microporous membranes.

A membrane is a semipermeable barrier separating two phases, where mass transfer occurs under the action of a driving force (Mulder, 1997; Tavolaro and Drioli, 1999). In membrane processes, a feed mixture is separated into two streams: permeate (which permeates the membrane) and retentate (which does not diffuse through membrane). Separation takes place owing to the membrane ability to transport one component from the feed mixture more readily than the others, due to differences in size, shape or affinity (Mulder, 1997).

Several membrane processes may be distinguished essentially by the driving force responsible for permeation (i.e. gradients in pressure, concentration, temperature or electrical potential), the physical state of streams, and membrane type. Accordingly, one may distinguish microfiltration, ultrafiltration, nanofiltration, reverse osmosis, gas permeation, pervaporation, dialysis, electrodialysis, membrane electrolysis, thermal-osmosis, and membrane distillation. It is well known that the actual driving force for transmembrane transport arises from a gradient in chemical potential (electrical potential included), as will be explained in Chapter III. A detailed description of distinct membrane

processes may be found in fundamental texts (Rautenbach and Albrecht, 1989; Ho and Sirkar, 1992; Mulder, 1997).

Membrane technology offers a number of important benefits over classical separation processes (Mulder, 1997; Koros, 2004; Rand and Dell, 2008). For instance, (i) separation can be carried out continuously; (ii) the energy consumption is generally low, a highly required quality when presently energy conservation is one of the most important priorities for the industry, reducing the environmental impact and energy costs of industrial processes – the energy required in some large-scale separations can be one order of magnitude lower when membranes are used instead of traditional thermal separations; (iii) membranes can be easily combined with other separation processes, giving rise to hybrid processes; (iv) separation can be carried out under mild conditions; (v) up-scaling is easy and membrane units require a small layout, which makes them attractive for isolated applications such as offshore gas-processing platforms; and (vi) membrane properties are variable and can be adjusted to the specific requirements of each process. Despite such benefits, membrane technology is still under development holding a number of drawbacks, such as (i) the possibility of concentration polarization and membrane fouling, which reduces the permeation fluxes and change the selectivity of the process, giving rise to a frequent need of cleaning; (ii) low lifetime and selectivity; (iii) the up-scaling factor is more or less linear; and (iv) the operating temperature and pH conditions may affect the membrane structure and must be taken into account.

Nowadays, membranes are applied in a variety of industries to recover valuable products or to reduce unwanted chemicals from exhaust streams. For instance, they may be found in petrochemical, food processing, metallurgy, pulp and paper, textile, pharmaceutical, automotive, dairy, and biotechnology industry (Burggraaf and Cot, 1996; Mulder, 1997). Moreover, membrane technology is becoming increasingly important also in water treatment for domestic and industrial water supply (Mulder, 1997). In seawater desalination, membranes operations are an effective approach for solving the freshwater requirements in many regions of the world, at lower costs and minimum environmental impact (Bernardo *et al.*, 2009). In other applications, membranes have been combined and embodied with chemical or biochemical reactions, where they work as catalysts as well as selective barriers to remove one of the products, shifting the chemical equilibrium, or to

selectively remove reaction inhibitors. Membranes can be used to enhance the conversion of de-hydrogenations, partial oxidations, isomerisations and esterifications (Caro and Noack, 2008), or to remove inhibitory compounds during fermentation processes (Crespo and Carrondo, 1993). For instance, Akamatsu *et al.* (2009) obtained hydrogen with purity up to 99.9% by dehydrogenation of cyclohexane using a hydrogen-selective amorphous silica membrane. Caro *et al.* (2005) investigated the reaction of *n*-propanol with propionic acid using a ZSM-5 water-selective membrane, and obtained an enhancement from 52% to 92% in the ester yield for infinite reaction time. Kita *et al.* (2007) found conversions of about 100% during esterification of lactic acid with ethanol using hydrophilic ZSM-5 and MOR membranes.

Concerning gas separations, some relevant industrial applications are: (i) H_2/N_2 and H_2/hydrocarbon separations in ammonia and petrochemical plants; (ii) separation of N_2 from air; (iii) CO_2 and water removal from natural gas; (iv) removal of CO_2 from process streams to prevent the "greenhouse effect"; (v) removal of volatile organic compounds from air or nitrogen streams; (vi) removal of H_2S from natural gas, refinery gas, and coal gas streams for odor control; and (vii) separation of hydrocarbon isomers in the petrochemical industries (e.g., mixtures of alkanes). The oxygen enrichment of air for medical purposes is also an important example (Burggraaf and Cot, 1996).

The performance of a given membrane is primarily related with its nature, i.e., its material and structure. Membranes can be natural or synthetic; the last ones can be further subdivided into organic (polymeric) and inorganic (e.g., alumina, metal and zeolites) (Mulder, 1997; Tavolaro and Drioli, 1999). Synthetic membranes may be also classified based on their morphology or structure. This is a very pertinent classification since these characteristics may determine its application. Accordingly, two classes of membranes are distinguished: dense (non-porous) and porous membranes. Following IUPAC classification, porous membranes are microporous ($d_p < 2$ nm), mesoporous ($2 < d_p < 50$ nm) or macroporous ($d_p > 50$ nm). Dense membranes are capable of separating molecules because of differences in solubility and/or diffusivity, where solubility plays a particularly significant role. Porous membranes induce separation by differences in size, shape, or affinity between permeating molecules and the material (Burggraaf and Cot, 1996; Mulder, 1997). In fact, microporous membranes can discriminate molecules of similar diameters,

polarities and/or molecular weight. In addition, their structures may be tuned in order to suit a particular separation. Accordingly, pore size and host-sorbate interactions can be adjusted by chemical modifications, such as ion exchange or changing the framework composition.

Concerning its structure, inorganic membranes can be symmetric or asymmetric. Symmetric membranes (or isotropic) are composed by a single material with one chemical composition and one morphological structure. These structures are usually thick in order to obtain mechanical strength, which is a disadvantage for obtaining large fluxes. On the other hand, asymmetric membranes (or anisotropic) are composed by two or more structural planes with different morphology, consisting generally in a combination of a supporting system with large pores and layers with gradually decreasing pore size. In this way, thin films and consequently higher permeabilities may be obtained (Burggraaf and Cot, 1996; Tavolaro and Drioli, 1999). A schematic representation of synthetic membranes structures is presented in Figure II.1.

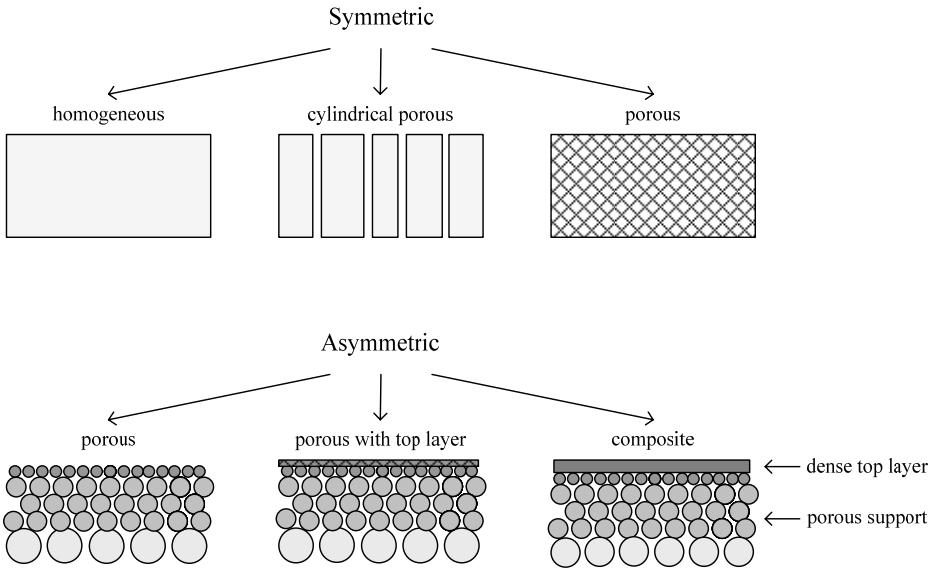

Figure II.1 – Schematic representation of synthetic membrane structures.

Membrane systems (support and separation layer) are generally assembled into modules (Burggraaf and Cot, 1996). Five module architectures can be distinguished, namely: tubular, capillary, hollow fibre, plate and frame and spiral-wound modules

(Rautenbach and Albrecht, 1989). The transport properties of membrane systems are also dependent on the architecture of the membrane modules (Burggraaf and Cot, 1996).

The performance of a given membrane in gas separation is mostly characterized by two parameters: selectivity and permeability. The selectivity describes the capacity of a given membrane to separate the components of a mixture and quantifies the enrichment of the desired product relatively to the feed stream; the permeability is the rate at which the molecules permeate through a membrane and determines the membrane productivity. Both high selectivity and high permeability are required to obtain good quality and economically feasible membranes. Nonetheless, low permeability can be compensated to a certain extent by an increase in the membrane surface area. Low selectivity leads to multi-stage processes, which in most cases are not economically viable when compared with established conventional processes (Rautenbach and Albrecht, 1989). The permeation flux of a molecule i through the membrane is given by the following relation:

$$N_i = \frac{P_{M,i}}{\delta} \times (\text{driving force}) = \Pi_i \times (\text{driving force}) \tag{II.1}$$

where $P_{M,i}$ is the membrane permeability for species i, δ is the membrane thickness, and $\Pi_i \equiv P_{M,i}/\delta$ is the permeance. In the case of gases at low pressure, the partial pressure difference across membrane, Δp_i, provides the driving force in gas mixture permeation, i.e., $\Delta p_i = p_{i,f} - p_{i,p} = P_f x_i - P_p y_i$, where subscripts f and p stand for feed and permeate, respectively, P is total pressure, and x_i and y_i are the molar fractions of component i in the retentate and permeate streams. For non-ideal gases, fugacities should be used instead. Taking into account previous equations, one obtains:

$$N_i = \Pi_i \left(x_i P_f - y_i P_p \right) \tag{II.2}$$

which for pure gases simplifies to:

$$N_i = \Pi_i \left(P_f - P_p \right) = \Pi_i \, \Delta P \tag{II.3}$$

The separation factor, α_{ij}, expresses the selectivity of the membrane towards a mixture of components i and j, which for gases is:

$$\alpha_{ij} \equiv \frac{y_i/y_j}{x_i/x_j} = \alpha_{ij}^{*}\left[\frac{x_i(\alpha_{ij}-1)+1-\xi\alpha_{ij}}{x_i(\alpha_{ij}-1)+1-\xi}\right] \tag{II.4}$$

where $\xi = P_p/P_f$, and the ideal selectivity, $\alpha_{ij}^{*} \equiv \Pi_i/\Pi_j$, is the key parameter to preview membrane performance, and corresponds to the situation where $\xi \to 0$, i.e., $P_f >> P_p$ (Mulder, 1997). A number of factors are responsible for selectivity deviations from the corresponding ideal values, such as pressure and temperature conditions or non-ideality due to co-existence of molecules in the mixture. Nonetheless, ideal values found in literature can be taken as a good starting point for the selection of an appropriate membrane material (Koros, 1995; Hsieh, 1996). It is important to refer that separation factors are frequently influenced not only by differences in intrinsic diffusivities, but also by their adsorption extent. For instance, the presence of an adsorbed compound may hinder the diffusion of other molecules, which may reduce strongly the permeability in microporous materials. This subject will be discussed in more detail in Chapter III.

2. Inorganic membranes

New membrane application fields have high demands and expectations regarding its thermal stability for high temperature applications, solvent and chemistry stability, sterilization ability and biocompactibility (Caro *et al.*, 2000). Although polymeric membranes show interesting selectivity in many gas separations, they can, in general, hardly operate successfully at harsh conditions. On the other hand, the high thermal and chemical stability and resistance to high pressure differences of microporous inorganic membranes make them promising materials for new gas separation applications. Moreover, the chemical stability of polymeric membrane is also limited with respect to pH and organic liquids, whereas inorganic materials can generally be applied at a large pH range and in any organic solvent. Also important are their greater lifetime and ease of cleaning, especially in high fouling applications (Mulder, 1997).

Many efforts have been made to design new polymers or modify existing materials in order to overcome the stability limitations of polymeric membranes (Shao *et al.*, 2009). For instance, interesting properties may be found by the synthesis of a block polymer system, consisting of microphase separated structures of hard glassy and soft rubbery polymer segments (Okamoto *et al.*, 1995; Powell and Qiao, 2006). In this case, gas permeation occurs primarily through the flexible chain structure of rubbery segments, which provides a good permeability, while glassy polymers offer mechanical support and chemical and thermal resistance, especially when formed by high temperature materials such as polyimides or polypyrrolones (Powell and Qiao, 2006). Synthesis of organic-inorganic hybrid membranes or mixed-matrix membranes is an additional technique to enhance the properties of polymeric membranes (Merkel *et al.*, 2002; Bernardo *et al.*, 2009) . The use of two materials with different flux and selectivity allows the combination of polymers features with the high performance of inorganic materials. However, besides economical advantages of mixed-matrix membranes over inorganic ones, their brittleness and difficulties for commercial scale manufacture remain important challenges.

Inorganic membranes can be synthesized from different materials (e.g., ceramic, glass, metal and zeolite-type materials). The most studied microporous inorganic membranes are amorphous metal oxides and zeolites. The first group has a very limited hydrothermal stability, excluding them for gas separation in atmospheres containing steam at high temperature. On the other hand, zeolite and related materials (e.g., titanosilicates and vanadosilicates) offer much better thermal and hydrothermal stability (Rocha and Anderson, 2000).

At this point, it is convenient to clarify some nomenclature aspects. The terms zeolite and molecular sieve are often indistinctly used in literature. It is then straightforward to present a convenient classification of molecular sieves as function of their composition, which is given in Figure II.2.

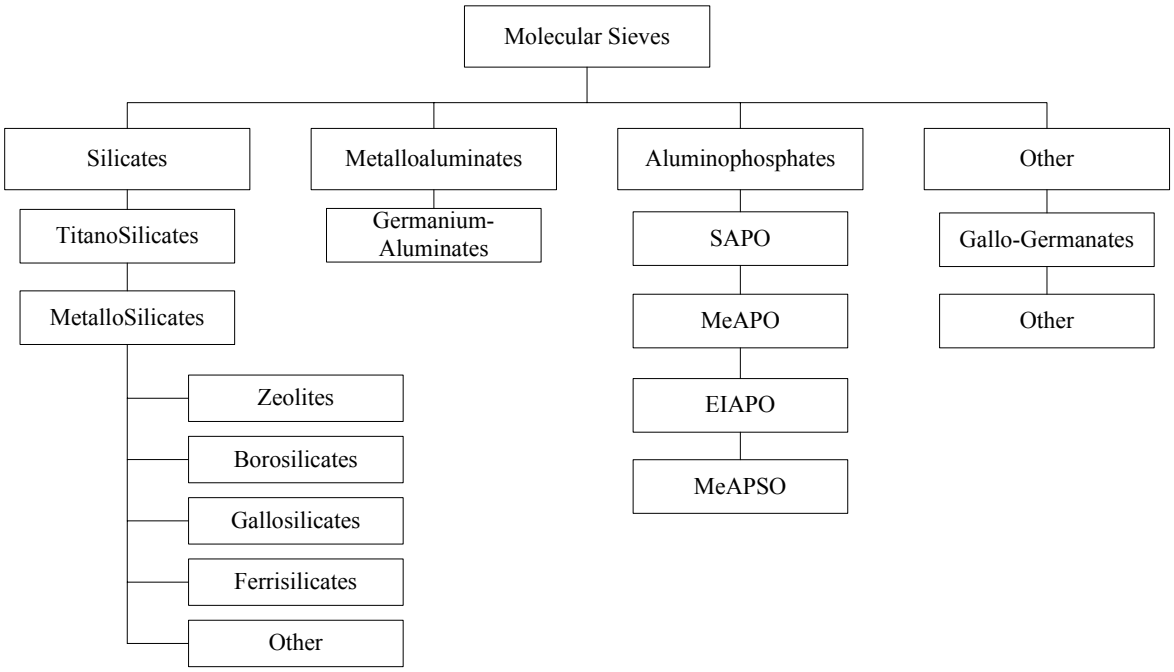

Figure II.2 – Classification of molecular sieve materials, as proposed by Szostak (1989).

2.1 Zeolite membranes

In recent years, zeolites have attracted increasing interest due to their potential applications as separation membranes, catalytic membrane reactors, chemical sensors, electrodes, opto-electronic devices, or low dielectric constant materials for use as electrical insulators, protection or insulation layers (Caro and Noack, 2008).

Zeolites are three-dimensional microporous crystalline solids with a well defined structure of channels and cavities (Breck, 1974; Rocha and Anderson, 2000). These materials have a regular framework formed by a three-dimensional combination of SiO_4 and AlO_4 tetrahedrons building blocks connected with each other by shared oxygen atoms. An isolated SiO_4 group contains a charge of -4 while it is neutral in a solid containing an O/Si ratio of two, since each oxygen atom is connected with two Si atoms; the AlO_4 unit charge is -1. Accordingly, the global structure of zeolites carries a negative charge, which is neutralized by exchangeable extra-framework cations, generally from groups I and II of periodic table. The structural formula of zeolites may be expressed for the crystallographic unit cell as:

$M_{x/n}[(AlO_2)_x(SiO_2)_y].mH_2O$

where M is a cation of valence n, which balances the negative charge, m is the number of water molecules in the zeolite, and the sum $x+y$ is the total number of tetrahedra in the unit cell. The channels and cavities of zeolites framework are occupied by the cations and water molecules.

Based on their pore dimensions, zeolites are classified into small, medium, large, and ultra-large pore materials (Tavolaro and Drioli, 1999; Guisnet and Giilson, 2002; Chao *et al.*, 2008). Small pore structures have eight-membered ring pore aperture, medium pore structures have 10-membered rings, large pore zeolite have 12-membered rings, and ultra-large frameworks consist of 14-, 18-, and 20-membered rings. Some examples of zeolite structures with different pore dimensions are pictured in Figure II.3

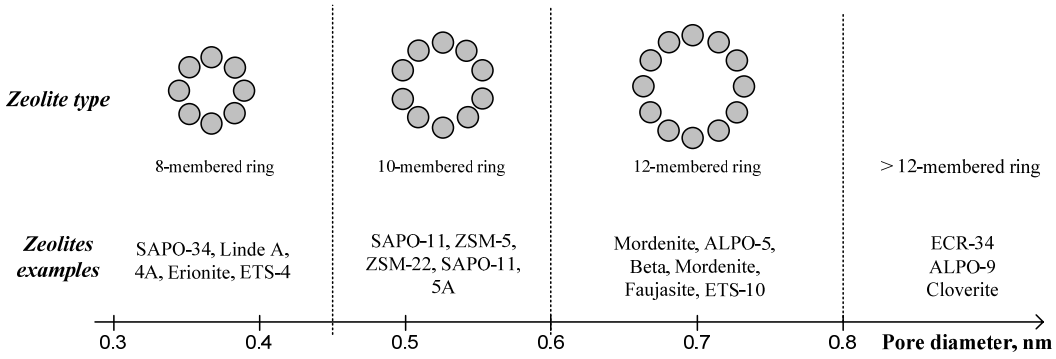

Figure II.3 – Classification of zeolites based on pore dimensions. Adapted from Chao *et al.* (2008).

Zeolite materials own a number of advantages over other microporous materials, such as pores with uniform molecular dimensions, ion exchange capability and selectivity, interesting adsorption properties, relatively easy catalytic activation, possibility to develop internal acidity, high thermal stability and high internal surface area (Tavolaro and Drioli, 1999). Additionally, they can be regenerated using relatively easy and well known methods, as thermal, pressure, and related swing adsorption, or ion exchange (Wankat, 1994).

The molecular sieving action of microporous zeolites, together with their large surface areas and controlled host-sorbate interactions, are the primary motivations in zeolitic membranes (Tavolaro and Drioli, 1999). These features allow them to carry out separations which are out of reach for common membranes (e.g. separation of isomers or compounds with similar diameters, polarities and/or molecular weight) and compete with traditional separation methods.

In order to prepare supported membranes, zeolite crystals need to grow on porous substrates to form a continuous film, having the zeolitic pores as the unique available pathway for molecules transport (Tavolaro and Drioli, 1999). Zeolite membranes are commonly prepared by *in situ* direct hydrothermal synthesis on porous supports. This method involves one step liquid-phase hydrothermal synthesis on the top or inside of support pores, which is immersed into a zeolite precursor gel or clear solution, under autogenous pressure and at a constant temperature.

Alternatively, the zeolite layer can be formed in two steps using seed crystals, which grow together to form a continuous supported zeolite layer in a subsequent hydrothermal synthesis. With this seeding crystallization technique, the nucleation and the crystal growth are decoupled allowing a controlled preparation of supported zeolite membranes. In the first step, a colloidal suspension of zeolite crystal seeds is prepared in the absence of the support. Subsequently, these seeds are deposited on the surface support and brought into contact with a solution containing the necessary nutrients for growth. A continuous zeolite layer is then formed by a second crystallization step. Since the concentration needed for secondary growth is lower than the required for nucleation, further nucleation is strongly decreased and almost all crystals growth takes place over the existing crystal seeds. By regulating the composition and concentration of the secondary growth solution, the rate and direction of crystals growth can be controlled. An oriented zeolite film is advantageous because the number of intercrystalline defects is reduced when crystals grow uniformly in the same direction. Moreover, higher permeabilities could be expected when crystal orientation allows the channels to be aligned with flow direction (Coronas and Santamaria, 1999). Furthermore, by providing the nutrients from the growth side, membrane thickness can be more accurately controlled; in this way, membranes with a thickness of only a few hundreds nanometres may be prepared.

Finally, zeolite layers can also be synthesized by crystallization of an amorphous dry gel on the porous support either by a vapour-phase transport method, when the structure-directing agent (SDA) is in the vapour, or by steam-assisted crystallization with a dry gel containing the SDA (Coronas and Santamaria, 1999; Caro *et al.*, 2000; Caro and Noack, 2008).

Undesirable transmembrane pathways larger than the intracrystalline zeolite pores, i.e. defects, are frequently formed during membrane synthesis. Larger defects could be eliminated by repeated crystallization (Coronas and Santamaria, 1999; Tavolaro and Drioli, 1999). A number of researchers have concluded that their membranes prepared in a single hydrothermal synthesis had defects because of the lack of connectivity between the individual particles, which points out that one synthesis may be not enough to achieve sufficient crystal intergrowth. Elimination of small defects may be possible by post-synthesis processing methods such as chemical vapor deposition of silica, via reaction with a silicon alkoxide or other silylation agents. Those treatments involve reduction of the pore openings on the external surface of the crystals (Coronas and Santamaria, 1999; Tavolaro and Drioli, 1999).

The synthesis of supported zeolite membranes has been carried out following trial and error procedures. The starting point to obtain a new zeolite membrane involves, in general, a synthesis gel with a composition similar to that reported for the synthesis of the zeolite as individual crystals. Once synthesised, the membrane would be subjected to characterization, and, depending on the results obtained, the synthesis would be repeated under different preparation conditions: gel composition, synthesis time, method of wetting the support, or rotation of the autoclave. It is worth noting that the presence of the support introduces a number of new factors which makes synthesis more difficult to reproduce. For instance, the mechanism of nucleation changes because the surface of the support provides nucleation sites that are not present in homogenous synthesis, and the support itself may dissolve in the synthesis gel and change its composition (Coronas and Santamaria, 1999).

2.2 Titanosilicate membranes

Microporous titanosilicates are novel materials that may broad the scope of application of zeolite membranes and thin films to separations, catalytic membrane reactors and sensors. The structure of these materials consists of interlinked octahedral and tetrahedral frameworks. Similarly to zeolites, titanosilicates exhibit a well-defined three-dimensional crystalline structure with molecular dimensions, being able to separate mixtures based on differences in affinity and sieving effect (Lin *et al.*, 1997; Liu *et al.*, 1997; Liu *et al.*, 1999; Rocha and Anderson, 2000). Moreover, they offer important benefits over classical zeolite membranes, namely: i) they are generally synthesised in the absence of organic templates, avoiding usual subsequent calcination treatments (at nearly 500ºC), which often cause irreversible defects and/or loss of active surface groups; ii) they are usually prepared under moderate pH conditions (generally, at pH=10–13), reducing chemical attack to the support; iii) they exhibit novel possibilities of isomorphous framework substitution, allowing for fine-tuning catalytic and adsorption properties; and iv) generally, they have strong alkalinity, complementing the acid properties of classic zeolites (Lin *et al.*, 2004).

AM-3 (Aveiro-Manchester number 3) is a synthetic microporous titanosilicate analogue of mineral penkvilksite, with an ideal formula $Na_4Ti_2SiO_{22}.5H_2O$ (Lin *et al.*, 1997). Its structure consists of SiO_4 tetrahedra connected by individual TiO_6 octahedra forming a three-dimensional framework of 6-ring channels (Lin *et al.*, 2006). In a previous work it was shown that AM materials do not adsorb any significant amount of nitrogen but they do adsorb water in relatively large amounts (Lin *et al.*, 1997). In addition, AM-3 was demonstrated to be stable up to ca. 600 ºC, loosing water and rehydrating reversibly after being kept in air for a few hours at room temperature. A detailed morphological characterization of AM-3 was first reported by Lin *et al.* (1997) and later by Rocha and Anderson (2000). Figure II.4a shows a scanning electron micrograph of AM-3 crystals.

ETS-10 (Engelhard Titanosilicate number 10) is a synthetic microporous titanosilicate discovered by Kuznicki (1989), with no mineral analogue. Its structure is composed by corner sharing SiO_4 tetrahedra and TiO_4 octahedra, linked by oxygen atoms, forming a three-dimensional system of wide 12-membered pores. This material shows a disordered structure and has excellent characteristics for diffusion (Rocha and Anderson, 2000). Moreover, ETS-10 has a remarkable high thermal stability. The structural formula

of the ETS-10 basic unit is $Si_4OTi_8O_{104}^{16-}$, which is balanced by 16 monovalent cations (usually Na^+ and K^+) (Rocha and Anderson, 2000). A scanning electron micrograph of ETS-10 crystals is presented in Figure II.4b.

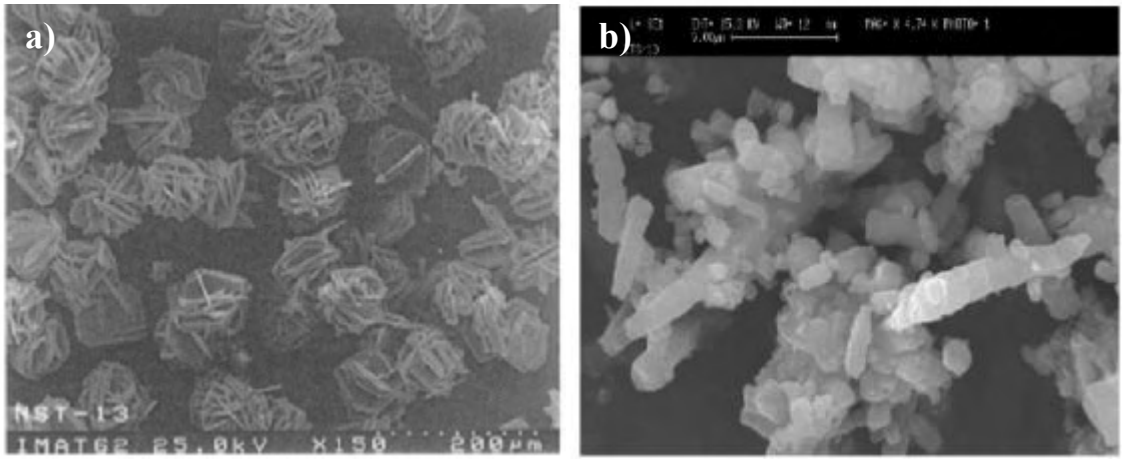

Figure II.4 – Scanning electron micrograph of: a) AM-3 crystals and b) ETS-10 crystals (Lin *et al.*, 1997; Pavel *et al.*, 2002).

Only a small number of microporous titanosilicate membranes have been synthesized and characterized, mainly reporting on ETS-4 (Braunbarth *et al.*, 2000; Guan *et al.*, 2001,2002). Accordingly, separations of N_2 from CO_2, O_2, Ar and CH_4 as well as pervaporation experiments of water/ethanol mixtures have been investigated using this material. Preparation of ETS-4 films on porous alumina and titania supports have been also described by Yilmaz *et al.* (2006), however only the crystals orientation was investigated. Hetero-epitaxial growth of ETS-10 on ETS-4 has been performed, but no permeation or separation results have been published (Jeong *et al.*, 2002). Preparation and characterization of ETS-10 membranes were presented for the first time by Lin *et al.* (2004), where pure N_2 permeation and water/alcohol pervaporation experiments were carried out. Subsequently, permeation of different gases at programmed temperature, and propylene/propane separation studies in ETS-10 membranes were reported by Tiscornia *et al.* (2005,2007). These studies showed ETS-10 is able to separate propylene/propane and water/ethanol mixtures with separation factors ranging between 3.8-6.5 and 7-12, respectively. Sebastian *et al.* (2005,2006,2008) reported the synthesis, characterization,

and separation properties of a Ti-Silicate umbite membrane (AM-2) prepared on porous α-alumina and TiO_2 tubular supports by seeded hydrothermal synthesis; selectivities higher than 30 were obtained for H_2 separation from N_2, CO_2 or propane mixtures. Moreover, Sebastian *et al.* (2008) used AM-2 membranes for H_2/N_2 separation in the presence of moisture concluding that, unlike other microporous zeolitic hydrophilic membranes, water should not permeate through the intrinsic micropores of the zeolitic material, undergoing capillary condensation in the inter-crystalline defects, giving rise to an increase in the H_2/N_2 selectivity. Reported results have revealed the potential of these membranes for real applications concerning purification of hydrogen-containing streams, and H_2 proton-exchange membrane (PEM) fuel cells.

3. Characterization methods

There is no universal method for characterization of all materials due to the numerous characteristics involved and because the wide variety of membrane operating conditions influences directly its performance. Frequently, more than one technique is required in a detailed examination (Burggraaf and Cot, 1996). A combination of well defined characterization techniques gives valuable information about membrane morphology, which may suggest possible fields of application. In addition, it can serve as a feed-back for high quality membrane preparation.

Two different types of characterization methods can be distinguished for porous membranes: structure-related methods, in which the pore size, pore size distribution, top layer thickness, surface porosity and crystallinity are determined; and permeation-related methods, where the actual separation parameters are investigated. There are a number of structural characterization techniques available for porous media, being the following the most frequently used for microporous membranes: X-ray diffraction (XRD), which is indispensable to identify the crystals formed in the synthesis, and to evaluate their purity; scanning electron microscopy (SEM), used to analyse the shape and size of crystals, and their distribution on the support, as well as to provide a measurement of membrane thickness and a first impression on the existence of inter-crystalline defects; and surface analyzing techniques such as electron-probe microanalysis (EPMA), X-ray Photoelectron

Spectroscopy (XPS) or Energy dispersive X-ray spectrometry (EDX), used to measure the chemical elements concentration across the membrane. Concerning the permeation-related methods, the determination of the gas permeabilities through synthesized materials is particularly important because it is the only tool allowing verification of membrane compactness and selectivity (Tavolaro and Drioli, 1999). Specific permeation measurements, either of single gases or multicomponent mixtures, provide extremely useful information on the effective membrane pore structure, and on the existence of inter-crystalline defects. Moreover, in contrast with structural characterization techniques, the whole membrane surface may be investigated. Permeation experiments are often complemented by adsorption measurements, which may help to identify and/or distinguish the involved permeation mechanisms (Coronas and Santamaria, 1999). With permeation results, the ideal preparation conditions to promote an efficient intergrowth between crystals can be found. Finally, the permeation of mixtures is the real test to evaluate membrane quality to perform a given separation.

4. Hydrogen Purification

Hydrogen is an alternative clean fuel for future sustainable energy economy. The development of "The Hydrogen and Fuel Cell Technology Platform" of the European Union (HFPeurope, 2009) clearly supports the importance of this subject. Presently, steam reforming, partial oxidation of hydrocarbons, autothermal reforming, and gasification of biomass are the best economically viable options for H_2 production (Hsieh, 1996; Fang *et al.*, 2008; Rand and Dell, 2008). The downstream processing of the resulting mixtures, mainly H_2/CO_2, H_2/N_2, and H_2/light-hydrocarbons, can be advantageously accomplished by membrane technology (Hsieh, 1996).

Many techniques are in use or under study for hydrogen separation and purification, including PSA, cryogenic separation, catalytic purification and membrane processes. Membrane technology for gas separation plays an increasingly vital role owing to their well known advantages. Several membrane materials have been used for H_2 recovery. Pd metal membranes show long-term thermal and mechanical stability, as well as high separation factors towards H_2; however, Pd and its alloys are extremely expensive, making

this material economically impractical for large-scale applications (Freemantle, 2005; Adams and Mickalonis, 2007). In addition, another technical disadvantage of Pd membranes is their high sensitivity to chemicals, such as sulphur or even CO (Freemantle, 2005). Polymeric membranes are the most widely used due to their relatively low manufacturing cost, but their chemical and thermal stability limits their application in H_2 purification under harsh conditions. For instance, H_2 and CO_2 are formed at high temperature during the steam reforming process. An efficient separation of the produced H_2 should occur at the reforming temperature, which is over 450ºC. Unlike polymeric membranes, the inorganic ones are robust under such conditions and may exhibit high selectivities.

Amorphous metal oxides membranes have very limited hydrothermal stability, excluding them for H_2 removal from atmospheres containing steam at high temperature. On the other hand, zeolite membranes offer much better thermal and hydrothermal stability, but the pore size of most applied materials is not sufficiently narrow for highly selective H_2 separation. Titanosilicate membranes may become especially competitive for industrial applications due to their narrow pore size, promoting an effective size-exclusion separation.

III. Gas Transport and Adsorption in Porous Media

The understanding of mass transport mechanisms is essential for an accurate modelling of the permeances. Modelling is fundamental for interpretation of experimental data and as a predictive tool. Prediction and correlation of permeation and separation behavior requires knowledge on single and multicomponent diffusion, adsorption and structure parameters. These parameters may be determined by experimental methods and adequate modelling of transport phenomena. This chapter describes mass transport phenomena and adsorption equilibrium occurring in microporous membranes. First, transport mechanisms for single gases in porous media are briefly explained, and the corresponding equations presented. Multicomponent mass transport relations for the flux through microporous membranes are subsequently derived based on Irreversible Thermodynamics theory and on the Maxwell-Stefan equations. Finally, the adsorption equilibrium of pure and multicomponent systems is discussed in the last section of the chapter.

1. Single gas permeation

The transport mechanisms involved in porous media (see Figure III.1) are primarily related with pore diameter, d_p. Accordingly, viscous flow dominates in macropores ($d_p > 50\,\text{nm}$), where the fluid flows as a whole under a pressure gradient. In mesopores and micropores ($2 < d_p < 50\,\text{nm}$ and $d_p < 2\,\text{nm}$, respectively), collisions between molecules and pore surface are fundamental. When the mean free path, λ, (i.e., the average distance traversed

by a molecule between collisions) is comparable or larger than the pore diameter, transport falls in Knudsen regime. In small micropores, pore size approaches the molecular dimensions and the molecules may not be as free as in Knudsen diffusion, where the effect of the potential field of the solid surface is minimal (Burggraaf and Cot, 1996). In this case, commonly described as configurational diffusion, molecules may never completely escape from the force field of the surface (Xiao and Wei, 1992a) and diffusion becomes an activated process. Based on the mode of translational motion of molecules inside the pores, two distinct mechanisms may be distinguished here: molecules may retain their gaseous state (gas translational or activated gaseous diffusion) or lose their gaseous entity due to strong interaction with the solid framework and move as an adsorbed phase (solid vibration or surface diffusion) (Xiao and Wei, 1992a).

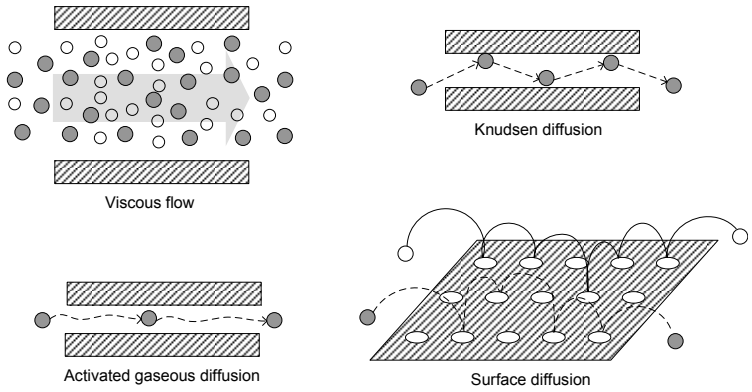

Figure III.1 – Distinct mass transport mechanisms involved in single gas transport in porous media. Adapted from Krishna (1993).

Several approaches have been proposed in literature to describe surface diffusion (Uhlhorn *et al.*, 1992; Burggraaf and Cot, 1996; Burggraaf, 1999), including the *hopping model*, by which molecules move over the surface by hopping between adjacent adsorption sites (minima in the potential energy field of the pore) (Gilliland *et al.*, 1974; Okazaki *et al.*, 1981; Xiao and Wei, 1992a; Krishna, 1993), the *hydrodynamic model*, in which adsorbed molecules are considered as a fluid film, which merely slide along the surface (Gilliland *et al.*, 1958; Gilliland *et al.*, 1974), and the *random walk model*, based on the

two-dimensional form of Fick's first law. Nonetheless, the hopping model is the most frequently adopted for modeling surface diffusion in micropores (Krishna, 1990; Xiao and Wei, 1992a,b; Krishna, 1993; Bakker *et al.*, 1997; Krishna and Paschek, 2000; Krishna and Baur, 2003; Krishna *et al.*, 2004), being adopted as well in this dissertation.

Similarly to the surface diffusion, the activated transport of gaseous molecules inside the pore may be assumed to occur by a sequence of jumps from site to site, restricted by the energy barrier imposed by the surface. Several authors report the activated gaseous diffusion as an activated process analogous to a Knudsen mechanism, denoting it by activated Knudsen diffusion (Bakker *et al.*, 1996; Burggraaf and Cot, 1996; Burggraaf, 1999; Romero *et al.*, 2004). However, Burggraaf and Cot (1996) present a slightly different concept to describe this mechanism. In their description, molecules are assumed to move freely between adsorption sites, involving an activated sub-step and a Knudsen diffusion step. This situation is reported for a ratio between pore diameter and kinetic molecular diameter around two. Moreover, the configurational diffusion regime is reached with decreasing pore size, where the remaining gaseous state within the pore is assumed to be vanished and only surface diffusion may occur.

1.1 Viscous flow

In macropores, intermolecular collisions are dominant and the mean free path of diffusion species is smaller than the pore diameter. In this case, the molar flux, J_v, under a pressure gradient may be described by a Hagen-Poiseuille type-law:

$$J_v = -\frac{\varepsilon}{\tau}\frac{d_p^2}{32\eta}\frac{P}{\Re T}\frac{dP}{dz} \tag{III.1}$$

where η is the gas viscosity, P and T are the total pressure and temperature, respectively, $\Re$ is the gas constant, and z is distance coordinate. The factor ε/τ is introduced in the flux equation to account for geometrical effects of the porous structure, being ε and τ the porosity and tortuosity, respectively.

At steady-state, the permeance through a porous membrane may be obtained after integration of equation (III.1) over the membrane thickness, δ :

$$\Pi_{\mathrm{v}} \equiv \frac{J_{\mathrm{v}}}{\Delta P} = \frac{\varepsilon d_{\mathrm{p}}^2}{32\eta\tau}\frac{P_{\mathrm{m}}}{\delta \Re T} \tag{III.2}$$

where P_{m} is the arithmetic mean pressure between two sides of the membrane.

It may be noted from equation (III.2) that permeance under viscous flow increases with increasing mean pressure, and declines with rising temperature (note that gas viscosity also increases with temperature).

1.2 Knudsen diffusion

Knudsen diffusion prevails in mesopores, where the mean free path of diffusing species is close to the pore diameter (Knudsen, 1909). Under this regime, molecule-pore wall collisions are important, being responsible for diffusion.

Knudsen diffusivity, D_{Kn}, may be expressed as the product of a geometric factor by a characteristic diffusion length and by the velocity of gas molecules (Xiao and Wei, 1992a). In this case, the diffusion length is the pore diameter, and the velocity of diffusing molecules is given by the kinetic theory of gases. The geometric factor is $1/3$ since only those molecules moving in the direction under consideration must be taken into account (Xiao and Wei, 1992a). Thus,

$$D_{\mathrm{Kn}} = \frac{d_{\mathrm{p}}}{3}\left(\frac{8\Re T}{\pi M}\right)^{0.5} \tag{III.3}$$

where M is the molecular weight of the diffusing gas.

Mass transport of single gases in porous media may be described by the Fick's first law (Fick, 1855a,b):

$$J = -D\nabla c \tag{III.4}$$

where D is the Fick diffusion coefficient, ∇ is the gradient operator, and c is the concentration of diffusing species. The expression for Knudsen diffusion flux, J_{Kn}, may be obtained by combining equation (III.3) with the Fick's first law (III.4), expressed in terms of the pressure gradient, and introducing factor ε/τ in order to account for structure geometrical effects (Burggraaf and Cot, 1996):

$$J_{\mathrm{Kn}} = -\frac{\varepsilon d_{\mathrm{p}}}{3\tau}\left(\frac{8}{\pi \Re T M}\right)^{0.5}\frac{dP}{dz} \tag{III.5}$$

The Knudsen permeance through a porous membrane may be found after integration of equation (III.5) over the membrane thickness:

$$\Pi_{\mathrm{Kn}} \equiv \frac{J_{\mathrm{Kn}}}{\Delta P} = \frac{\varepsilon d_{\mathrm{p}}}{3\tau\delta}\left(\frac{8}{\pi M \Re T}\right)^{0.5} \tag{III.6}$$

As pointed out by equation (III.6), permeance due to Knudsen diffusion is pressure-independent and decreases with temperature.

1.3 Diffusion in micropores

As aforementioned, the hopping model will be adopted in the following discussion. Gas diffusion in micropores may be explained as an activated process (Xiao and Wei, 1992a). In this case, the Fick diffusion coefficient may be expressed as follows:

$$D = g\bar{u}l_d \exp\left(\frac{-E_a}{\Re T}\right) \tag{III.7}$$

being g a geometrical factor, $\bar{u}$ the mean velocity of diffusing species, and l_d the diffusion length. The exponential term reflects the activated nature of the process and expresses the probability of a molecule to have sufficient kinetic energy to surmount an

energy barrier, E_a. The parameters involved in equation (III.7) are dependent on the pore and molecule dimension and thus on the corresponding system.

Mass transport of single gases is generally described by the Fick's first law, where a concentration gradient is assumed to be the driving force (see equation (III.4)). However, the true driving force for diffusion is believed to be the chemical potential gradient (Ruthven, 1984), which is most relevant in a microporous system. Accordingly, the permeation flux of a single gas in micropores (in the *z*–direction), in isothermal conditions, is more accurately described by:

$$J = -B\rho q \frac{\partial \mu}{\partial z} \tag{III.8}$$

where B is the mobility of diffusing gas, q is its molar concentration in the particle, ρ is the particle density, and μ is the chemical potential. Assuming the gas phase as ideal, i.e., $\mu = \mu_0 + \Re T \ln P$, where μ_0 is its standard chemical potential, the following relationship may be obtained:

$$J = -\rho q Đ \frac{d \ln P}{dz} \tag{III.9}$$

where $Đ = B\Re T$ is a corrected diffusion coefficient equivalent to a Maxwell-Stefan (MS) diffusivity (Krishna, 1990,1993; Krishna and Wesselingh, 1997). Similarly to the Maxwell-Stefan formulation, a thermodynamic factor may be defined as $\Gamma = \partial \ln P / \partial \ln q$, and the expression for permeation may be written as:

$$J = -\rho Đ \Gamma \frac{dq}{dz} \tag{III.10}$$

Fick and corrected diffusivities are related by the thermodynamic factor as $D = Đ\Gamma$. This relation, known as Darken equation, expresses the concentration dependence of Fick diffusivity, involving a generally concentration-independent corrected diffusivity. The integration of equation (III.10) is only possible if the relation between q and P is known.

In the following, its application to activated gaseous diffusion and surface diffusion mechanisms will be analyzed.

1.3.1 Activated gaseous diffusion

In the case of activated gaseous diffusion, the velocity of the molecules in gas phase is described by the kinetic theory of gases, similarly to the Knudsen mechanism, the diffusion distance may be considered the distance between two adjacent sites of low energy, l_d, while the geometrical factor is the probability of a molecule moving in the direction under consideration, $1/Z$, being Z the number of adjacent sites (Xiao and Wei, 1992a). The activation energy, $E_{\mathrm{a,g}}$, is the energy required for molecules to surmount the attractive constrictions imposed by the pore structure. As a result, the diffusivity of gaseous molecules is given by:

$$D_{\mathrm{g}} = \frac{1}{Z} l_d \left(\frac{8\Re T}{\pi M} \right)^{0.5} \exp\left(\frac{-E_{\mathrm{a,g}}}{\Re T} \right) \tag{III.11}$$

Since there is no formal adsorption, the flux may be expressed in terms of pressure. Hence, from equations (III.9) and (III.11) one may obtain:

$$J_{\mathrm{g}} = -\frac{1}{Z} l_d \left(\frac{8}{\pi M \Re T} \right)^{0.5} \exp\left(\frac{-E_{\mathrm{a,g}}}{\Re T} \right) \frac{dP}{dz} \tag{III.12}$$

Permeance through a microporous membrane may be found after integration of equation (III.12) over the membrane thickness:

$$\Pi_{\mathrm{g}} \equiv \frac{J_{\mathrm{g}}}{\Delta P} = \frac{l_d}{Z\delta} \left(\frac{8}{\pi M \Re T} \right)^{0.5} \exp\left(\frac{-E_{\mathrm{a,g}}}{\Re T} \right) \tag{III.13}$$

Equation (III.13) shows an exponential dependence of gas permeance on the temperature, differently from that of the Knudsen model.

1.3.2 Surface diffusion

For surface diffusion of adsorbed molecules, the diffusion length corresponds to the distance between two adjacent sites, l_d, and the geometrical factor represents the probability of a molecule moving in the direction under consideration, $1/Z$, similarly to the activated gaseous diffusion mechanism (Xiao and Wei, 1992a). Additionally, the velocity of adsorbed molecules is given by the product of the jump frequency, $\nu(q)$, with the jump distance. Hence, Fick diffusivity may be expressed as

$$D_s(q) = \frac{1}{Z} l_d^{\,2} \nu(q) \exp\left(\frac{-E_{a,s}}{\Re T}\right) = D_s^0(q) \exp\left(\frac{-E_{a,s}}{\Re T}\right) \tag{III.14}$$

where $D_s^0(q) = \frac{1}{Z} l_d^{\,2} \nu(q)$. According to the relation between Fick and corrected diffusivities,

$$D_s(q) = Đ_s \Gamma = Đ_s^0 \Gamma \exp\left(\frac{-E_{a,s}}{\Re T}\right) \tag{III.15}$$

where $E_{a,s}$ is the activation energy for surface diffusion.

In order to determine the thermodynamic factor and thus the flux of adsorbed molecules, the isotherm must be known. Based on different concepts and assumptions, a number of adsorption models can be found in literature (Do, 1998; Burggraaf, 1999; Pakizeh *et al.*, 2007), as will be discussed next in section 2.3.

The adsorption of gas molecules in microporous membranes occurs frequently in monolayer, being accurately represented for a large number of cases by the Langmuir isotherm:

$$\theta = \frac{q}{q_{sat}} = \frac{b_L P}{1 + b_L P} \tag{III.16}$$

where θ is the fractional occupancy, q_{sat} is concentration of adsorbed molecules at saturation, and b_{L} is the Langmuir equilibrium adsorption constant. The temperature dependency of b_{L} can be correlated by a van't Hoff-type expression:

$$b_L = b_o \exp\left[\frac{Q_{\text{st}}}{\Re T_o}\left(\frac{T_o}{T}-1\right)\right] \cong b_0 \exp\left[\frac{-\Delta H_{\text{ads}}}{\Re T_o}\left(\frac{T_o}{T}-1\right)\right] \tag{III.17}$$

where Q_{st} is the isosteric heat of adsorption, ΔH_{ads} is the enthalpy of adsorption, and b_o is b_L at the reference temperature T_o.

For the case of Langmuir regime, the thermodynamic factor reduces to:

$$\Gamma = \frac{1}{1-\theta} \tag{III.18}$$

The surface flux of adsorbed molecules in micropores may be then obtained after substitution of equations (III.15) and (III.18) into equation (III.10):

$$J_{\text{s}} = -\rho \frac{Đ_{\text{s}}^0}{1-\theta} \exp\left(\frac{-E_{\text{a,s}}}{\Re T}\right)\frac{dq}{dz} \tag{III.19}$$

or, expressed in terms of the fractional occupancy, θ,

$$J_{\text{s}} = -\rho q_{\text{sat}} \frac{Đ_{\text{s}}^0}{1-\theta} \exp\left(\frac{-E_{\text{a,s}}}{\Re T}\right)\frac{d\theta}{dz} \tag{III.20}$$

By integration over the membrane thickness, the surface permeance is found to be:

$$\Pi_{\text{s}} \equiv \frac{J_{\text{s}}}{\Delta P} = \frac{\rho}{\delta} q_{\text{sat}} Đ_{\text{s}}^0 \exp\left(\frac{-E_{\text{a,s}}}{\Re T}\right)\ln\left(\frac{1-\theta_{\text{p}}}{1-\theta_{\text{f}}}\right)\frac{1}{P_{\text{f}}-P_{\text{p}}} \qquad \text{or}$$

$$\Pi_{\text{s}} = \frac{\rho}{\delta} q_{\text{sat}} Đ_{\text{s}}^0 \exp\left(\frac{-E_{\text{a,s}}}{\Re T}\right)\ln\left[\frac{1+bP_{\text{f}}\exp\left(-\Delta H_{\text{ads}}/\Re T\right)}{1+bP_{\text{p}}\exp\left(-\Delta H_{\text{ads}}/\Re T\right)}\right]\frac{1}{P_{\text{f}}-P_{\text{p}}} \tag{III.21}$$

where the subscripts f and p refer to membrane feed and permeate sides conditions, respectively.

As shown by equation (III.21), the dependence of surface permeance on temperature is not quite straightforward. Following Burggraaf (1999), assuming $b_{\mathrm{L}}P_{\mathrm{p}}<1$, a maximum in the permeance may be expected when $E_{\mathrm{a,s}}<-\Delta H_{\mathrm{ads}}$. Similarly, Van de Graaf *et al.* (1998b) analyzed the permeance behavior with temperature and demonstrated that (*i*) if $E_{\mathrm{a,s}}>-\Delta H_{\mathrm{ads}}$, no solution is found and there is no maximum in the flux as function of temperature, being the activated diffusion dominant over all temperature range; (*ii*) if $E_{\mathrm{a,s}}=-\Delta H_{\mathrm{ads}}$, a maximum exists only when occupancy approaches zero; in this case the flux approaches an asymptotic value at higher temperatures becoming temperature-independent, and (*iii*) if $E_{\mathrm{a,s}}<-\Delta H_{\mathrm{ads}}$, a maximum in the flux can effectively be observed. The same conclusions were drawn by Kapteijn *et al.* (2000b) by calculating the first derivative of the permeation flux equation.

Corrected, or MS, diffusivities have been assumed here to be concentration-independent; however, $Đ_s$ is generally function of molecular loading (Krishna, 1990; Krishna and Paschek, 2000; Krishna and Baur, 2003; Krishna *et al.*, 2004). Molecular dynamics (MD) simulations have shown this simplification is accurate in a number of systems but may considerably fail in others. For instance, Skoulidas and Sholl (2001,2002) obtained occupancy-independent diffusivities of He, Ar and Ne in MFI (silicalite and ZSM-5 zeolites) while for larger molecules, such as CF_4 and SF_6, they were found to depend on surface occupancy. Moreover, Monte Carlo simulations performed by Paschek and Krishna (2000) for diffusion of 2-methylhexane in silicalite also exhibit a dependence of $Đ_{\mathrm{s}}$ on surface loading. The behavior of MS diffusion coefficient with occupancy has been found to diverge concerning the permeating gas and membrane structure. For instance, MS diffusivities of several gases through different zeolite structures were shown to decrease strongly with increasing loading, following in many systems the relation $Đ_{\mathrm{s}}(\theta)=Đ_{\mathrm{s}}(0)(1-\theta)$, where $Đ_{\mathrm{s}}(0)$ is the zero-loading diffusivity (Krishna, 1990; Krishna and Paschek, 2000; Krishna and Baur, 2003; Krishna *et al.*, 2004).

At low pressures the Henry's regime for adsorption is frequently valid. Under these conditions, the concentration of adsorbed gas depends linearly on the pressure, i.e.,

$$q = KP \tag{III.22}$$

where K is the Henry's constant. As for the case of activated gaseous diffusion, the thermodynamic factor is here unity, and thus Fick and corrected diffusion coefficients are equal and concentration-independent (Gavalas, 2008). In this case equation (III.10) equals the Fick's first law. The dependence of K on temperature is also given by a van't Hoff-type relation:

$$K = K_0 \exp\left(\frac{Q_{st}}{\Re T}\right) \cong K_0 \exp\left(\frac{-\Delta H_{ads}}{\Re T}\right) \tag{III.23}$$

Accordingly, the surface flux under Henry´s regime is given by:

$$J_s = -\rho D_s^0 K_0 \exp\left(\frac{\Delta H_{ads} - E_{a,s}}{\Re T}\right)\frac{dP}{dz} \tag{III.24}$$

The permeance through a microporous membrane may be found after integrating equation (III.24) over the membrane thickness:

$$\Pi_s \equiv \frac{J_s}{\Delta P} = \frac{\rho}{\delta} D_s^0 K_0 \exp\left(\frac{\Delta H_{ads} - E_{a,s}}{\Re T}\right) \tag{III.25}$$

As equation (III.25) shows, the permeance-temperature behavior under Henry's regime depends on the relative values of $E_{a,s}$ and ΔH_{ads}. The permeance will monotonically increase or decrease when the activation energy for diffusion is larger or smaller than the heat of adsorption, respectively .

1.4 Gas permeation through microporous membranes

It is generally found that both surface and activated gaseous diffusion mechanisms contribute to the overall mass transport through a microporous membrane. The degree to

which each mechanism contributes to the total permeation depends mainly on the adsorption properties of the system, as well as on the conditions of temperature and pressure (Dong *et al.*, 2000; Gardner *et al.*, 2002; Zah *et al.*, 2007). Moreover, in real membrane systems, Knudsen diffusion and/or viscous flow may be expected to contribute to the total permeation flux as well, owing to the presence of defects in the crystalline structure.

The fluxes from different diffusion mechanisms are additive. Accordingly, the total permeation flux through microporous membranes may be written as follows:

$$J_{\text{total}} = J_{\text{defects}} + J_{\text{micropores}} = J_{\text{v}} + J_{\text{Kn}} + J_{\text{s}} + J_{\text{g}} \tag{III.26}$$

It is worth noting that the effect of the support must be taken into account in the calculation of the effective J_{total}, since only a fraction of the total area is available for permeation. This obligates to multiply equation (III.26) by a support geometric factor, which is commonly associated to its porosity and tortuosity.

The transport mechanism controlling the permeation process may be discriminated from the permeance-temperature behavior, in agreement with the previous discussion. For instance, diffusion of non-adsorbable gases in micropores is expected to increase monotonically with temperature. However, a minimum in the permeance is frequently found at low temperatures, which can be ascribed to the presence of defects, since permeation flux resulting from both viscous and Knudsen mechanisms decreases with increasing temperature.

The transport of strongly adsorbing molecules at low or moderate temperatures is dominated by surface diffusion, while activated gaseous diffusion may prevail at high temperatures (van den Broeke *et al.*, 1999b; Zhu *et al.*, 2006; Gavalas, 2008). In this case, a maximum followed by a minimum in the permeance could be anticipated (Bakker *et al.*, 1997; Coronas *et al.*, 1997; Burggraaf *et al.*, 1998; van de Graaf *et al.*, 1998a). At low temperatures, permeance increases because the diffusivity of adsorbed molecules is enhanced by temperature, even though the surface coverage simultaneously decreases; at a given temperature, the decrease in the adsorbed concentration becomes the determining factor, so that the overall permeance will start to decrease. At higher temperatures,

adsorption could be negligible and permeance would be expected to exponentially increase, given the activated nature of diffusion through micropores (Nishiyama *et al.*, 2001). Once more a minimum in the permeance is commonly observed at lower temperatures, which may be attributed to an additional contribution of viscous and/or Knudsen mechanisms.

2. Multicomponent Diffusion

Multicomponent mass transport has been described based on three main approaches, namely, the Fickian formalism, the thermodynamics of irreversible processes (IT) theory, and the generalized Maxwell-Stefan (MS) equations.

The widely applied Fick's first law (equation (III.4)) may be generalized to describe multicomponent systems (Taylor and Krishna, 1993). However, these diffusivities do not have the same physical significance of the binary coefficients since they do not reflect pair interactions. Moreover, similarly to single component diffusion, for accurate modeling and theoretical understanding of multicomponent diffusion, it is convenient to adopt the more fundamental approach based the chemical potential gradients as the true driving force for diffusion (Krishna, 1990,1993; Krishna and Wesselingh, 1997; Smit and Maesen, 2008). Furthermore, in the presence of electrostatic or centrifugal force fields, Fick's first law cannot be properly applied (Krishna, 1990,1993; Krishna and Wesselingh, 1997).

As alternative to the generalized Fick's law, both the irreversible thermodynamics and the Maxwell-Stefan models express the diffusion fluxes in terms of chemical potential gradients and can include the effect of external force fields into the respective equations.

2.1 Thermodynamics of Irreversible Processes (IT)

Transport phenomena occur under the action of driving forces. While irreversible mass and heat fluxes take place, local equilibrium may be assumed, and a thermodynamic treatment may be valid near equilibrium under steady state conditions (Haase, 1969).

Transport through membranes may be described by thermodynamics of irreversible processes. During irreversible processes, under the action of a constant driving force, the free energy is continually dissipated and entropy is produced. Such entropy production provides a fundamental difference between irreversible and classical thermodynamics, where entropy is constant.

The derivation of the IT model involves three postulates (Bitter, 1991; Mulder, 1997), namely:

(1) The rate of entropy production in irreversible processes, σ, is calculated from the dissipation function, Ψ, which always has the form:

$$\Psi = T\sigma = \sum_i J_i X_i \geq 0 \tag{III.27}$$

where the J_i are generalized fluxes and X_i the appropriate (conjugate) generalized forces.

(2) Close to equilibrium, a linear dependence of the flux and the forces is assumed:

$$J_i = \sum_{j=1}^{m} L_{ij} X_j \tag{III.28}$$

where L_{ij} are the Onsager coefficients.

(3) Following the Onsager reciprocal relations, the coefficients L_{ij} are symmetric, i.e.:

$$L_{ij} = L_{ji} \tag{III.29}$$

For an isothermal binary system in the absence of any external forces, the driving force is the chemical potential gradient, $\nabla\mu$, and thus:

$$J_1 = -L_{11}\nabla\mu_1 - L_{12}\nabla\mu_2 \tag{III.30}$$

$$J_2 = -L_{21}\nabla\mu_1 - L_{22}\nabla\mu_2 \tag{III.31}$$

Diffusion flux equations derived from irreversible thermodynamics provide a real description for transport through membranes. Besides, the existence of coupling of driving forces and/or diffusion fluxes can be evidenced and clearly described (Bitter, 1991; Mulder, 1997). However, in this description the membrane is considered as a black box and no information is obtained or required about molecules permeation, which may limit the applicability of this approach concerning the membrane nature and separation mechanisms (Bitter, 1991; Mulder, 1997).

2.2 Maxwell-Stefan Equations

Maxwell-Stefan formalism is the most widely used approach to describe multicomponent diffusion. Although formally equivalent to the IT theory, it is recognized to be the most advantageous and preferable alternative (Krishna, 1990; Gardner *et al.*, 2002; Krishna, 2009).

MS model was originally developed for description of binary mixtures (Krishna, 1990,1993; Krishna and Wesselingh, 1997). Accordingly, in order to cause a relative motion between the two components of the mixture, a force must be exerted on each component. This force on molecule 1 is balanced by the friction between both species, which is proportional to their relative velocity, and to the molar fraction of the second molecule, x_2. The force balance is then given by:

$$-\nabla\mu_1 = \frac{\Re T}{Đ_{12}} x_2 (u_1 - u_2) \tag{III.32}$$

where u_1 and u_2 are velocities of 1 and 2, respectively, and $Đ_{12}$ is the Maxwell-Stefan diffusivity, which describes the interaction between both components; the term $\Re T / Đ_{12}$ may be interpreted as a drag coefficient between the molecules. Equation (III.32) may be combined with the definition of molar flux, i.e. $N_i = c_t x_i u_i$, to get:

$$-\frac{x_1}{\Re T}\nabla\mu_1 = \frac{x_2 N_1 - x_1 N_2}{c_t Đ_{12}} \tag{III.33}$$

being c_t the total molar concentration.

Since friction between different species is explicitly accounted by the Maxwell–Stefan theory, it may be especially suitable for describing multicomponent mass transport. The MS model presented for a binary mixture can thus be extended to a general multicomponent system. In this case, generalized MS equations express the balances between the chemical potential gradient of species i and the friction exerted on i by all other species j, according to:

$$-\frac{x_i}{\Re T}\nabla\mu_i = \sum_{\substack{j=1 \\ j\neq i}}^{n} \frac{x_j N_i - x_i N_j}{c_t Đ_{ij}} = \sum_{\substack{j=1 \\ j\neq i}}^{n} \frac{x_j J_i - x_i J_j}{c_t Đ_{ij}} \tag{III.34}$$

where $Đ_{ij}$ represents de interaction between each $i-j$ pair. From the Gibbs-Duhem restriction, $\sum_{i=1}^{n} x_i \nabla\mu_i = 0$, it follows that only $n-1$ of these equations are independent.

The driving force term in equation (III.34) may be expressed as function of the mole fraction gradients by introducing the thermodynamic factors, Γ_{ij}:

$$\frac{x_i}{\Re T}\nabla\mu_i = \sum_{j=1}^{n-1} \Gamma_{ij}\nabla x_j \text{, where } \Gamma_{ij} = \delta_{ij} + x_i \frac{\partial \ln \gamma_i}{\partial x_j} \qquad i, j = 1, 2, ..., n-1 \tag{III.35}$$

being γ_i the activity coefficient of species i in the mixture, which may be evaluated by thermodynamics models (e.g., the Wilson, NRTL, UNIQUAC, and UNIFAC models). For dense gas mixtures exhibiting deviations to the ideal gas behavior, fugacity coefficient may be used instead (Taylor and Krishna, 1993).

For simplicity, equation (III.34) can be combined with equation (III.35) and expressed in $n-1$ dimensional matrix form, explicitly written in terms of diffusion fluxes:

$$(J) = -c_t [B]^{-1} [\Gamma] (\nabla x) \tag{III.36}$$

being the elements of $[B]$ defined as follows:

$$B_{ii} = \frac{x_i}{Đ_{in}} + \sum_{\substack{k=1 \\ k \neq i}}^{n} \frac{x_k}{Đ_{ik}}, \quad B_{ij} = -x_i \left(\frac{1}{Đ_{ij}} - \frac{1}{Đ_{in}} \right) \tag{III.37}$$

By comparison of equation (III.36) with the generalized Fick´s law $(J) = -c_t [D] (\nabla x)$, it follows that Fick and Maxwell-Stefan coefficients are related by:

$$[D] = [B]^{-1} [\Gamma] \tag{III.38}$$

While Maxwell-Stefan diffusivity has a fundamental physical meaning of an inverse drag coefficient, Fick diffusivity couples the drag effects with thermodynamic non-ideality effects (Krishna, 1993). Hence, MS diffusivity may be more easily interpretable and predictable than Fick diffusivity. Besides, because of the strong composition dependence of thermodynamic factor, Fick diffusivity may be expected to exhibit strong composition dependence as well. For ideal systems it may be easily found that $[D] = [B]^{-1}$.

The superiority of the MS formalism in terms of physical interpretation of the corresponding diffusivities can be extended to the Onsager coefficients L_{ij} (Krishna, 2009). Nonetheless, Krishna and Wesselingh (1997) and Skoulidas *et al.* (2003) have shown that the three formalisms are equivalent since the coefficients of each formulation can be expressed in terms of the coefficients of any of the other two.

As aforementioned, several diffusion mechanisms can be distinguished within a porous material. In macro- and mesopores, viscous flow and/or Knudsen diffusion may occur; in mixtures, bulk or molecular diffusion is an additional mechanism. The *Dusty Gas Model* (DGM) (Jackson, 1977; Krishna, 1993) is the most widely used approach to describe combined bulk and Knudsen diffusion. The principle behind the DGM is to consider the porous solid as a collection of stationary giant molecules uniformly distributed in space. Those dust molecules are considered to be a pseudo-species in the multicomponent mixture, corresponding to the $(n+1)^{th}$ component. By combining this

principle with Maxwell-Stefan formulation, the following n independent equations may be obtained:

$$-\frac{x_i}{\Re T}\nabla\mu_i = \sum_{\substack{j=1 \\ j\neq i}}^{n}\frac{x_j N_i - x_i N_j}{c_t Đ_{ij}} + \frac{N_i}{c_t Đ_{i,Kn}} \tag{III.39}$$

where $Đ_{i,Kn}$ is the Knudsen diffusivity, defined as $Đ_{i,Kn} = Đ_{i,n+1}/x_{n+1}$, and reflects the molecule-wall collisions. In this case, the force exerted on species i is balanced by the sum of the friction forces between molecular species i and j (bulk diffusion) together with the friction between species i and the solid (Knudsen diffusion). Under the action of a pressure gradient, viscous flow will take place within the pores. Accordingly, the contribution from viscous mechanism may be included into the transport equation (Manson and del Castillo, 1985; Manson and Lonsdale, 1990; Krishna and Wesselingh, 1997):

$$-\frac{x_i}{\Re T}\nabla_{T,p}\mu_i - \frac{x_i}{\Re T}\overline{V}_i\nabla P - \alpha'_i\, x_i \frac{B_0}{\eta Đ_{iM}}\nabla P = \sum_{j=1}^{n}\frac{x_j N_i - x_i N_j}{c_t Đ_{ij}} + \frac{N_i}{c_t Đ_{i,Kn}} \tag{III.40}$$

where $\nabla_{T,p}\mu_i$ is the chemical potential gradient of i at fixed temperature and pressure, B_0 is the medium permeability, η is the mixture viscosity, ∇P is the pressure gradient, $\overline{V}_i$ is the partial molar volume of i, and α'_i is the viscous selectivity factor.

Transport across a composite membrane is a combination of diffusion through both the separation top layer and porous support. Because supports are generally macro and/or mesoporous, transport across them can be accurately described by equation (III.40), since it embodies the various mechanisms present.

Surface forces are dominant in microporous structures, where molecules never escape completely from the surface force field, even at the centre of the pore. By analogy with the DGM, diffusion of adsorbed species in micropores may be described assuming the surface vacant sites as a $(n+1)^{th}$ pseudo-species in the multicomponent system. As a result, surface diffusion can be described by (Krishna, 1990,1993; Krishna and Wesselingh, 1997):

$$-\frac{\theta_i}{\Re T}\nabla\mu_i = \sum_{\substack{j=1 \\ j\neq i}}^{n}\frac{\theta_j N_i^s - \theta_i N_j^s}{\rho_p \varepsilon q_{sat} Đ_{ij}^s} + \frac{N_i^s}{\rho_p \varepsilon q_{sat} Đ_i^s} \tag{III.41}$$

for molecules with equal q_{sat}, where ρ_p and ε are the matrix density and porosity, respectively. The chemical potential gradient, $\nabla\mu_i$, is the driving force for diffusion of species i along the surface. The first term on the right-hand side represents the friction exerted on species i by all the other components in the mixture, while the second term represents friction exerted by the surface on i. Coefficients $Đ_{ij}^s$ express the interaction between moving components i and j, in the same way as in bulk diffusion, and $Đ_i^s$, defined as $Đ_i^s = Đ_{i,n+1}^s/\theta_{n+1}$, reflects the molecule-wall interactions.

Similarly to the single gas diffusion, $Đ_i^s$ may be dependent on the surface loading. Assuming that a molecule can migrate from one site to another only when it is empty, a simple model to describe the loading dependence is $Đ_i^s = Đ_i^s(0)(1-\theta_1-\theta_2-...-\theta_n)$, where $Đ_i^s(0)$ is the diffusivity in the limiting case of vanishingly small occupancy (Krishna and Paschek, 2002; Krishna and Baur, 2004). Concerning $Đ_{ij}^s$, these coefficients should exhibit a coverage dependence between $Đ_i^s$ and $Đ_j^s$, which can be determined by the empirical Vignes correlation (Vignes, 1966), adapted to micropores diffusion by Krishna (1990):

$$Đ_{ij}^s = \left(Đ_j^s\right)^{\frac{\theta_j}{\theta_i+\theta_j}}\left(Đ_i^s\right)^{\frac{\theta_i}{\theta_i+\theta_j}} \tag{III.42}$$

Assuming equilibrium between the surface and bulk fluid, the surface chemical potential in equation (III.41) may be expressed in terms of gradients of surface occupancy by introducing the matrix of thermodynamics factors:

$$\frac{\theta_i}{\Re T}\nabla\mu_i = \sum_{j=1}^{n}\Gamma_{ij}\nabla\theta_j \text{ , where } \Gamma_{ij} = \theta_i\frac{\partial \ln f_i}{\partial\theta_j} \tag{III.43}$$

being f_i the fugacity of molecule i in the bulk fluid mixture. At low pressures, the components fugacity may be replaced by the partial pressures, i.e., $f_i = p_i$.

The thermodynamic factors, Γ_{ij}, are calculated based on the isotherms of each component. Extended Langmuir isotherm is one of the most popular adsorption models for two-component systems. This model usually provides a good data representation when saturation loadings of the two components are close. However, when saturation loadings differ significantly, extended Langmuir isotherms may not predict correctly the equilibrium data, particularly at high occupancies where adsorption of the component with higher saturation loading can prevail (van den Broeke *et al.*, 1999c; Kapteijn *et al.*, 2000a; Gavalas, 2008). Dual-site Langmuir (DSL) isotherms have been also adopted in modelling permeation of single component and binary mixtures, when two different adsorption sites are distinguished (Krishna *et al.*, 1998; Krishna and Paschek, 2000; Krishna and Baur, 2003; Krishna *et al.*, 2004; Gavalas, 2008). Alternatively, a model based on the ideal adsorbed solution theory (IAST), developed by Myers and Prausnitz (1965) and Ruthven (1984) has been also adopted by several authors (e.g., van den Broeke *et al.* (1999a), Kapteijn *et al.* (2000a), and Yu *et al.* (2007)). Similarly to the extended Langmuir isotherm, the IAST model can be used to predict multicomponent adsorption equilibrium based on single gas-adsorption isotherms only (van den Broeke *et al.*, 1999a; Zhu *et al.*, 2006; Gavalas, 2008). Kapteijn *et al.* (2000a) used the IAST model together with extended multicomponent diffusion equations to successfully describe the diffusion in mixtures of molecules with different saturation loadings.

Langmuir isotherm may be easily extended to describe N-component systems, according to the following relation:

$$\theta_i = \frac{q_i}{q_{sat}} = \frac{b_{L,i} p_i}{1 + \sum_{j=1}^{N} b_{L,j} p_j} \tag{III.44}$$

For the case of Langmuir regime, the thermodynamic factor reduces to:

$$\Gamma_{ij} = \delta_{ij} + \frac{\theta_i}{1 - \sum_{j=1}^{N} \theta_j} \tag{III.45}$$

where δ_{ij} is the delta of Kronecker.

Equations (III.41) and (III.43) may be combined and expressed in *n*-dimensional matrix form, leading to the final form of Maxwell-Stefan model to describe surface diffusion:

$$\left(N^{s}\right) = -\rho_{p}\varepsilon q_{sat}\left[B^{s}\right]^{-1}\left[\Gamma\right]\left(\nabla\theta\right) \tag{III.46}$$

being the elements of $\left[B^{s}\right]$ defined as follows:

$$B_{ii}^{s} = \frac{1}{Đ_{i}^{s}} + \sum_{\substack{j=1 \\ j\neq i}}^{n} \frac{\theta_{j}}{Đ_{ij}^{s}}, \quad B_{ij}^{s} = -\frac{\theta_{i}}{Đ_{ij}^{s}} \tag{III.47}$$

Mass transport of multicomponent mixtures may be predicted with Maxwell–Stefan equations based only on single components adsorption and diffusion data (van den Broeke *et al.*, 1999a; Zhu *et al.*, 2006). However, the individual contribution of each species in the mixture may differ significantly from its pure behavior, as, for instance, in the case of binary mixtures of a strong and weak adsorbable components. Although stronger adsorbates move slower than the weaker ones, their presence within small pores may create a barrier to the diffusion of the second ones, and hence hinder their transport across the membrane. As a result, an unexpected maximum may appear in the uptake profiles of the faster diffusing component (van den Broeke *et al.*, 1999a,b; Yang *et al.*, 1999).

2.3 Adsorption equilibrium

Several models are available in the literature providing appropriate descriptions for single and multicomponent adsorption equilibrium. For instance, Langmuir, Nitta, Freundlich, Langmuir-Freundlich, and Toth isotherms are frequently adopted models. In this section their main characteristics and mathematical representation for pure and multicomponent systems are presented, along with the temperature dependence of their parameters.

Langmuir theory has been the most widely used approach to describe equilibrium adsorption data in porous materials. This isotherm is a fundamental equation based on several basic assumptions, namely: i) adsorption on the surface is localized, i.e. molecules are adsorbed at a fixed number of well-defined localized adsorption sites; ii) each site can

accommodate only one adsorbate molecule; iii) all sites are energetically equivalent, which means that the surface is homogeneous; and iv) there is no interaction between molecules adsorbed on neighbouring sites.

The Langmuir model was developed based on a kinetic principle, assuming that the rate of adsorption is equal to the rate of desorption on the surface (Do, 1998). Accordingly, equation (III.16) may be obtained, which in the low pressure region reduces to the Henry law, and for sufficiently high pressures reaches the saturation capacity characteristic of the monolayer coverage. For N-component systems, Langmuir isotherm is:

$$\theta_{\mathrm{i}} = \frac{q_{\mathrm{i}}}{q_{\mathrm{sat}}} = \frac{b_{\mathrm{L,i}} p_{\mathrm{i}}}{1 + \sum_{j=1}^{N} b_{\mathrm{L,j}} p_{\mathrm{j}}} \tag{III.48}$$

For thermodynamic consistency of the extended Langmuir equation the saturation capacity of all species must be the same (Broughton, 1948).

The model of Nitta was derived by Nitta *et al.* (1984), based on statistical thermodynamics. This theory provides an extension of the Langmuir isotherm, assuming localized monolayer adsorption on the surface and allowing for multi-site adsorption, where each molecule may be adsorbed on n active sites (Do, 1998). The Nitta isotherm is given by:

$$n_{\mathrm{N}} b_{\mathrm{N}} P = \frac{\theta}{(1-\theta)^{n_{\mathrm{N}}}} \exp\left(-\frac{n_{\mathrm{N}} u \theta}{kT}\right) \tag{III.49}$$

where n_N is the number of sites occupied by one adsorbed molecule, u reflects the adsorbate-adsorbate interaction, and b_{N} is the adsorption affinity constant calculated by:

$$b_{\mathrm{N}} = b_{\mathrm{o}} \exp\left[\frac{Q_{\mathrm{N}}}{\Re T_{\mathrm{o}}}\left(\frac{T_{\mathrm{o}}}{T} - 1\right)\right] \tag{III.50}$$

For systems where the adsorbate-adsorbate interaction is not as strong as the adsorbate-adsorbent interaction, $u = 0$, and equation (III.49) simplifies to:

$$n_{\mathrm{N}} b_{\mathrm{N}} P = \frac{\theta}{(1-\theta)^{n_{\mathrm{N}}}} \tag{III.51}$$

In this case, Nitta isotherm reduces to the Langmuir equation when $n_{\mathrm{N}} = 1$.

Nitta isotherm may be also extended to describe multicomponent systems. When all interaction energies between adsorbed molecules are zero, the multicomponent isotherm equation is simply:

$$n_{\mathrm{N,i}} b_{\mathrm{N,i}} p_{\mathrm{i}} = \frac{\theta_{\mathrm{i}}}{\left(1 - \sum_{\mathrm{j=1}}^{\mathrm{N}} \theta_{\mathrm{j}}\right)^{n_{\mathrm{N,i}}}} \tag{III.52}$$

Similarly to the single gas isotherm, when all $n_{\mathrm{N,i}} = 1$, equation (III.52) reduces to the extended Langmuir equation.

Adsorbent materials generally exhibit a rather complex pore and surface structure. Consequently, fundamental adsorption isotherms, such as the classical Langmuir equation or the Nitta isotherm, may not accurately describe equilibrium. Accordingly, a number of semi-empirical approaches have been proposed. In the following, the Freundlich, Langmuir-Freundlich and Toth isotherm models will be briefly discussed.

The Freundlich isotherm is one of the most frequently equations used to describe equilibria. It may be represented by:

$$q = (b_{\mathrm{F}} P)^{1/n_F} \tag{III.53}$$

Here, b_{F} and n_{F} are temperature-dependent parameters; n_{F} usually lies in the range of 1 to 5, and the larger this constant is, the more nonlinear sorption becomes. In general, b_{F} decreases with temperature, and n_{F} approaches unit at high temperatures.

Freundlich isotherm may be adopted for energetically heterogeneous surfaces. However, it is generally valid only in a narrow range of pressure, since it does not exhibit a proper linear behaviour at low pressures and a finite limit for sufficiently high pressures. To overcome the restriction of continuous increase in the concentration of adsorbed

molecules, an empirical extension of the Freundlich equation, frequently called Langmuir-Freundlich isotherm, was proposed by Sips (1948):

$$\theta = \frac{q}{q_{sat}} = \frac{\left(b_{\mathrm{LF}} P\right)^{1/n_{\mathrm{LF}}}}{1+\left(b_{\mathrm{LF}} P\right)^{1/n_{LF}}} \tag{III.54}$$

where b_{LF} is the adsorption affinity constant, and n_{LF} characterises the surface heterogeneity. This last parameter is usually greater than unity, and the larger is its value the more heterogeneous the system is.

The temperature dependence of the Langmuir-Freundlich parameters may be expressed as follows:

$$b_{\mathrm{LF}} = b_{LF,\infty} \exp\left(\frac{Q_{\mathrm{LF}}}{\Re T}\right) = b_{\mathrm{LF,o}} \exp\left[\frac{Q_{\mathrm{LF}}}{\Re T_{\mathrm{o}}}\left(\frac{T_{\mathrm{o}}}{T}-1\right)\right] \tag{III.55}$$

$$1/n_{LF} = 1/n_{\mathrm{LF,o}} + \alpha_{\mathrm{LF}}\left(1 - T_{\mathrm{o}}/T\right) \tag{III.56}$$

where $b_{LF,\infty}$ is the adsorption affinity constant at infinite temperature, $b_{\mathrm{LF,o}}$ and $n_{\mathrm{LF,o}}$ are the parameters b_{LF} and n_{LF} at a reference temperature T_{o}, and α_{LF} is a constant. The temperature dependence of the saturation capacity can be represented by the following empirical relation:

$$q_{\mathrm{sat}} = q_{\mathrm{sat,o}} \exp\left[\chi_{\mathrm{LF}}\left(1 - T/T_{\mathrm{o}}\right)\right] \tag{III.57}$$

being $q_{\mathrm{sat,o}}$ and χ_{LF} the saturation capacity at the reference temperature T_{o}, and a constant parameter, respectively.

For multicomponent systems, equation (III.54) takes the form:

$$\theta_i = \frac{q_i}{q_{sat,i}} = \frac{\left(b_{\mathrm{LF,i}}\, p_i\right)^{1/n_{\mathrm{LF,i}}}}{1+\sum_{j=1}^{N}\left(b_{\mathrm{LF,j}}\, p_j\right)^{1/n_{LF,j}}} \tag{III.58}$$

Langmuir–Freundlich isotherm combines features of both Langmuir and Freundlich models. Nonetheless, this isotherm still does not follow the expected linear behaviour at

low pressures. In contrast, the Toth isotherm, given by equation (III.59), satisfies both low and high pressure limits:

$$\theta = \frac{q}{q_{sat}} = \frac{b_{\mathrm{T}} P}{\left[1 + \left(b_{\mathrm{T}} P\right)^{t}\right]^{1/t}} \tag{III.59}$$

where b_{T} and t are the Toth isotherm parameters. When $t = 1$, equation (III.59) reduces to the Langmuir equation. Similarly to the Langmuir-Freundlich isotherm, this parameter characterizes the system heterogeneity. The temperature dependence of b_{T} and q_{sat} may be equivalent to those of the Langmuir-Freundlich isotherm (please see equations (III.55) and (III.56)). Concerning parameter t, the following empirical relation may be assumed:

$$t_{\mathrm{i}} = t_{\mathrm{o}} + \alpha_{\mathrm{T}} \left(1 - T_{\mathrm{o}} / T\right) \tag{III.60}$$

where t_{o} is the parameter t at a reference temperature T_{o}, and α_{T} is a constant.

Similarly to the above discussed isotherms, also the Toth equation may be extended to multicomponent adsorption systems. A number of different approaches have been proposed in the literature for its multicomponent form, as, for instance, (i) that given by Jaroniec (1984).

$$\theta_{\mathrm{i}} = \frac{b_{\mathrm{T,i}}\, p_{\mathrm{i}}}{\left[1 + \sum_{j=1}^{N} \left(b_{\mathrm{T,j}}\, p_{\mathrm{j}}\right)^{t_i}\right]^{1/t_i}} \quad , \tag{III.61}$$

(ii) the modified Langmuir-Freundlich form adopted by Abdul-Rehman *et al.* (1990):

$$\theta_{\mathrm{i}} = \frac{b_{\mathrm{T,i}}\, p_{\mathrm{i}}}{\left[1 + \sum_{j=1}^{N} \left(b_{\mathrm{T,j}}\, p_{\mathrm{j}}\right)^{t_j}\right]^{1/t_i}} \tag{III.62}$$

or (iii) the extended model as used by Lamia *et al.* (2009):

$$\theta_{\mathrm{i}} = \frac{b_{\mathrm{T,i}}\, p_{\mathrm{i}}}{\left[1+\sum_{j=1}^{N}\left(b_{\mathrm{T,j}}\, p_{\mathrm{j}}\right)^{t_T}\right]^{1/t_T}} \tag{III.63}$$

In this last model, a global heterogeneity parameter, t_{T}, different from those specific for the single component isotherms, is used. It is calculated from the single component isotherms as:

$$t_{\mathrm{T}} = \sum_{i=1}^{N} y_{\mathrm{i}} t_{\mathrm{i}} \tag{III.64}$$

being y_{i} the gas molar fraction of i. The saturation capacities of different species in the extended Toth isotherm should also be the same in order to meet the thermodynamic consistency (Lamia *et al.*, 2009).

The ideal adsorbed solution (IAS) theory is an alternative approach to describe multicomponent adsorption equilibrium, in which the adsorbate mixture is treated as a two-dimensional solution in equilibrium with a gas phase. Several versions of the IAS theory have been proposed, such as the Myers and Prausnitz (1965) theory or the LeVan and Vermeulen (1981) approach for binary systems. This theory is thermodynamically consistent and provides an effective technique for estimating the adsorption equilibrium of a gaseous mixture, using uniquely the adsorption isotherms of the pure components.

The IAS theory of Myers and Prausnitz adopts the fundamental thermodynamic equations for liquids to the adsorbed phase. Accordingly, the general equilibrium relationship between gaseous and adsorbed phases may be expressed by an equation analogous to Raoult's law for vapour-liquid equilibria:

$$P y_{\mathrm{i}} = \theta_{\mathrm{i}} P_{\mathrm{i}}^{\mathrm{o}}(\pi), \text{ for } 1 = 1,2,...,\mathrm{N} \tag{III.65}$$

where y_{i} and θ_{i} are the molar fractions of component i in the fluid and adsorbed phases, respectively, P is the total pressure and P_i^{o} is the hypothetical pressure of the pure component i that gives the same spreading pressure, π, as the adsorbed mixture. The physical meaning of spreading pressure is analogous to that of a monomolecular film at the

gas-liquid interface. Thus π defines the lowering of the surface tension at the solid-gas interface upon adsorption (Yang, 1987). The spreading pressure may be calculated by the Gibbs adsorption isotherm:

$$\frac{A\pi}{\Re T} = \int_0^{P_1^o} \frac{q_1\left(P_1^o\right)}{P_1} dP_1 = \int_0^{P_2^o} \frac{q_2\left(P_2^o\right)}{P_2} dP_2 = \ldots = \int_0^{P_N^o} \frac{q_N\left(P_N^o\right)}{P_N} dP_N \tag{III.66}$$

where A is the surface area of the adsorbent, and $q_i\left(P_i^o\right)$ is the isotherm of the pure component i at the hypothetical pressure P_i^o. The total concentration of adsorbed molecules in the mixture, q_t, is obtained from:

$$\frac{1}{q_t} = \sum_{j=1}^{N} \frac{\theta_j}{q_j\left(P_j^o\right)} \tag{III.67}$$

The previous set of equations can not be solved analytically. In addition, although being widely considered as a simple and convenient tool to calculate multicomponent adsorption equilibria, the predictability of IAS theory is limited, which may be primarily due to the assumption of treating the adsorbed phase as one thermodynamic entity.

Different adsorption models may be found in literature to successfully describe single and binary sorption in zeolites. Barrer (1978) pointed out that the widely adopted Langmuir isotherm is usually suitable for zeolites, due to compensation effects, even for more heterogeneous systems. The dual-site Langmuir (DSL) model has also been used to describe isotherms that deviate from the conventional Langmuir behaviour, being especially suitable for fitting the equilibrium data of branched alkanes on silicalite-1 (Zhu *et al.*, 2000). DSL isotherms have been adopted in modelling permeation of single component and binary mixtures through zeolite membranes, when two different adsorption sites are distinguished (Krishna *et al.*, 1998; Krishna and Paschek, 2000; Krishna and Baur, 2003; Krishna *et al.*, 2004; Gavalas, 2008).

Abdul-Rehman *et al.* (1990) modelled pure and multicomponent equilibrium data for the adsorption of the first four n-alkanes on Linde S-115 silicalite using different isotherms explicit in partial pressure, namely the loading ratio correlation (Yon and Turnock, 1971), Toth isotherm (Jaroniec, 1984), Mathews and Weber (1980) isotherm, and the statistical

thermodynamic isotherm of Ruthven (1984). The extended Langmuir equation was found to describe the adsorption of ethane, methane, and ethane/methane mixture in silicalite-1, even though the saturation capacities of the single components were different. For propane/methane mixtures some deviations were found upon predicting mixture adsorption with the extended Langmuir equation, being the Toth isotherm the most adequate. Since in this case there were no kinks or steps in the mixture adsorption isotherms, which would be the case if surface heterogeneity would play a role, the extended Langmuir equation was considered a good approximation. According to the authors, the Toth model gives the best description for the adsorption of the first four alkanes in silicalite-1, for single components and some binary mixtures.

Rees *et al.* (1991) established a comparison between the Langmuir and the Langmuir-Freundlich models for the description of pure nitrogen, methane, and carbon dioxide in silicalite-1. The IAS theory with the Langmuir model for the pure component isotherms was used to describe the binary adsorption of nitrogen and carbon dioxide. A good description was found for the total concentration of adsorbed molecules, though the IAS predictions for the separation factor deviated significantly from the experimental results. A consistent description of the equilibrium adsorption was given by the Nitta model.

Buss and Heuchel (1997) describe the adsorption of binary mixtures of methane and tetrafluormethane in silicalite-1 using both the IAS theory, with Toth isotherm for the pure components, and the binary model of Nitta. Both models were found to provide a good description of the experimental data. The good results obtained were attributed to the high surface homogeneity as well as to the channel-like pore geometry of silicalite, where interactions between the adsorbate molecules can only occur to a small extent.

Seidel and Carl (1989) used the Freundlich, Dubinin-Radushkevich, Toth, and Langmuir-Freundlich isotherms for diffusion of phenol and indole from aqueous solution in activated carbon. The known simple relationship between surface diffusivity and adsorption energy proposed by Gilliland *et al.* (1974) were related to the isotherm on an energetically heterogeneous surface. The loading concentration dependence of surface diffusivity was calculated for each isotherm equation. The authors concluded that

isotherms do have a great influence on kinetics. This point is particularly emphasized in this thesis, as it will be discussed in section VI.1.

Li *et al.* (2007) tested the capability of the Maxwell-Stefan formulation to predict permeation fluxes of CO_2/CH_4, CO_2/N_2, and N_2/CH_4 mixtures across a SAPO-34 membrane using only data of pure-component adsorption isotherms and diffusivities. The authors concluded that for adsorption of pure gases in zeolite structures with cages separated by narrow windows, such as SAPO-34, the model based on statistical thermodynamics described by Ruthven (1984) may be particularly relevant. The mixture thermodynamics was estimated using the IAS theory of Myers and Prausnitz (1965).

IV. Modelling Ion Exchange in Microporous Titanosilicates

This chapter focuses the modelling of ion exchange in microporous titanosilicates based on the Maxwell-Stefan equations. First, a brief overview of the more classical kinetic models will be presented. Then, a more detailed description around the Nernst-Planck equations will be given. Finally, a detailed model based on the Maxwell-Stefan formulation will be developed to describe a batch ion exchange in microporous materials. The model equations will be solved numerically in order to fit and predict experimental data from literature. The cases studied to validate the proposed model consist in mercury (II) and cadmium (II) removal from aqueous solution using ETS-4 microporous titanosilicate. The capability of the proposed model to describe experimental data and its predictive capacity will be compared with those of the Nernst-Planck model, given its sound theoretical fundaments. To conclude, results obtained with the more frequently applied pseudo first- and pseudo second-order kinetic equations will be presented as well.

1. Introduction

Toxic metals are well known by their toxicology and tendency to accumulate in the living organisms and aquatic systems, causing serious diseases and disorders. They are mainly discharged into the aquatic system as industrial wastewaters, mainly from metal finishing, welding, alloy manufacturing plants, pulp industries and petroleum refining, endangering soil and water quality (Inglezakis *et al.*, 2002). Mercury and cadmium are two of the most

toxic non-essential metals present in the environment, even at low concentrations, and their persistence in the aquatic systems encourages the development of techniques to remove them. Ion exchange is probably one of the most attractive processes, being commonly used in industry because of its simple and efficient application. This technique is effective to remove even traces from solutions and is particularly useful for treating large volumes of dilute solutions (Dabrowski *et al.*, 2004). Natural and synthetic zeolites are gaining considerable interest as ion-exchangers because of their high selectivity and capacity (Biskup and Subotic, 2004; Ahmed *et al.*, 2006; Trgo *et al.*, 2006a). A number of titanosilicates have recently been used as ion exchangers for toxic metals removal. For instance, ETS-10 has been shown to have high selectivity for several toxic metals such as Pb^{2+}, Cu^{2+}, Cd^{2+}, Co^{2+}, Mn^{2+}, Zn^{2+} (Choi *et al.*, 2006; Lv *et al.*, 2007; Camarinha *et al.*, 2009) and some radiocations (Pavel *et al.*, 2003). Moreover, Bortun *et al.* (1997) evaluated framework and layered titanosilicates for cesium and strontium uptake from contaminated groundwater and wastewater; Decaillon *et al.* (2002) studied the ion exchange selectivity of layered titanosilicate AM-4 toward strontium; Koudsi and Dyer (2001) studied a synthetic titanosilicate analog of the mineral penkvilsite-2O, i.e. AM-3, for removal of Cobalt-60; and Lopes *et al.* (2007,2009) evaluated the potential of synthetic microporous (ETS-4, ETS-10, and AM-2) and layered (AM-4) titanosilicates for decontamination of natural waters polluted with low mercury levels. These results induced us to develop in this thesis a Maxwell-Stefan formulation for the ion exchange fluxes in microporous titanosilicates.

As stated in Chapter II, microporous titanosilicates are crystalline solids with a well defined structure formed by a three-dimensional combination of tetrahedral and octahedral building blocks. Each TiO_6 octahedron in the titanosilicate global structure carries a -2 charge, which can be neutralized by extra-framework cations (usually Na^+ and K^+). These compensation species, as well as water molecules or other adsorbed molecules, are located in the channels of the structure and can be replaced by others (e.g., Hg^{2+} and Cd^{2+}). The framework anionic sites are typically divalent, which should be particularly useful for the exchange of divalent ions.

Modelling and simulation are useful tools to study and design a chemical plant. It is fundamental to be able to predict the dynamic behaviour of any unit, optimize their

operating conditions, and scale up from laboratory to large scale. Such goals may be accomplished by computer simulation in order to reduce the number of indispensable experiments. The validity of a model is not only the result of a good fitting but also its ability to predict the behaviour of a process under operating conditions apart from those used to obtain its parameters. Such principle guided the development of our model.

2. Classical Models

The kinetic performance of an ion exchange process is frequently interpreted by semiempirical pseudo first- and second-order equations (Namasivayam and Senthilkumar, 1998; Ho and McKay, 1999a,b; Reddad *et al.*, 2002; Chiron *et al.*, 2003; Yardim *et al.*, 2003; Aksu, 2005; Zhang *et al.*, 2005; Lopes *et al.*, 2007; Lopes *et al.*, 2009)). However, such models have no theoretical background, which limits their application and extrapolation

Mass transport in dilute ionic systems can be effectively described by the Nernst-Planck (NP) equations (Smith and Dranoff, 1964; Chanda and Rempel, 1995; Dolgonosov *et al.*, 1995; Patzay, 1995; Rodriguez *et al.*, 1998; Samson and Marchand, 1999; Varshney and Pandith, 1999; Rodriguez *et al.*, 2002; Varshney *et al.*, 2003; Valverde *et al.*, 2004,2005; Cincotti *et al.*, 2006). In an electrolyte solution, the electrical field induced by the different mobility of counter ions produces an additional force responsible for the transference of ions. The Nernst-Planck Equations account for both concentration and electric potential gradients. However, according to this model, the interdiffusion coefficients of counter ions are composition-dependent and the ionic interactions (ion-ion, ion-solvent, and ion-ion exchanger) are lumped into effective diffusivities (Helfferich, 1995). Furthermore, Nernst-Planck does not take non-ideality effects and the pressure gradient into account (Helfferich, 1995; Wesselingh *et al.*, 1995).

Some authors represent experimental data with analytical models devised specifically for particle diffusion control or film diffusion control under well defined conditions, as for instance infinite solution volume or constant diffusion rate and radial diffusion coefficient.

However, such conditions generally never hold in practice (Liberti *et al.*, 1978; Helfferich, 1995; Trgo *et al.*, 2006a,b). For this reason, such models will be not included in this study.

2.1 Pseudo-first order model

The pseudo-first order rate equation of Lagergren (1898) is one of the most widely used kinetic models to express the ion exchange mechanism. The Lagergren equation was the first rate equation for sorption of liquid/solid system based on the solid capacity. It may be represented by:

$$\frac{dq}{dt} = k_1(q_e - q) \tag{IV.1}$$

where k_1 is the rate constant of the first order sorption, q_e is the sorbed solute concentration at equilibrium, and q is the concentration at any time t. Integrating equation (IV.1) for $t = 0$ to $t = t$, and $q = 0$ to $q = q$, and rearranging to get a linear form, one obtains:

$$\ln(q_e - q) = \ln(q_e) - kt \tag{IV.2}$$

In order to fit equation (IV.2) to experimental data, the equilibrium sorption capacity, q_e, must be known. The constant k_1 can be determined by plotting $\ln(q_e - q)$ *versus* t. The parameter $\ln(q_e)$ is expected to be equal to the intercept of the $\ln(q_e - q)$ *vs* t representation; however, this is often not the case.

2.2 Pseudo-second order model

The pseudo-second order rate equation is also based on the sorption capacity of the solid and can be written as:

$$\frac{dq}{dt} = k_2 \left(q_e - q\right)^2 \tag{IV.3}$$

where k_2 is the rate constant of the second order sorption. Integrating equation (IV.3) for the previous boundary conditions, and rearranging in a linear form, it can be expressed as:

$$\frac{t}{q} = \frac{1}{k_2 q_e^2} + \frac{1}{q_e} t \tag{IV.4}$$

In this case, k_2 can be determined by plotting t/q *versus* t.

2.3 Nernst-Planck based model

Ion exchange is a stoichiometric process in which an ion from a solution is replaced by an equivalent amount, in terms of electrical charges, of another ionic species from a solid phase. This process may be represented by conventional chemical equilibrium between two counter ions (Helfferich, 1995). For the case where the zeolite is initially in B form and the counter ion in solution is A, the reaction is:

$$z_A \overline{B^{z_B}} + z_B A^{z_A} \Leftrightarrow z_B \overline{A^{z_A}} + z_A B^{z_B} \tag{IV.5}$$

where z_A and z_B are the electrochemical valences, and the upper bars identify the solid phase.

An electric field in an electrolyte solution, caused by the different mobilities of counter ions, produces an additional force responsible for the transference of ions. In contrast to the classical Fick's law, the Nernst-Planck model does account for the influence of this electric field. Hence, the flux of each counter ion in dilute ionic solutions may be described by the Nernst-Planck equations (Helfferich, 1995):

$$N_A = -D_A \left(\frac{\partial q_A}{\partial r} \right) - D_A z_A q_A \frac{F}{\Re T} \left(\frac{\partial \phi}{\partial r} \right) \tag{IV.6}$$

$$N_{\mathrm{B}} = -D_{\mathrm{B}}\left(\frac{\partial q_{\mathrm{B}}}{\partial r}\right) - D_{\mathrm{B}} z_{\mathrm{B}} q_{\mathrm{B}} \frac{F}{\Re T}\left(\frac{\partial \phi}{\partial r}\right). \tag{IV.7}$$

where D_{A} and D_{B} are the self-diffusion coefficients of species A and B, q_{A} and q_{B} are the molar concentration of counter ions in the particle, F is Faraday constant, $\Re$ is gas constant, T is absolute temperature, ϕ is the electrostatic potential and r is the radial position.

In the following development, the particle is assumed to be subjected to the restrictions of electroneutrality and nonexistent electric current, mathematically represented by:

$$q_{\mathrm{A}} z_{\mathrm{A}} + q_{\mathrm{B}} z_{\mathrm{B}} = Q \tag{IV.8}$$

$$z_{\mathrm{A}} N_{\mathrm{A}} + z_{\mathrm{B}} N_{\mathrm{B}} = 0\,. \tag{IV.9}$$

where Q is the ion exchanger capacity. The electrostatic potential term in the transport equations may be eliminated by substituting equations (IV.6) and (IV.7) in equation (IV.9):

$$\frac{F}{\Re T}\frac{\partial \phi}{\partial r} = \frac{z_{\mathrm{A}}\left(D_{\mathrm{B}} - D_{\mathrm{A}}\right)}{z_{\mathrm{A}} q_{\mathrm{A}}\left(z_{\mathrm{A}} D_{\mathrm{A}} - z_{\mathrm{B}} D_{\mathrm{B}}\right) + D_{\mathrm{B}} z_{\mathrm{B}} Q}\frac{\partial q_{\mathrm{A}}}{\partial r} \tag{IV.10}$$

After substitution in equation (IV.10), the general expression for the flux of A is obtained:

$$N_{\mathrm{A}} = -\frac{D_{\mathrm{A}} D_{\mathrm{B}}\left(z_{\mathrm{B}}^2 q_{\mathrm{B}} + z_{\mathrm{A}}^2 q_{\mathrm{A}}\right)}{D_{\mathrm{A}} z_{\mathrm{A}}^2 q_{\mathrm{A}} + D_{\mathrm{B}} z_{\mathrm{B}}^2 q_{\mathrm{B}}}\left(\frac{\partial q_{\mathrm{A}}}{\partial r}\right) \tag{IV.11}$$

This equation may be recast as a special form of the Fick's first law, where a coupled interdiffusion coefficient, D_{AB}, appears:

$$N_{\mathrm{A}} = -D_{\mathrm{AB}}\left(\frac{\partial q_{\mathrm{A}}}{\partial r}\right), \quad \text{and} \quad D_{\mathrm{AB}} \equiv \frac{D_{\mathrm{A}} D_{\mathrm{B}}\left(z_{\mathrm{A}}^2 q_{\mathrm{A}} + z_{\mathrm{B}}^2 q_{\mathrm{B}}\right)}{D_{\mathrm{A}} z_{\mathrm{A}}^2 q_{\mathrm{A}} + D_{\mathrm{B}} z_{\mathrm{B}}^2 q_{\mathrm{B}}}\,. \tag{IV.12}$$

D_{AB} depends on D_{A}, D_{B}, and on the ionic concentration of the zeolite, which varies in the course of ion-exchange.

3. Maxwell-Stefan Formulation

An alternative approach to describe an ion exchange process deals with the application of the Maxwell-Stefan (MS) equations, due to their well documented advantages in mass transport (Krishna, 1990,1993; Krishna and Wesselingh, 1997) (see detailed description in Chapter III). However, in the case of porous structures, such formulation has been essentially applied to non-ionic systems, particularly in gas phase (van de Graaf *et al.*, 1999; Kapteijn *et al.*, 2000a). In the last years, some papers concentrate on the application of MS theory to mass transfer in membrane electrolysis process (e.g., van der Stegen (1999) and Hogendoorn *et al.* (2001)) and electrodialysis (Kraaijeveld *et al.*, 1995). The MS equations do take into account and distinguish both ion-ion and ion-solid interactions, and they have been proved to be more effective in predicting ion exchange than the above mentioned Nernst-Planck relationships (Graham and Dranoff, 1982a,b; Pinto and Graham, 1987; Wesselingh *et al.*, 1995). Furthermore, under the scope of MS formalism, one diffusivity coefficient is defined for each pair of components, being dependent on their properties only. In addition, these coefficients are only weakly dependent on composition.

3.1 Maxwell-Stefan based model

In this section, the intraparticle resistance to ion exchange in microporous materials is described using the generalized MS equations (e.g., Krishna and Wesselingh (1997)) subjected to the following assumptions: i) Surface diffusion is the only transport mechanism, since due to the very small pore diameters ions never escape from the force field of the matrix co-ions, mainly due to the strong and long range nature of the electrostatic interactions. ii) The solid matrix is considered to be a uniform distribution of fixed ionic charges corresponding to the $(n+1)^{\text{th}}$ component, through which counter ions diffuse. Therefore, $u_{n+1}=0$, as in the well known Dusty Gas Model (Jackson, 1977; Krishna and Wesselingh, 1997), already described in Chapter III.

Considering the abovementioned assumptions, the MS transport equation for species i in multicomponent ionic systems is:

$$-\nabla\mu_{\mathrm{i}} - Fz_{\mathrm{i}}\nabla\phi = \sum_{\substack{j=1 \\ j\neq i}}^{n} \frac{y_{\mathrm{j}}\Re T(u_{\mathrm{i}} - u_{\mathrm{j}})}{Đ_{\mathrm{ij}}} + \frac{y_{\mathrm{s}}\Re T u_{\mathrm{i}}}{Đ_{\mathrm{is}}} \tag{IV.13}$$

where $\nabla\mu_{\mathrm{i}}$ is the surface chemical potential gradient of i, z_{i} is the charge of component i, $Đ_{\mathrm{ij}}$ is the common MS surface diffusivity of pair i - j, $Đ_{\mathrm{is}}$ is the MS surface diffusivity corresponding to the interaction between i and the fixed ionic charges (subscript s stands for solid), $y_{\mathrm{j}} = q_{\mathrm{j}}/q_{\mathrm{t}}$ is molar fraction of counter ion j, $y_{\mathrm{s}} = Q/q_{\mathrm{t}}$ is molar fraction of fixed charged groups, q_{j} is the molar concentration of j, and q_t is the total concentration of ionic species. It should be noted that $\sum_{i=1}^{n+1} y_{\mathrm{i}} = 1$, and q_{t} is not constant whenever counter ions have different electrochemical valences. Taking into account the definition of molar flux of the ionic species j,

$$N_{\mathrm{j}} = q_{\mathrm{t}} y_{\mathrm{j}} u_{\mathrm{j}} \tag{IV.14}$$

equation (IV.13) may be recast as:

$$-\frac{y_{\mathrm{i}}}{\Re T}\nabla\mu_{\mathrm{i}} - y_{\mathrm{i}} z_{\mathrm{i}} \frac{F}{\Re T}\nabla\varphi = \sum_{\substack{j=1 \\ j\neq i}}^{n} \frac{y_{\mathrm{j}} N_{\mathrm{i}} - y_{\mathrm{i}} N_{\mathrm{j}}}{q_{\mathrm{t}} Đ_{\mathrm{ij}}} + \frac{y_{\mathrm{s}} N_{\mathrm{i}}}{q_{\mathrm{t}} Đ_{\mathrm{is}}} \tag{IV.15}$$

Assuming equilibrium between exchanger and bulk solution, (i.e., $\mu_{\mathrm{i}} = \mu_{\mathrm{i,sol}}$), $\nabla\mu_i$ can be expressed in terms of the molar fraction gradients of counter ions in the particle by:

$$\frac{y_{\mathrm{i}}}{\Re T}\nabla\mu_{\mathrm{i}} = \sum_{j=1}^{n} \Gamma_{\mathrm{ij}} \nabla y_{\mathrm{j}}\,, \quad \text{with } \Gamma_{\mathrm{ij}} \equiv y_{\mathrm{i}} \frac{\partial \ln\left(\gamma_{\mathrm{i,sol}} x_{\mathrm{i}}\right)}{\partial y_{\mathrm{j}}} \tag{IV.16}$$

where $\gamma_{\mathrm{i,sol}}$ is activity coefficient of counter ion i in solution, Γ_{ij} is thermodynamic factor, $x_{\mathrm{i}} = C_{\mathrm{i}}/C_{\mathrm{t}}$ and C_{i} are molar fraction and concentration of i in solution, and C_{t} is total concentration of ionic species in bulk solution. It is worth noting that in equation (IV.16) x_{i} and y_{i} are related by equilibrium isotherm (e.g., equation (IV.34) below).

Equation (IV.15) can be expressed in n-dimensional matrix notation. Introducing the matrix of thermodynamic factors, $[\Gamma]$, given by equation (IV.16) one obtains:

$$-q_t[\Gamma](\nabla y)-q_t(\nabla\xi)=[B](N) \tag{IV.17}$$

or

$$(N)=-q_t[B]^{-1}[\Gamma](\nabla y)-q_t[B]^{-1}(\nabla\xi) \tag{IV.18}$$

where:

$$B_{ii}=\frac{y_s}{Đ_{is}}+\sum_{\substack{j=1\\ j\neq i}}^{n}\frac{y_j}{Đ_{ij}}, \qquad B_{ij}=-\frac{y_i}{Đ_{ij}} \tag{IV.19}$$

$$\nabla\xi_i=y_i z_i\frac{F}{\Re T}\nabla\phi. \tag{IV.20}$$

Under conditions of electroneutrality and nonexistent electric current the following relations are adhered to:

$$\sum_{i=1}^{n+1}q_i z_i=0 \tag{IV.21}$$

$$\sum_{i=1}^{n+1}z_i N_i=0. \tag{IV.22}$$

Equations (IV.18) and (IV.22) may be combined to eliminate $\nabla\phi$ from the generalized MS equations. As a result, the mass transport process in a mixture of $n+1$ components can be described by the following set of equations:

i) $n-1$ Maxwell-Stefan equations for components 1 to $n-1$ [equation (IV.18)];

ii) One reference condition (bootstrap relation):

$$N_{n+1}=0 \text{ or } u_{n+1}=0. \tag{IV.23}$$

iii) The no current relationship, equation (IV.22).

In the particular case of this study, there are three components with interest: counter ions Hg^{2+} or Cd^{2+} and Na^{+}, and the solid particle (i.e., fixed charges); solution co-ions are neglected due to Donnan effect. Hence, the equations available are: one MS equation (equation (IV.18)), the bootstrap relation (equation (IV.23)), and the no current restriction (equation (IV.22)). Furthermore, the electrostatic potential gradient obtained from equations (IV.18) and (IV.22) is:

$$\varphi = \frac{-\sum_{i=1}^{n} z_i \left(\sum_{j=1}^{n} L_{ij} \nabla y_j \right)}{\sum_{i=1}^{n} y_i z_i \left(\sum_{i=1}^{n} z_j L_{ji} \right)} \tag{IV.24}$$

which gives for our case:

$$\frac{F}{\Re T} \nabla \phi = \frac{-z_A \left[L_{11} \left(\Gamma_{11} \nabla y_A + \Gamma_{12} \nabla y_B \right) + L_{12} \left(\Gamma_{21} \nabla y_A + \Gamma_{22} \nabla y_B \right) \right] - z_B \left[L_{21} \left(\Gamma_{11} \nabla y_A + \Gamma_{12} \nabla y_B \right) + L_{22} \left(\Gamma_{21} \nabla y_A + \Gamma_{22} \nabla y_B \right) \right]}{y_A z_A^2 L_{11} + y_B z_A z_B L_{12} + y_A z_A z_B L_{21} + y_B z_B^2 L_{22}} \tag{IV.25}$$

where $[L] = [B]^{-1}$. The thermodynamic factors simplify, since the activity coefficients calculated were very nearly unitary.

3.2 Material balances, initial and boundary conditions, and equilibrium isotherms

The models developed to describe batch ion exchange embody the following hypothesis: i) there exist film and intraparticle mass transfer resistances; ii) spherical solid particles; iii) perfectly stirred tank; iv) isothermal operation; v) liquid and solid volume changes are neglected; (vi) co-ions are excluded from the zeolite particles (Donnan exclusion); (vii) effect of competitive ions (e.g. H^{+}) is neglected and (viii) ideal solution. Concerning diffusing components, A is the pollutant to remove from solution, Hg^{2+} or Cd^{2+}, using the ion-exchanger (ETS-4) initially in B – form (Na^{+}).

Material Balances and initial and boundary conditions

Considering the above assumptions, the mass balances in the particle and in the reservoir are:

$$\left(\frac{\partial q_A}{\partial t}\right) = -\frac{1}{r^2}\frac{\partial}{\partial r}\left(r^2 N_A\right) \tag{IV.26}$$

$$\frac{d\,C_A}{dt} = -\frac{V_s}{V_L}\frac{d\,\overline{q}_A}{dt}\,. \tag{IV.27}$$

where the average loading per unit particle volume is calculated by:

$$\overline{q}_A = \frac{3}{R^3}\int_0^R r^2 q_A\, dr\,. \tag{IV.28}$$

The variables R, V_s, and V_L represent particle radius, volume of solid phase, and volume of fluid phase, respectively.

The following initial and boundary conditions are used. The initial conditions (no B in solution, no A in zeolite) are:

$$t = 0, \qquad \begin{cases} q_A = \overline{q}_A = 0 \\ C_A = C_{A,0} \end{cases} \tag{IV.29}$$

and the boundary conditions are the interface concentration and the null central flux condition:

$$r = R, \qquad q_A = q_{A,R} \tag{IV.30}$$

$$r = 0, \qquad \left(\frac{\partial q_A}{\partial r}\right) = 0\,. \tag{IV.31}$$

The concentration at the interface is uniquely determined by equalizing internal diffusion and film convection fluxes, i.e.:

$$N_A A\big|_{r=R} = A\,k_f\left(C_A - C_{A,R}\right) \tag{IV.32}$$

where k_f is the convective mass transfer coefficient, and A is the external particle surface area. For well established agitated systems, it is possible to estimate k_f using correlations which depend generally on the Reynolds, Schmidt and Power numbers, and on geometrical parameters such as the ratio of impeller to tank diameter, the specific geometry of the impeller, and the geometry of baffling, if any, used to inhibit vortex formation in the vessel. Several correlations and more references may be found elsewhere (Treybal, 1981; Misic *et al.*, 1982; Kulov *et al.*, 1983; Miller *et al.*, 1984; Slater, 1991).

The correlation of Armenante and Kirwan (1989) may be used to estimate the convective mass transfer coefficient, at least to predict its order of magnitude, due to its simplicity and because it was specifically derived for microparticles in agitated systems:

$$Sh = 2 + 0.52Re^{0.52}Sc^{1/3} \tag{IV.33}$$

where $Sh = k_f d_p / D_{Aw}$ is the Sherwood number, d_p is the particle diameter, D_{Aw} is the diffusivity of the solute in solution, $Re = \varepsilon^{1/3} d_p{}^{4/3} / \nu$ is the Reynolds number, ε is the mixer power input per unit of fluid mass, ν is the kinematic viscosity, and $Sc = \nu / D_{Aw}$ is the Schmidt number. This equation is frequently applied to fix k_f in the model equations or, alternatively, to estimate k_f and compare it with the optimized value from experimental data (Fernandez and Carta, 1996; Bhattacharya, 2007).

Equilibrium Isotherms

In order to describe the system behavior, both kinetics and adsorption equilibrium have to be simultaneously taken into account. The equilibrium between bulk solution and ion-exchanger were evaluated in this work using the Freundlich isotherm, given the good equilibrium representation achieved. Freundlich isotherm can be represented by:

$$q_A = K_F C_A^{1/n_F} \tag{IV.34}$$

Here, K_F and n_F are temperature-dependent parameters; n_F usually lies in the range of 1 to 5, and the larger this constant is, the more nonlinear sorption becomes. In general, K_F decreases with temperature, and n_F approaches unit at high temperatures (Do, 1998).

3.3 Solution approach: numerical methods used

The simultaneous solution of the set of differential and algebraic equations listed above gives the concentration of counter ions in the fluid, and their concentration profiles in the solid phase as function of position and time. The model has been solved numerically using the Method of Lines (Schiesser, 1991) and integrated by the finite-difference approach. For that purpose, a program in Matlab has been written to solve the resulting Ordinary Differential Equations (ODEs) with 101 grid points and finite-difference approach with central differences of second order; forward and backward differences formulas were adopted for the first and last nodes, respectively. The average loading per unit particle volume (equation (IV.28)) is numerically evaluated using the 1/3 Simpson's Rule. Ode15s has been used to integrate this set of ODEs of the initial-value type.

The self-diffusion coefficients and the convective mass transfer coefficient are the model parameters to fit to the experimental data. Accordingly, a first optimization step was performed based on the 'elimination of linear parameters in nonlinear regression' technique due to Lawton and Sylvestre (1971). With this procedure, a reduction of the number of parameters that must be estimated by the iterative procedure is achieved, as well as faster convergence attained. Finally, an enhancing optimization involving all parameters simultaneously was performed, where the results previously obtained from the above mentioned technique were taken as reliable initial guesses.

3.4 Data used to validate MS based model

The validity of the proposed model was examined using experimental data measured in the University of Aveiro, concerning batch experiments where mercury (II) and cadmium (II) ions are removed from aqueous solution using ETS-4 microporous titanosilicate (Ferreira

et al., 2009; Lopes *et al.*, 2009). Totally, eight experiments are considered, corresponding to the conditions listed in Table IV.1 and Table IV.2. In those works the bulk concentration of Hg^{2+} and Cd^{2+} has been measured along time. Table IV.3 compiles relevant physical properties of ETS-4 particles used in the experiments.

Table IV.1 – Experimental conditions of data used in calculations for Hg^{2+} removal (Lopes *et al.*, 2009).

Experimental Conditions	Exp.1	Exp.2	Exp.3	Exp.4
Temperature, K	295 ± 1			
Solution volume, $10^{-3}\ m^3$	2			
Initial Hg^{2+} conc., $10^{-3}\ kg/m^3$	50			
Mass of ETS-4, $10^{-6}\ kg$	1.63	5.06	8.02	12.20

Table IV.2 – Experimental conditions of data used in calculations for Cd^{2+} removal (Ferreira *et al.*, 2009).

Experimental Conditions	Exp.5	Exp.6	Exp.7	Exp.8
Temperature, K	295 ± 1			
Solution volume, 10^{-3} m^3	2			
Initial Cd^{2+} conc., 10^{-3} kg/m^3	0.51	0.64	0.84	0.62
Mass of ETS-4, 10^{-6} kg	44	50	51	100

Table IV.3 – Physical properties of ETS-4 titanosilicate.

Formula	$[Na_9Ti_5Si_{12}O_{38}(OH).12H_2O]$
Density, kg/m^3	2200
Ion exchanger capacity, eq/kg	6.39
Particle diameter, 10^{-6} m	0.5 – 0.9
Pore diameter, 10^{-10} m	3 – 4

4. Discussion

Results obtained with the MS based model proposed in this work are shown in Figures IV.1 and IV.2, plotted in $C_A(t)/C_{A0}$ *versus* time and $\overline{q}_A(t)$ *versus* time forms, along with experimental data. Table IV.4 displays the calculated parameters, namely MS diffusivities and film mass transfer coefficient optimized, and the average absolute relative deviations $(AARD)$ found. The figures point out the good agreement between model results and experiments of Tables IV.1 and IV.2, confirmed by the low deviations found, $AARD = 5.49\%$ and $AARD = 6.41\%$, respectively, which are well inside the experimental accuracy reported (5-8%). The accurate correlation accomplished in the transition from steep descent to horizontal branch is noteworthy in both cases, once in liquid-solid sorbent processes the elbow of the kinetic curves is frequently most difficult to fit.

The diffusion coefficients fitted (Table IV.4) are in the order of $10^{-20} - 10^{-18}$ m^2s^{-1}, which are consistent with both the small pore diameters of ETS-4 (0.3-0.4 nm), and the strong and long range nature of the electrostatic interactions, following other values in literature. For instance, Barrer and Rees (1960) reported self-diffusion coefficients of 1.14×10^{-17}, 1.96×10^{-21}, and 8.27×10^{-26} m^2s^{-1} for Na^+, K^+ and Rb^+ in analcite, repectively; apparent diffusion coefficients of 1.8×10^{-17} and 8.0×10^{-18} m^2s^{-1} were obtained by Coker and Rees (2005) for Ca^{2+} and Mg^{2+} in semi-crystalline zeolite Na-A, respectively; Brooke and Rees (1969) reported interdiffusion diffusivities in the range of $10^{-18} - 10^{-19}$ m^2s^{-1} for the system Na^+/K^+ in shabazite; and Coker and Rees (1992) reported interdiffusion coefficients of 2.00×10^{-18} and 6.53×10^{-18} m^2s^{-1} for Na^+/Ca^{2+} and Na^+/Mg^{2+} in beryllophosphate. Ahmed *et al.* (2006) published an estimated Cd^{2+} apparent diffusion coefficient of 2.84×10^{-23} m^2s^{-1} in CaX zeolite, based on an intraparticle diffusion model neglecting external diffusion resistances. However, the simulation achieved with such coefficient was comparatively poor relatively to that obtained by simply fitting a first-order kinetic model to the experimental data.

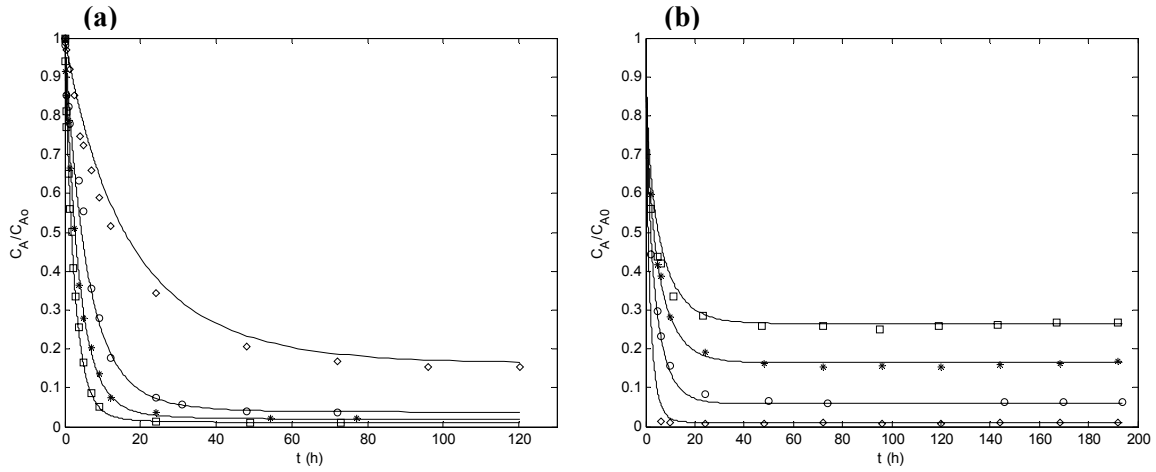

Figure IV.1 – Plot of the normalized concentration of cation in the bulk solution *versus* time: modelling and experimental data for (a) Hg^{2+} removal; experimental conditions (see Table IV.1): ◊, Exp.1; ○, Exp.2; *, Exp.3 and □, Exp.4; and (b) Cd^{2+} removal; experimental conditions (see Table IV.2): □, Exp.5; *, Exp.6; ○, Exp.7 and ◊ Exp.8.

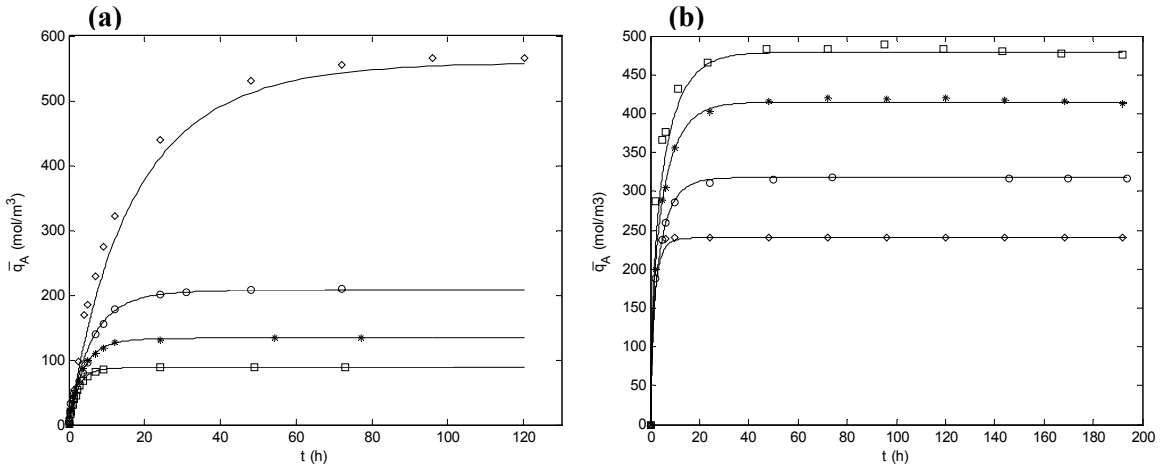

Figure IV.2 – Plot of the average particle concentration *versus* time: modelling and experimental data for: (a) Hg^{2+} removal and (b) Cd^{2+} removal. Experimental conditions: same as Figure IV.1.

The MS diffusivities of the pairs Hg^{2+}/fixed ionic charges and Cd^{2+}/fixed ionic charges (i.e., $Đ_{As}$) are very close, which could evidence the interaction between each ion and titanosilicate fixed ionic charges is similar. Concerning the Na^{+}/fixed ionic charges pair, the MS diffusivities ($Đ_{Bs}$) obtained for both Hg^{2+} and Cd^{2+} systems are expected to be the same, given the binary nature of those coefficients; however, they were shown to differ

by one order of magnitude. Such discrepancy could be ascribed to some model assumptions which could be not entirely suitable. For instance, the effect of competition between H^+ and Hg^{2+} or Cd^{2+} towards titanosilicate sorption sites at low pH has not been taken into account. Moreover, a relative inaccuracy associated with determination of such coefficients is frequently found in literature. For instance, Gebremedhin-Haile *et al.* (2003) published data for diffusion coefficients of Hg^{2+} in natural and modified zeolites, with an associated error of the same magnitude.

Table IV.4 – Calculated results with the MS based model of this work: parameters optimized and average absolute deviation.

	Maxwell-Stefan				
	$Đ_{As}$, m^2s^{-1}	$Đ_{Bs}$, m^2s^{-1}	$Đ_{AB}$, m^2s^{-1}	k_f, ms^{-1}	$AARD$, %
Hg^{2+}	3.309×10^{-18}	1.927×10^{-19}	5.863×10^{-20}	4.808×10^{-3}	5.49
Cd^{2+}	3.099×10^{-18}	2.314×10^{-18}	2.108×10^{-19}	1.263×10^{-3}	6.41

The convective mass transfer coefficient fitted were 4.81×10^{-3} and 1.28×10^{-3} ms^{-1}, while those predicted by Armenante and Kirwan correlation were 2.90×10^{-3} and 2.20×10^{-3} ms^{-1}, for mercury and cadmium uptake calculations, respectively. This is a reliable result since some parameters used in the correlation were not entirely appropriate for the specific experimental set-up, namely, the power was approximately calculated, and the size of ETS-4 particles ($d_p = 0.7\times10^{-6}$ m) is one order of magnitude lower than the inferior limit studied by Armenante and Kirwan (range of $d_p = (6-420)\times10^{-6}$ m).

In Figure IV.3 the normalized concentration of mercury (II) in ETS-4 is graphed as function of time and radial position, for Experiment 2 of Table IV.1. Similar behaviour is found for the remaining experiments. This plot confirms expected trends, nonetheless it is interesting to detach the time evolution of normalized concentration at surface, $q_A(t;r=R)/q_{A,eq}$. As Figure IV.3 illustrates, initial sudden rise of surface concentration is so pronounced that it goes through a maximum and than decreases gradually until equilibrium is reached. Inside particle, far from surface, monotonous behaviour is found

instead. With no film resistance, the initial particle concentration at surface would change suddenly from $q_A\left(t=0^-, r=R\right)=0$ to $q_A\left(t=0^+, r=R\right)=q_A\left(C_{A0}\right)$, which is the concentration in equilibrium with bulk solution. Then, for $t>0$, $q_A\left(t, r=R\right)$ would decrease monotonously until final system equilibration, i.e. $q_A(t,r) \to q_{A,eq} = q_A(t=\infty, r)$. Figure IV.3 illustrates such behaviour, but the existence of external diffusion smoothes the ideal trend identified with initial step increase.

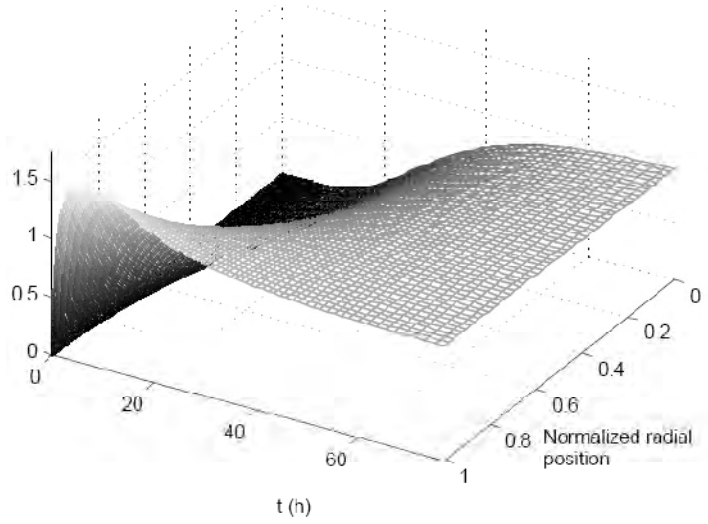

Figure IV.3 – Simulation results obtained for Exp.2 (Table IV.1) graphed as normalized concentration of the particle as function of time and normalized radial position.

The predictive capability of the model proposed in this chapter has been also analyzed. With that purpose, the parameters involved ($Đ_{As}$, $Đ_{Bs}$, $Đ_{AB}$, k_f) were optimized using one set of experimental data independently (namely, Exp.4 and Exp.7, for mercury and cadmium experiments, respectively). Afterwards the remaining curves were predicted with those parameters. The results obtained may be found in Table IV.5, and demonstrate the model is able to predict ion exchange behaviour for different experimental conditions. Please verify the moderate increments of the *AARDs* when we go from correlation to prediction: $AARD = 6.21 \to 6.29\%$ and $AARD = 6.70 \to 6.96\%$, for Hg^{2+} and Cd^{2+} removal data, respectively. Figure IV.4 shows the theoretical curves provided by our

model: full lines correspond to the base case of global correlation, whereas dashed lines are predictions obtained according to this procedure. As may be observed, fitted and predicted curves are very close, being almost superimposed for the Hg^{2+} system, so corroborating fine prediction potential.

Table IV.5 – Analysis of predictive capability of the MS and NP based models.

		Maxwell-Stefan		**Nernst-Planck**	
		Optimization	Prediction	Optimization	Prediction
Hg^{2+}	*AARD* Exp.1	7.34	7.58	6.86	7.05
	AARD Exp.2	5.44	5.37	5.61	5.45
	AARD Exp.3	5.68	5.82	5.72	5.83
	AARD Exp.4	3.56	-	3.53	-
	Global *AARD*	5.49/ 6.21*	6.29	5.39 / 6.08*	6.13
Cd^{2+}	*AARD* Exp.5	7.56	5.67	7.07	5.86
	AARD Exp.6	2.81	4.27	2.87	3.83
	AARD Exp.7	5.67	-	6.63	-
	AARD Exp.8	11.25	12.49	12.11	12.47
	Global *AARD*	6.41 / 6.70**	6.96	6.74/ 6.79**	6.86

* Global *AARD* for experiments 1 to 3.
** Global *AARD* for experiments 5, 6 and 8

In Figure IV.5, a comparison between results obtained with MS and NP based models, plotted in $C_A(t)/C_{A0}$ *versus* time form, is established. Table IV.6 compiles the calculated values involved, namely NP self-diffusion coefficients, the mass transfer coefficient, and average absolute deviations (*AARD*) found. Figure IV.5 clearly points out the similar fitting capability both models exhibit to represent experimental data, which can be confirmed by the similar deviations found.

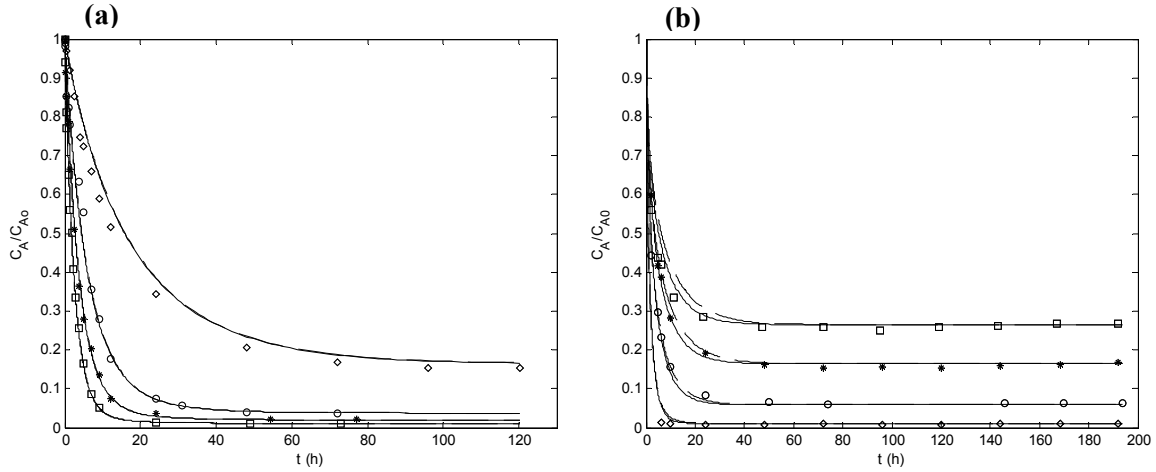

Figure IV.4 – Analysis of the prediction ability of the proposed MS based model: (a) Hg^{2+} removal and (b) Cd^{2+} removal. Full lines are simulations achieved optimizing all data; dashed lines are predictions obtained with parameters independently fitted to one set of experimental data alone. Note: in figure (a) both curves overlap.

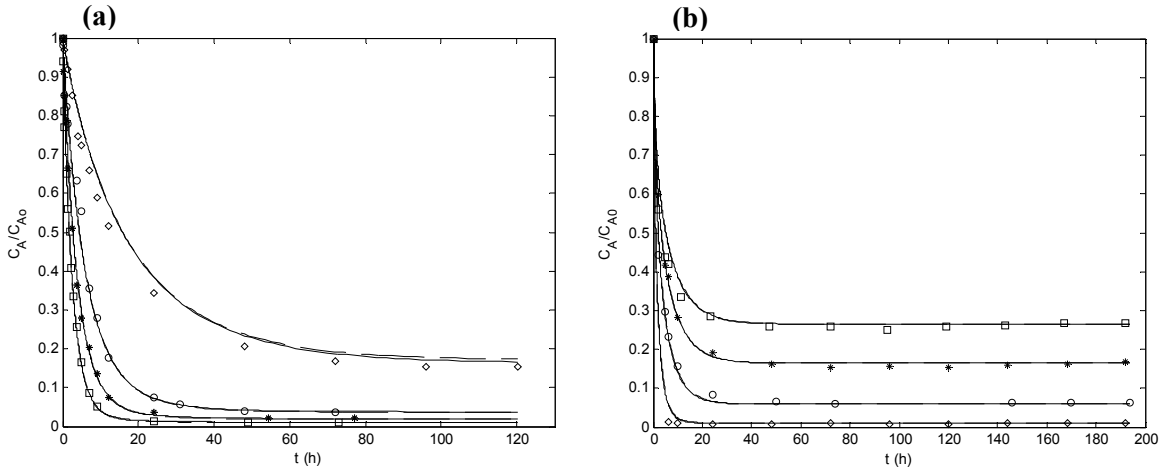

Figure IV.5 – Plot of normalized concentration of bulk solution *versus* time for (a) Hg^{2+} removal and (b) Cd^{2+} removal. Full and dashed lines are representations achieved optimizing all data with MS and NP based models, respectively. Experimental conditions: same as Figure IV.1.

The diffusion coefficients optimized with both models (Table IV.4 and Table IV.6) possess the same order of magnitude (i.e., $10^{-20} - 10^{-18}$ m^2s^{-1}). It should be noted, however, that MS and NP diffusivities do not have to be identical because of their distinct intrinsic

physical meaning: MS diffusivities characterize the interaction between each pair of species in the mixture, including the solid fixed ionic charges, whereas NP self diffusion coefficients represent the mobility with which counter ions diffuse in the ion-exchanger. Moreover, the calculated convective mass transfer coefficients are almost the same, i.e., 4.808×10^{-3} m.s^{-1} and 4.791×10^{-3} m.s^{-1}, for Hg^{2+} removal experiments, and 1.263×10^{-3} m.s^{-1} and 1.286×10^{-3} m.s^{-1}, for Cd^{2+} experiments, respectively. This fact emphasizes the good modelling results achieved.

Table IV.6 – Calculated results with the NP based model: parameters optimized and average absolute deviation.

	Nernst-Planck			
	D_A [$m^2 s^{-1}$]	D_B [$m^2 s^{-1}$]	k_c [$m\,s^{-1}$]	$AARD$ [%]
Hg^{2+}	1.130×10^{-19}	1.135×10^{-18}	4.791×10^{-3}	5.39
Cd^{2+}	2.595×10^{-19}	2.434×10^{-18}	1.280×10^{-3}	6.74

The predictive capability of both models may be also compared in Figure IV.7, where the MS and NP simulations of three sets of experiments obtained with parameters optimized from a distinct fourth experiment are graphed. It is possible to conclude that both models perform similarly, as NP and MS predicted curves practically overlap. The $AARDs$ of correlations and predictions are compiled in Table IV.5, and evidence both models offer good predictions with modest global deviations increments over those corresponding to correlation: $AARD_{MS} = 6.21 \rightarrow 6.29\,\%$ and $AARD_{NP} = 6.08 \rightarrow 6.13\,\%$, for Hg^{2+} experiments, and $AARD_{MS} = 6.70 \rightarrow 6.96\,\%$ and $AARD_{NP} = 6.79 \rightarrow 6.86\,\%$, for Cd^{2+} experiments. With respect to the individual $AADs$ (for each experiment), they are equally ordered, i.e. $AARD_{NP,4} < AARD_{NP,2} < AARD_{NP,3} < AARD_{NP,1}$ and $AARD_{MS,4} < AARD_{MS,2} < AARD_{MS,3} < AARD_{MS,1}$, for Hg^{2+} removal experiments, and $AARD_{NP,6} < AARD_{NP,7} < AARD_{NP,5} < AARD_{NP,8}$ and $AARD_{MS,6} < AARD_{MS,7} < AARD_{MS,5} < AARD_{MS,8}$ for Cd^{2+} removal experiments. Nonetheless, Nernst-Planck based model

results are still slightly better. In the whole, under the conditions investigated, both approaches can be applied successfully to describe intraparticle ionic transport. Such reliable performance must rely on the sound physical principles of the Maxwell-Stefan approach and on the theoretically fundamentals of the NP equations for dilute systems.

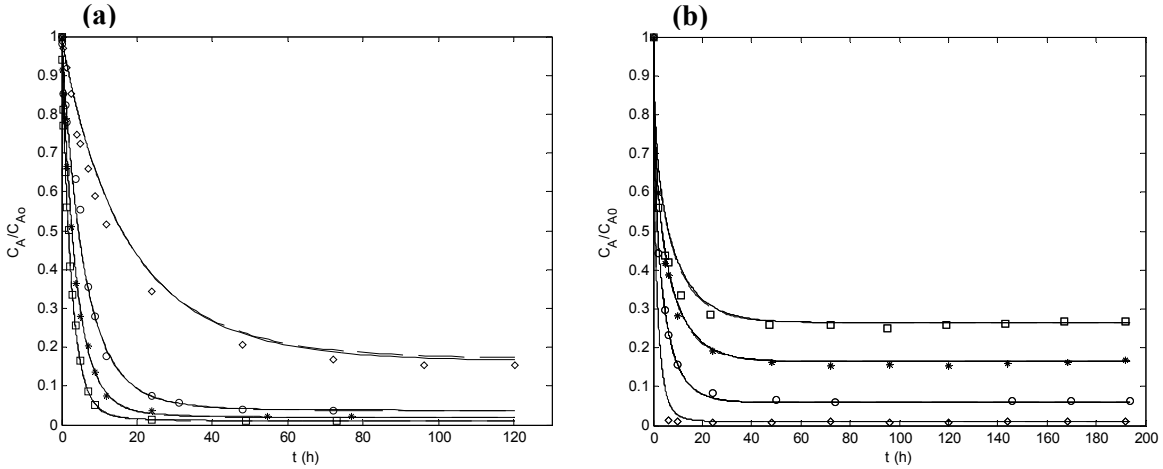

Figure IV.6 – Comparison of the prediction ability of the proposed MS based model with the NP model for: (a) Hg^{2+} removal and (b) Cd^{2+} removal. Full and dashed lines are predictions with parameters independently fitted to one set of experimental data alone with MS and NP based models, respectively. Experimental conditions: same as Figure IV.1.

Experimental data were also analyzed according to pseudo first- and pseudo second-order models, for comparison. Table IV.7 compiles the deviations found with MS based model, NP based model, pseudo first-order and pseudo second-order models. With respect to the pseudo first- and second-order equations, results show they provide poor representations of the fluid concentration ($AARDs = 12.11 - 215.73\%$) although they continue to be frequently used in this field, certainly because of their simplicity.

Figures IV.7 and IV.8 illustrate the distribution of the calculated deviations, for each model, over the normalized concentration of mercury and cadmium ions, respectively. A superiority of Maxwell-Stefan and Nernst-Planck based models over pseudo first- and pseudo second-order models to describe experimental data is clearly notorious, mainly over the pseudo first-order model.

Table IV.7 – Average absolute deviations (%) calculated for the models studied in this work.

	Maxwell-Stefan based model	**Nernst-Planck based model**	**Pseudo 1st-order model**	**Pseudo 2nd-order model**
Hg^{2+}	5.49	5.39	58.22	49.93
Cd^{2+}	6.41	6.74	215.73	12.11

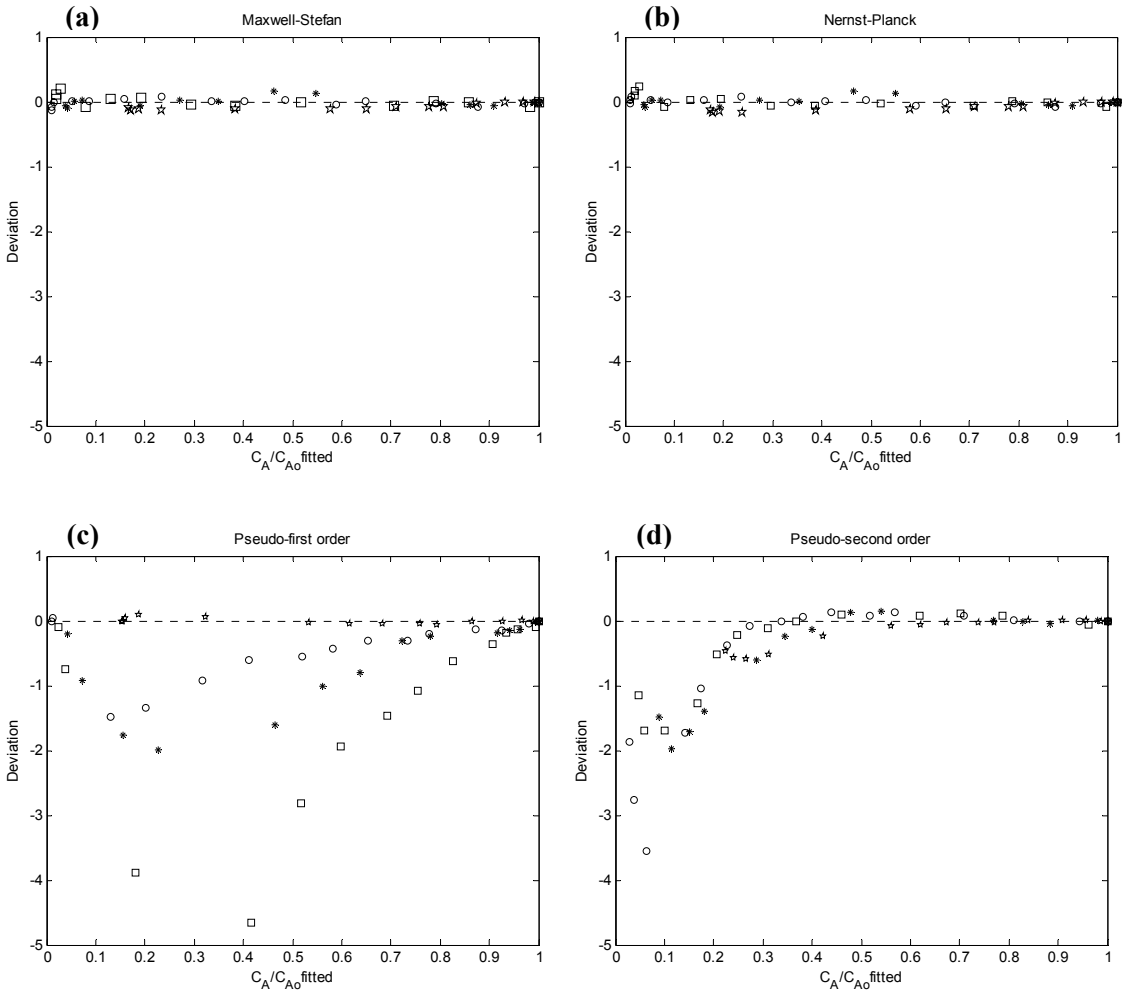

Figure IV.7 – Plot of the calculated deviations *versus* corresponding normalized Hg^{2+} concentration in bulk solution for: (a) Maxwell-Stefan model; (b) Nernst-Planck model; (c): pseudo first-order model; and (d): pseudo-second order model.

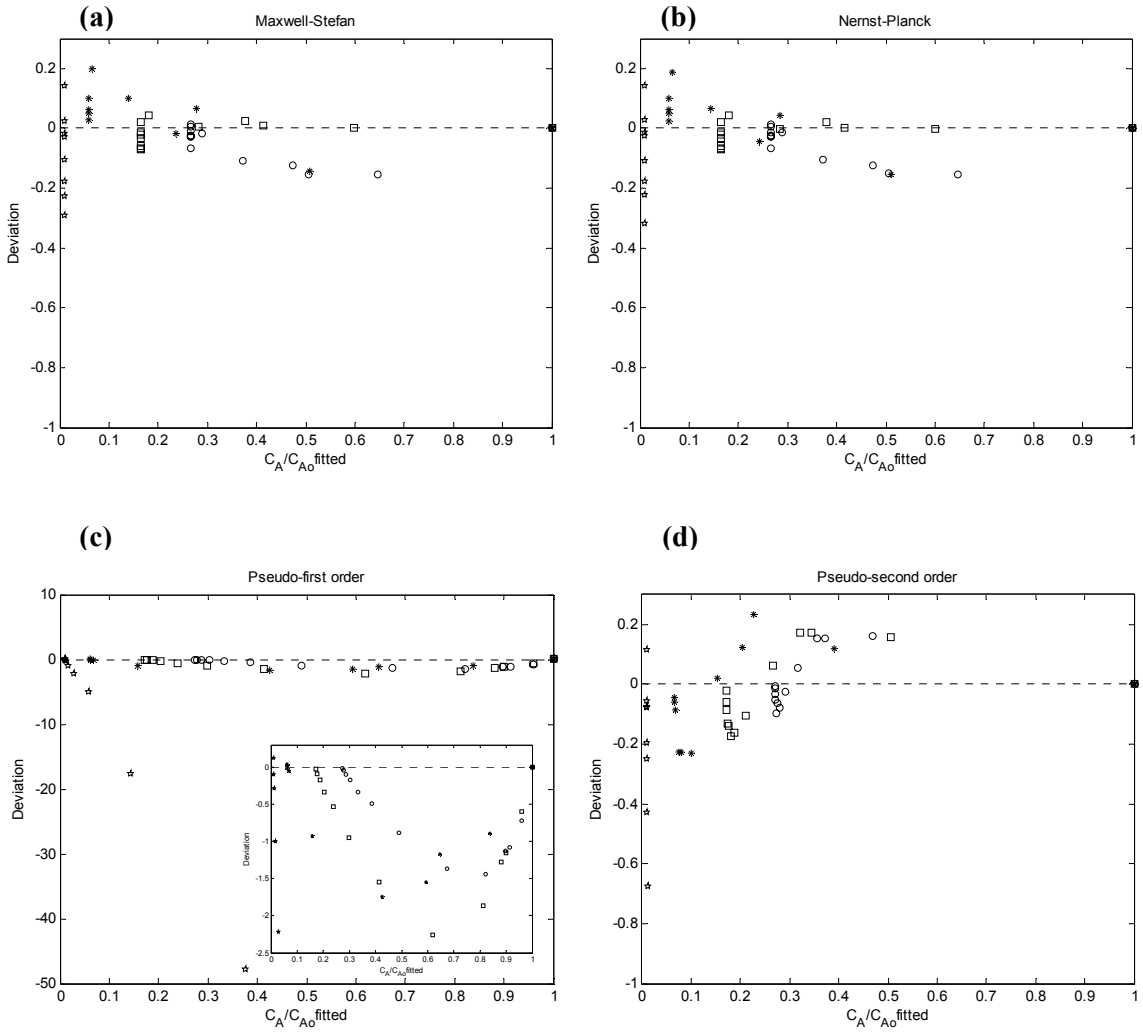

Figure IV.8 – Plot of the calculated deviations *versus* corresponding normalized Cd^{2+} concentration in bulk solution for: (a) Maxwell-Stefan model; (b) Nernst-Planck model; (c): pseudo first-order model; and (d): pseudo-second order model.

These plots show that the deviations corresponding to the Maxwell-Stefan and Nernst-Planck models are more uniformly distributed along the predicted concentration range. Moreover, the similarity between both models can be confirmed once again. On the other hand, deviations found for the second order model are particularly pronounced in the range of lower predicted concentration, which are considerably lower than the experimental ones. The magnitude of the first-order model deviations is significantly higher along the entire range of concentrations (please note the y-axis scale of Figure IV.8c, particularly the onset of the figure), being those concentrations systematically underestimated.

5. Final remarks

In this chapter a model based on the Maxwell-Stefan formulation has been developed to describe ion exchange in microporous materials. The MS approach has been adopted due to their well documented advantages over Nernst-Planck relationships, particularly because it takes account of ion-ion and ion-solid. The model accounts for external (film) and intraparticle diffusion control; their parameters are the MS diffusivities of each pair of species (counter ions and fixed charges of the particle) and the film mass transfer coefficient.

The model was validated with batch experiments on mercury (II) and cadmium (II) removal from aqueous solution using ETS-4 microporous titanosilicate (pore diameters between 0.3-0.4 nm). In this case the relevant species are Hg^{2+} or Cd^{2+} and Na^{+} (initially in solution and in ETS-4, respectively), and titanosilicate ionic fixed charges. Results obtained provide good representations of metal ions concentration in solution and solid phase along time. Even the transition from the steep descent to the horizontal branch of C_A/C_{A0} *versus* time curve is well represented, precisely where kinetic curves are most difficult to fit.

The predicting ability of the MS based model was analyzed, being possible to conclude it exhibits good predictive capacity. In effect, good predictions are accomplished with parameters optimized from an independent set of data. Such performance may be attributed to the sound physical principles of Maxwell-Stefan theory.

A comparison between Nernst-Planck and Maxwell-Stefan based models has been accomplished. The results obtained reveal that both models provide similar data representation, as well as fine predictive capability. The advantageous of the Maxwell-Stefan description, which arise particularly from taking into account ion-ion and ion-solid interactions, are not distinguished in this comparison. Such result can be ascribed to the experimental conditions used, namely dilute ionic solutions and binary exchange. Although, in principle, it is expected theoretically that these models will behave differently in concentrated solutions and in multicomponent systems; Nernst-Planck equations lump ionic interactions (ion-ion, ion-solvent, and ion-ion exchanger) into effective diffusivities and are not able to take non-ideality effects into account.

A research team at University of Aveiro is carrying out new experiments to study ion exchange in more concentrated solutions as well as competition effects with multicomponent mixtures and titanosilicates. Accordingly, it will be interesting to validate the performance of the proposed MS based model for simultaneous Hg^{2+} and Cd^{2+} ion exchange, and analyze its behaviour for concentrated solutions, where the Nernst-Planck model is expected to fail.

V. Experimental Section

The study of membranes permeation properties is fundamental for their characterization. Membrane quality should be assessed by measuring permeances of individual gases as well as separation factors of mixtures.

The permeation of certain molecules, at room temperature, can be used to detect rough defects in the membrane structure since over enhanced fluxes denunciate the presence of defects. The ideal selectivity, calculated as the ratio between the corresponding individual permeances, could give an idea of the membrane quality as well: ideal selectivities close to the Knudsen value (equal to the square root of molecular weighs ratio inverse) evidence meso-defects since in mesoporous systems Knudsen diffusion is the dominant transport mechanism. Moreover, the behaviour of permeation flux with temperature or pressure allows the discrimination between the different transport mechanisms involved and the subsequent detection of defects. Finally, the separation of real mixtures allows a real investigation of the membrane performance.

In the present work, gases with different molecular dimensions were selected in order to study transport through the micropores. For that purpose, an experimental set-up was designed, assembled and tested to carry out permeation experiments with single gases and mixtures at fixed and programmed temperature, under several transmembrane pressure differences. This chapter describes in detail the experimental set-up and procedures adopted for the dynamic characterization of membranes.

1. Experimental set-up

An experimental set-up was designed and assembled in order to carry out single gas permeation measurements as well as mixture separations. Figure V.1 shows some pictures of the experimental apparatus, which consists essentially of:

(i) a stainless-steel membrane module (manufactured at the University of Aveiro) used to accommodate the membrane (see Figure V.1a);

(ii) a tubular electric oven (manufactured at the University of Aveiro) coupled with a PID temperature controller (TC) (Eurotherm, Type 818) which allows the regulation of temperature and heating rate; a double thermocouple (Omega, Type K, CASS-IM15U-300-DUAL) is introduced inside the membrane and simultaneously connected to the temperature controller and to a data acquisition system (see Figure V.1c);

(iii) three mass flow controllers (MFC) (ALicat, MC-500SCCM-D/5M) used to control the mass flow of feed and sweep gases (Figure V.1b);

(iv) a mass flow meter (MFM) (ALicat, M-500SCCM-D) used to measure the permeate flow (see Figure V.1b);

(v) a back pressure regulator (BPR) (ALicat, PC-100PSIG-D/5P) used to measure and regulate the pressure at the retentate side, controlling in this way the transmembrane pressure difference (see Figure V.1b);

(vi) a pressure transducer (PT) (ALicat, P-100PSIG-D), placed before the MFM, to measure the permeate pressure (see Figure V.1b);

(vii) 16 electric solenoid valves (V1–V16) (Mega Control) to open and close the gas lines of the experimental set-up; gases are fed to the system and flow through the set-up in 1/4” and 1/8” stainless-steel and polypropylene tubing (see Figure V.1b);

(viii) a gas detector (GD) (Oldham MX 2100), essential to detect any gas leakage when inflammable or toxic gases are studied. In this case, a fan is also used to support efficient ventilation near the equipments (see Figure V.1c).

(ix) a gas chromatograph (GC) (DANI 1000 DPC), with a thermal conductivity detector (TCD), equipped with two separation capillary columns: a ValcoPLOT Molesieve 0.5×30 5A column for permanent gases, and a ValcoPLOT HayeSep D 0.5×30 column for CO_2 separation (see Figure V.1d).

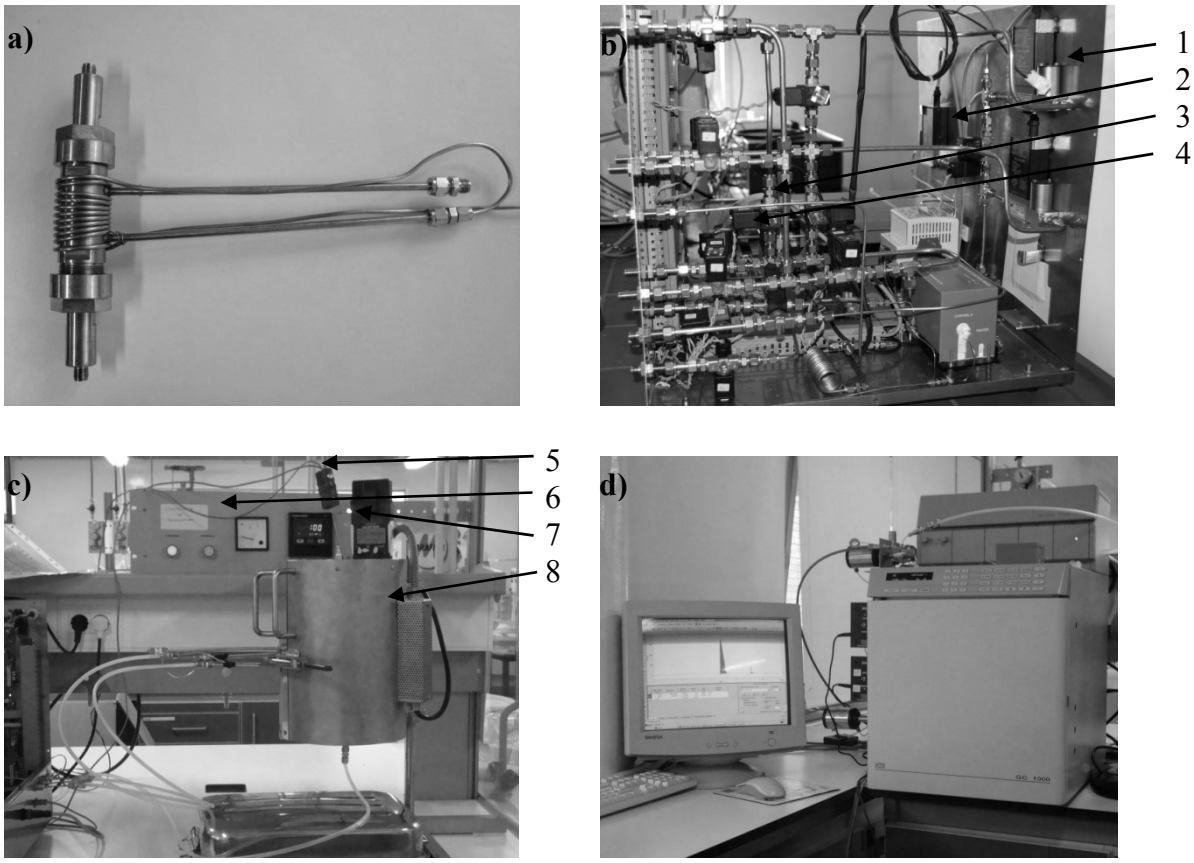

Figure V.1 – Experimental set-up used for permeation measurements. a) membrane module; b) 1 – mass flow controller (MFC), 2 – back pressure regulator (BPR), 3 – mass flow meter (MFM), 4 – pressure transducer (PT); c) 5 – thermocouple, 6 –temperature controller (TC), 7 – gas detector (GD), 8 – electric oven; d) gas chromatograph.

A graphical interface was developed using the LabVIEW software (National Instruments) in order to exchange information with the experimental set-up, i.e., to send/get information to/from the several set-up components. The RS-485 communication protocol was used for that purpose. Figures V.2 and V.3 show the LabVIEW user interface windows developed in this work.

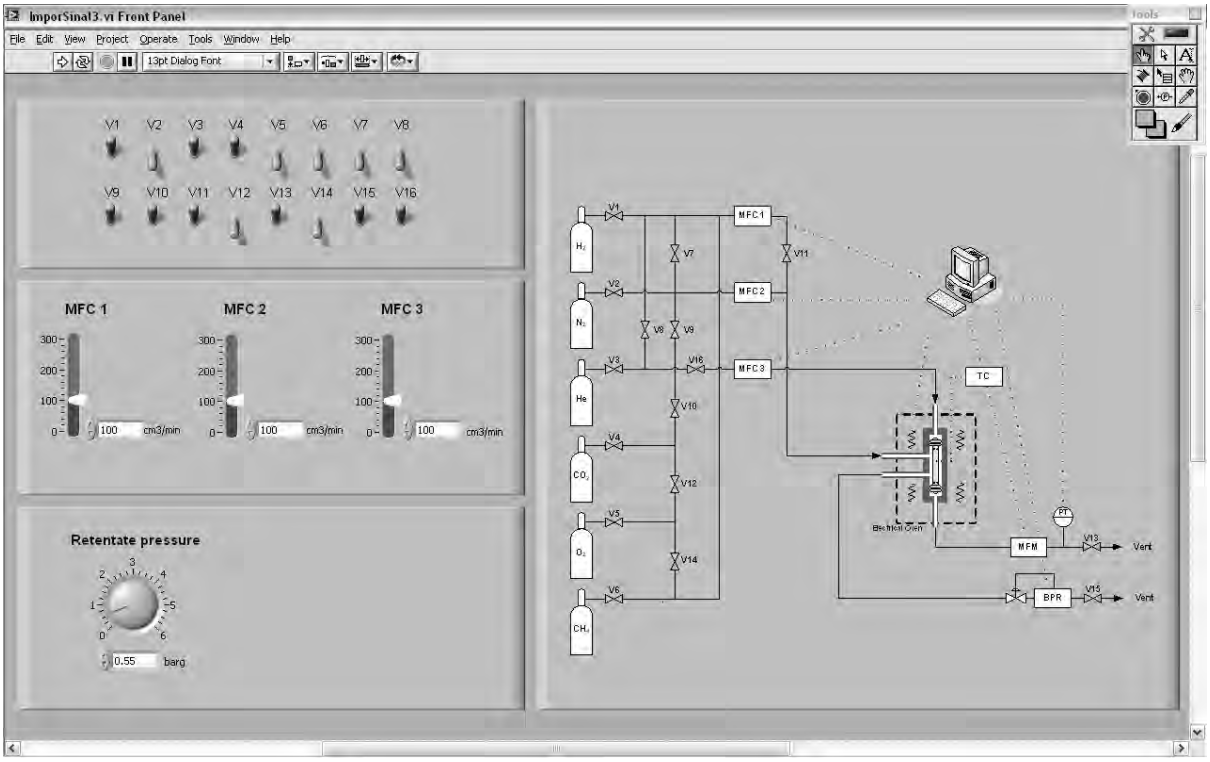

Figure V.2 - LabVIEW windows for sending information to the experimental set-up.

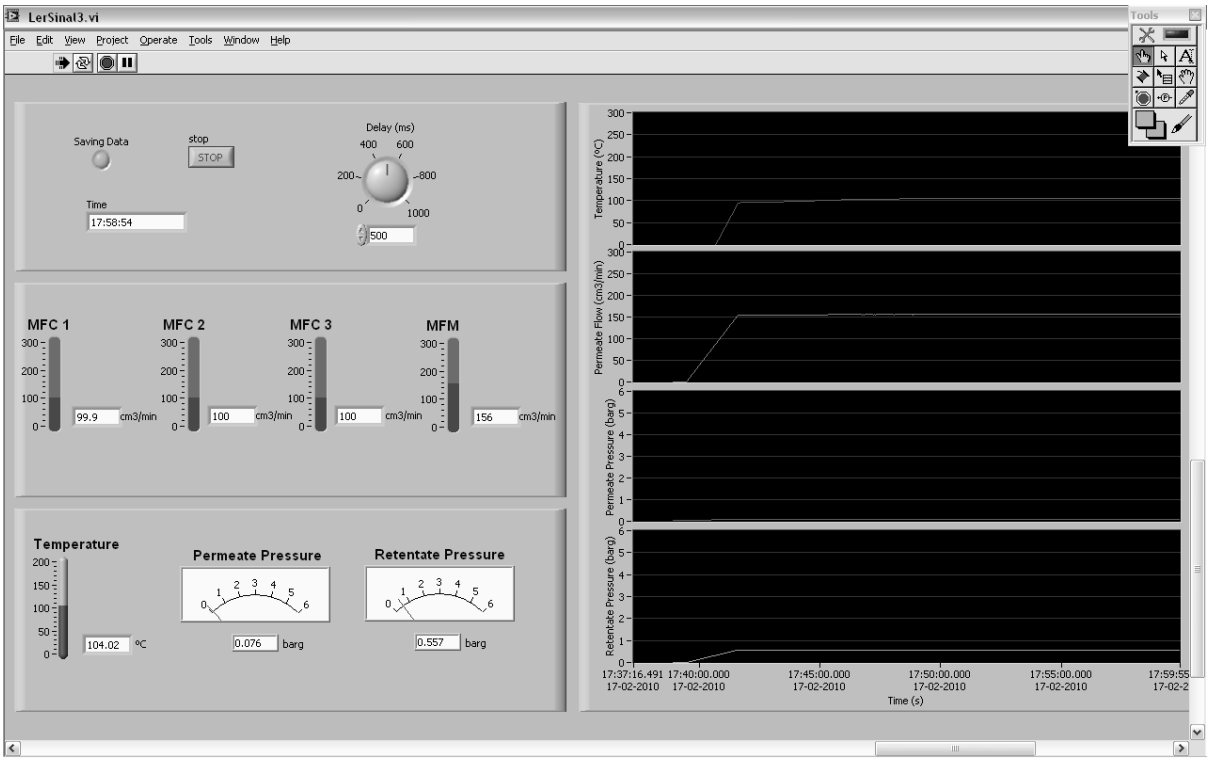

Figure V.3 – LabVIEW windows acquiring information from the experimental set-up.

With this interface, solenoid valves can be opened or closed and the feed flow (and composition in the case of binary mixtures) and retentate pressure can be regulated. The gas to be tested is selected also acting directly from PC by opening the corresponding valves (see Figure V.3). The temperature and heating rate, on the other hand, can be only adjusted on the temperature controller. Feed and permeate flow rates, retentate and permeate pressures, and temperature are continually recorded and displayed in the computer during experiments; the evolution of such parameters is also shown in a graphical form (see Figure V.3). All data measured can be collected at the end of the runs and saved into a spreadsheet file.

Calibrations

In order to control the operating conditions directly from the computer, all the measuring devices had to be previously calibrated. Concerning the mass flow controllers and mass flow meter, a distinct calibration was carried out for each gas. For that purpose, fixed flow rates were imposed directly on the MFCs display, where the studied gas was previously selected, and the corresponding voltage was registered by the LabVIEW software. This procedure was repeated for different flow rates covering all the operating range of the equipments. The MFM was calibrated after connecting the feed stream directly to the MFM, by fixing several flow rates of each gas directly on a MFC and reading the MFM voltage on the computer. The response signal of the pressure and temperature measuring devices is independent of the selected gas. Accordingly, BPR and PT calibrations were performed using only N_2. The BPR was calibrated imposing several N_2 flow rates on a MFC, and relating the pressure read on the BPR display with the voltage exhibited on the computer. A similar procedure was adopted for the PT, which was calibrated with respect to the BPR. Finally, the thermocouple was calibrated using the temperature controller as reference.

Table IV.1 compiles the calibration equations for each instrument. As an example, calibration data of the MFM for several gases are shown in Figure V.4, together with the corresponding correlation lines.

Table V.1 – Calibration data for the measuring devices.

Instrument	**Calibration Equation** [a)]
MFC 1	$Q = 59.93V - 0.53$
MFC 2	$Q = 59.98V - 0.58$
MFC 3	$Q = 109.2V - 0.03$
BPR	$P = 1.20V - 0.01$
PT	$P = 2.00V - 0.04$
TC	$T = 125.3V - 123.4$
MFM	$Q_{He} = 90.68V - 0.61$
	$Q_{H_2} = 200.78V - 1.38$
	$Q_{N_2} = 100.33V - 0.70$
	$Q_{CO_2} = 120.17V - 0.40$
	$Q_{O_2} = 87.78V - 0.26$

[a)] Q (cm^3(PTN)/min), P (barg), T (ºC), V (V)

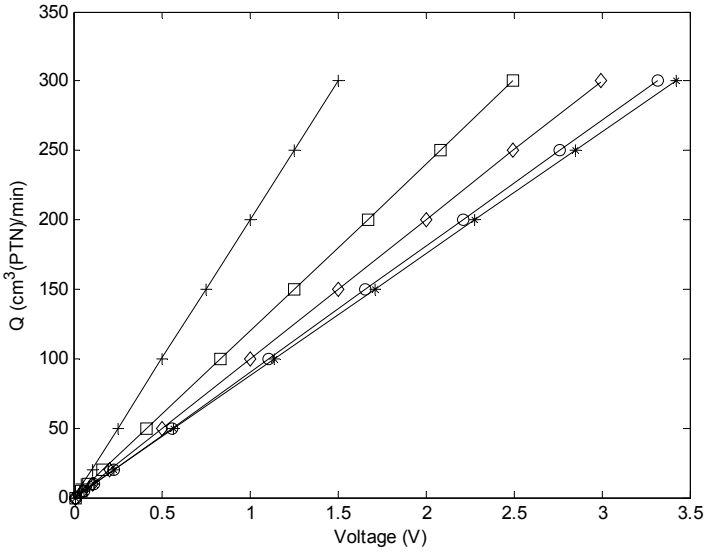

Figure V.4 – Graphical representation of calibration data of the MFM for several gases. Symbols: ○, He; +, H_2; ◊, N_2; □, CO_2; and *, O_2. Lines: fittings.

Beyond the measuring devices, also the GC system had to be calibrated in order to get the streams composition from the obtained chromatograms. For that purpose, binary and ternary mixtures with different compositions, and including all the studied gases, were analyzed. The composition of each component was then related with the corresponding area of the chromatogram peaks. The chromatograms acquisition and their mathematical treatment were carried using the DataApex Clarity software for windows.

Figure V.5 shows a chromatogram obtained for a binary CO_2/N_2 mixture, together with the resulting peak areas. A graphical representation for CO_2 calibration data is pictured in Figure V.6 as an example to illustrate the calibration procedure. As shown in this figure, the resulting calibration equation and correlation factor are simultaneously provided.

The calibrations for each gas were carried out three times in order to obtain reproducible and accurate results, which may be of special importance in the case of H_2-containing mixtures, given the similarity of H_2 and He thermal conductivities, since He was used as carrier gas for the TCD.

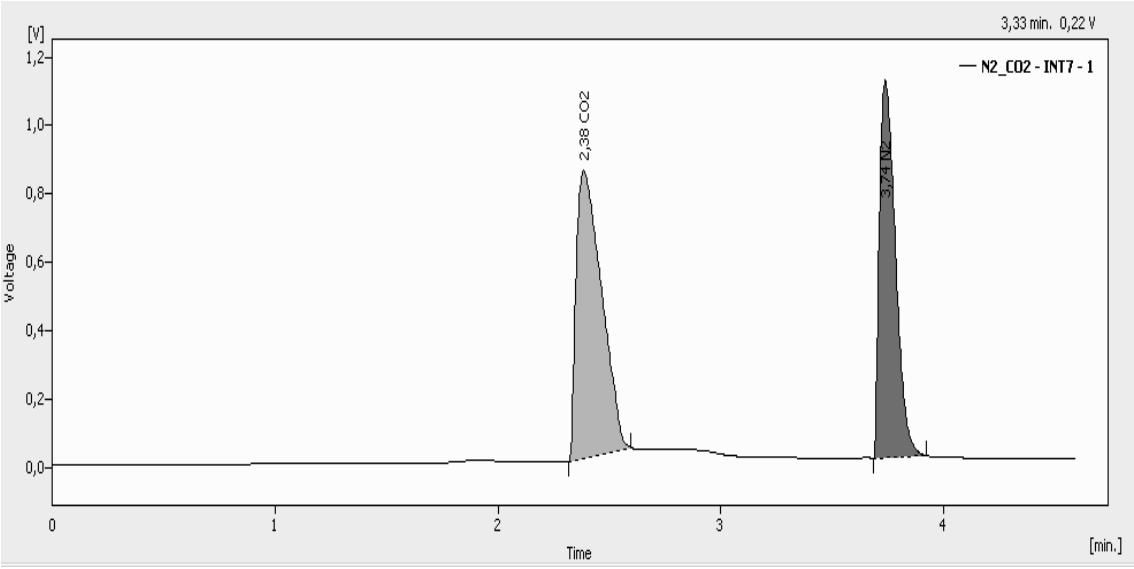

Figure V.5 – Chromatogram for a binary 50:50% CO_2/N_2 mixture.

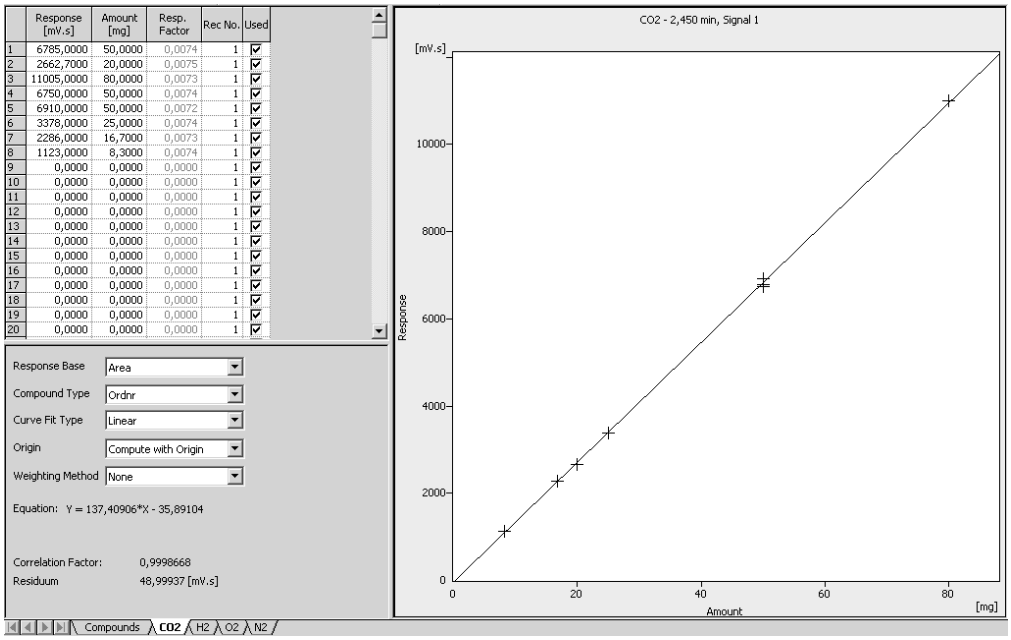

Figure V.6 – Results for the CO_2 calibration.

2. Membranes

In this work, nineteen microporous membranes were studied: nine of AM-3, and five of ETS-10. In addition, four ZSM-5 zeolite membranes and a last one of 4A- zeolite were also evaluated for comparison. All membranes were synthesized in the Associated Laboratory CICECO (Department of Chemistry, University of Aveiro) by secondary growth procedure on commercial tubular α-alumina (Inocermic) and stainless-steel (Mott Corporation) supports with different pore diameters. The α-alumina supports were symmetric with internal and external diameters of approximately 7 and 10 mm, respectively, and were 8 cm long; porous stainless-steel supports had 8 and 10 mm of internal and external diameters, respectively, and were 3.5 – 4 cm long. In order to prevent by-pass of feed and permeate streams during the permeation measurements, alumina supports were subjected to enamelling at both ends, being their permeation length reduced to approximately 5.5 cm; 2 cm long non-porous stainless-steel tubes were soldered at the end of the stainless-steel porous supports for the same purpose.

Membranes were synthesized with the crystalline layer on the outside of the tubular supports. However, a quantity of crystals could be expected to be formed inside the tubes

as well, since supports were not wrapped during membranes synthesis. Several samples were prepared varying the synthesis conditions (including time and number of synthesis).

The structure and morphology of synthesized titanosilicate membranes have been previously investigated at CICECO by X-ray diffraction, scanning electron microscopy, energy dispersive X-ray spectrometry, and X-ray mapping techniques. The main physical properties of membranes studied are compiled in Table V.2. Figure V.7 shows a stainless-steel and an α-alumina supported membranes together with a schematic representation of their structure.

Table V.2 – Characteristics of the membranes studied.

Membrane	Support	Surface area (m^2)
AM-3-1	α-alumina (3000 nm)	1.75×10^{-3}
AM-3-3	α-alumina (3000 nm)	1.72×10^{-3}
AM-3-4	α-alumina (3000 nm)	1.82×10^{-3}
AM-3-5	α-alumina (3000 nm)	1.71×10^{-3}
AM-3-7	Stainless-steel (500 nm)	1.19×10^{-3}
AM-3-8	Stainless-steel (500 nm)	1.18×10^{-3}
AM-3-9	Stainless-steel (500 nm)	1.08×10^{-3}
AM-3-10	Stainless-steel (500 nm)	1.19×10^{-3}
AM-3-11	Stainless-steel (500 nm)	1.27×10^{-3}
ETS-10-1	α-alumina (1900 nm)	1.57×10^{-3}
ETS-10-2	α-alumina (1900 nm)	1.57×10^{-3}
ETS-10-3	Stainless-steel (500 nm)	1.11×10^{-3}
ETS-10-4	Stainless-steel (500 nm)	1.14×10^{-3}
ETS-10-5	Stainless-steel (500 nm)	1.14×10^{-3}
ZSM-5-1	α-alumina (3000 nm)	1.57×10^{-3}
ZSM-5-1	Stainless-steel (500 nm)	1.14×10^{-3}
ZSM-5-2	Stainless-steel (500 nm)	1.15×10^{-3}
ZSM-5-3	Stainless-steel (500 nm)	1.14×10^{-3}
4A	Stainless-steel (500 nm)	1.12×10^{-3}

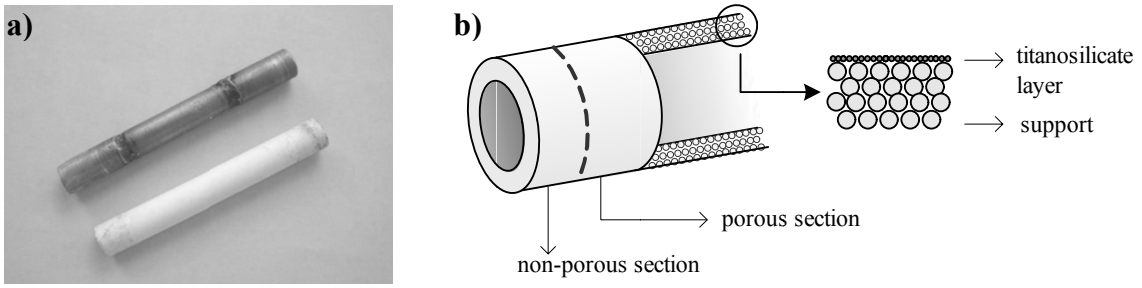

Figure V.7 – a) Stainless-steel (above) and α-alumina (below) supported membranes; b) schematic representation of membranes structure.

3. Permeation Measurements

Permeation measurements were carried out with the membrane placed inside a stainless-steel module (see a schematic representation in Figure V.8). The two entrance streams connected to the membrane module correspond to the feed and sweep gases, and module exit streams correspond to the retentate and permeate. The membrane is sealed inside the module with two o-rings in each end, in order to avoid mixture of permeate and feed streams. In the present work, the feed stream was fed to the titanosilicate side of the membrane. The feed stream tube was rolled around the membrane module to heat the gas before it faces the membrane; in this way, the temperature gradient across the membrane was minimized (please see Figure V.1d).

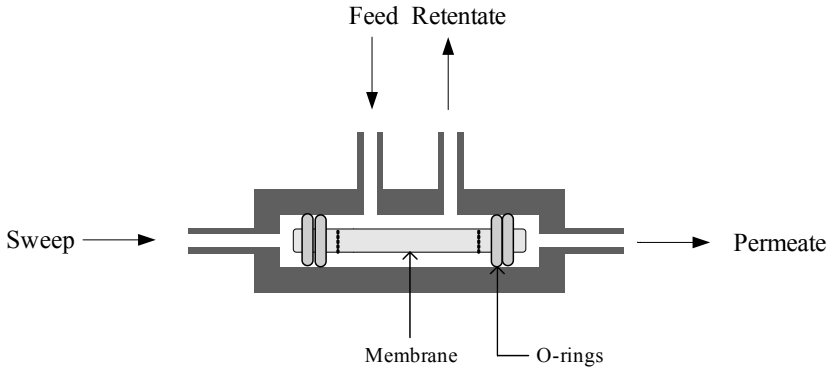

Figure V.8 – Membrane module layout.

Two methods are frequently used to create the driving force responsible for gas permeation: the pressure drop generation method and the Wicke-Kallenback (WK) method (Wicke and Kallenbach, 1941). In the first one, the driving force is created by generating a total pressure drop across the membrane, either by pressurizing the feed side or evacuating the permeate side. In the second method, a sweep gas is used (typically He or Ar) to wash the permeate chamber in order to decrease or vanish the partial pressure of the permeating species. In this case, the total pressure difference between the two sides of the membrane could be zero, eliminating the presence of viscous flow, being the partial pressure difference the driving force. Accordingly, the WK method imposes a composition gradient through the membrane by the flow of sweep gas in the permeate side. In addition, the turbulence created by the sweep gas helps desorption of adsorbed components. Both single gas permeation and mixture separation can be performed with this method. Nonetheless, sweep gas back-diffusion can occur and the new mixture, formed by permeate and sweep streams, has to be further separated for industrial purposes. This method is thus more advantageous for mixtures separation experiments, being that of the pressure difference the preferable method for single component permeation (Gump *et al.*, 2000; Bernal, 2002).

3.1 Single gas permeation

Gases

Single gas permeation experiments were performed with a transmembrane pressure drop providing the driving force, and no sweep gas was used. Nitrogen (Praxair, 99.995%), helium (Praxair, 99.999%), carbon dioxide (Praxair, 99.95%), hydrogen (Praxair, 99.995%), and oxygen (Praxair, 99.999%) were the molecules used for single gas measurements.

Membrane pre-treatment

The presence of adsorbed compounds on the titanosilicate pores affects the permeation results. ETS-10 and AM-3 crystals are hydrophilic, and therefore water molecules from moisture are expected to be adsorbed on their structure. In order to remove the adsorbed

water and eventually other compounds, a heating and cooling cycle had to be carried out up to ca. 200ºC. Single N_2 permeance was measured at room temperature before and after this thermal treatment to evaluate the effect of adsorbed compounds upon the gas permeation. The experimental procedure followed for this purpose is described under the next item. During this heating treatment, a continuous He flow (20 cm^3(PTN)/min) was kept through the membranes in order to facilitate the removal of the desorbed compounds.

Membranes were not submitted to higher temperatures due to thermal resistance limitations of the o-rings used. In fact, at the beginning of the experiments, a membrane sealed with silicone o-rings was submitted to 300ºC; however, the o-rings melted and damaged the membrane. Subsequently, a material with a higher thermal resistance, and holding at the same time sufficient flexibility, was attempted to be found; viton o-rings were selected among a few number of options (service temperature around 200ºC).

The heating and cooling cycle was repeated whenever a different gas was studied, and after changing membranes from the module (given their hydrophilic character).

Measurement of nitrogen permeance at room temperature

Dynamic characterization of new membranes should start by detecting the existence of rough defects or cracks by means of single gas permeation runs. Whenever detected, membrane preparation conditions will be adjusted until defects elimination. In this work, such characterization was accomplished by measuring permeation fluxes of pure N_2 at room temperature. The arrangement of the experimental set-up used to carry out single gas permeation measurements, at fixed temperature and under different transmembrane pressure drops, is schematically represented in Figure V.9.

The membrane was placed inside the stainless-steel module and sealed with viton o-rings. Sweep gas and retentate sides were kept blocked during the experiments (dead-end mode) to promote total permeation of the gas through the membrane. The stainless-steel module containing the membrane was placed inside the oven at fixed temperature. The flow rate of feed gas was fixed by a MFC and fed to the titanosilicate side of the membrane. The permeate side was kept at atmospheric pressure while the transmembrane

pressure drop was measured with the BPR after reaching equilibrium (stationary state). At this moment the permeate flow rate, measured by the MFM, should equal the feed gas flow rate, what was always verified.

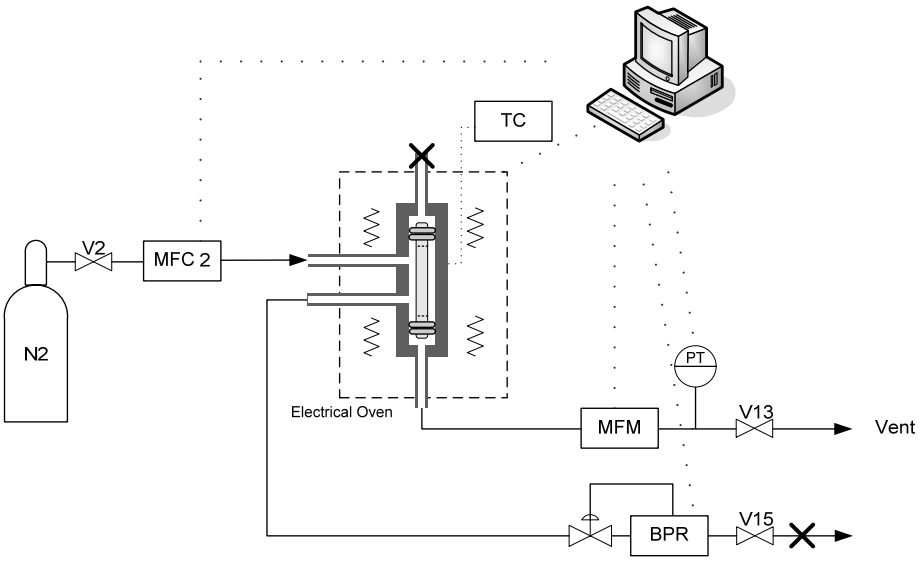

Figure V.9 – Layout of experimental apparatus for preliminary N_2 permeance tests.

During these experiments the temperature was kept at 25 ºC and different feed flow rates were imposed. Permeance was then obtained by the slope of the permeation flux *versus* transmembrane pressure difference curve (see equation (II.3)).

Permeation of single gases at programmed temperature (PPT)

A different test used to evaluate the membrane structure consists in the measurement of permeation fluxes of single gases at programmed temperature, with a fixed transmembrane pressure drop. From permeation *versus* temperature curves it is possible to characterize the transport mechanisms taking place at a given temperature and, subsequently, to detect defects in the crystalline structure of the membrane. The PPT experiments were reported for the first time by Bernal *et al.* (2002), being presented as a fast and reliable tool to investigate the characteristics of zeolite membranes.

Figure V.10 shows the experimental set-up used to carry out PPT measurements. Gases with different molecular weights and diameters were studied, namely: N_2, H_2, He, CO_2 and O_2.

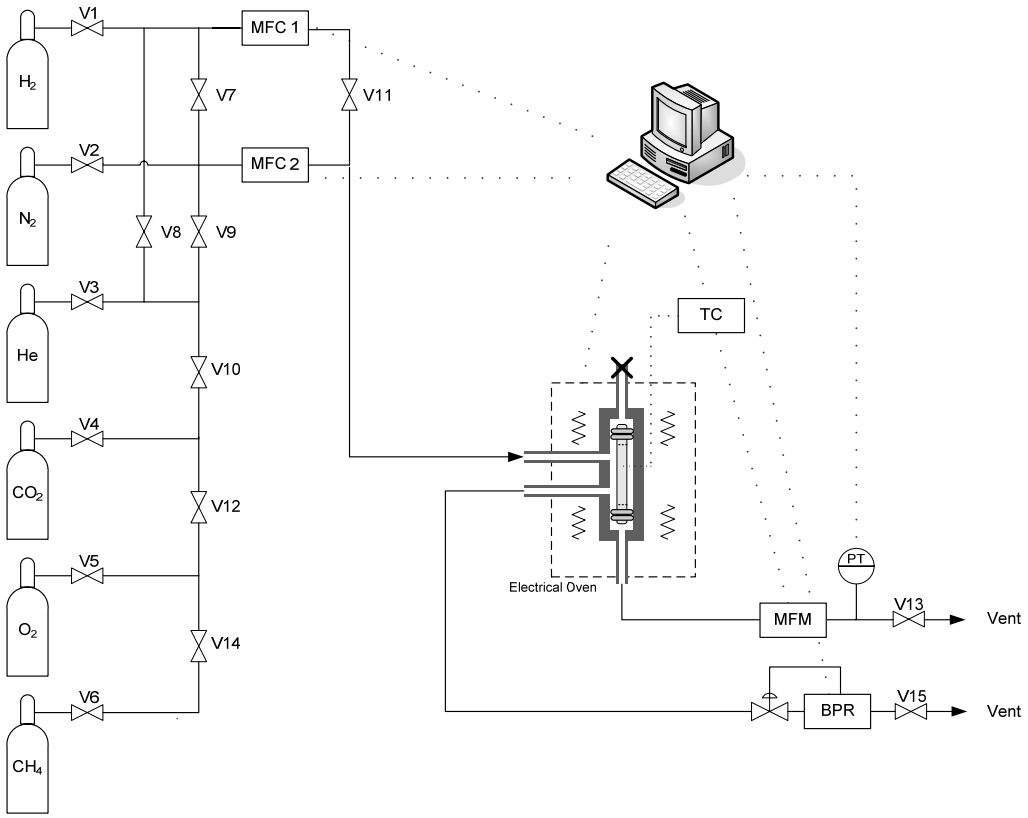

Figure V.10 - Layout of experimental apparatus for permeation at programmed temperature of single gases.

The feed gas stream, regulated by a MFC, was fed to the membrane module placed inside the oven, and a temperature ramp was programmed with a fixed heating rate of 1 ºC/min. This value is generally sufficient to approach stationary state at each temperature, but not excessively small to delay the experiments; moreover, it is the smaller heating rate allowed by the temperature controller. The permeate side was kept at atmospheric pressure, while transmembrane pressure difference was controlled by the BPR. During these experiments the retentate side was no longer blocked. The values of the permeate flow measured by the MFM and temperature by the thermocouple were continually registered

along time by the data acquisition system. Experiments were conducted with different feed flows in the temperature range of 25 to 180ºC, for fixed transmembrane pressure drops between 20 and 500 kPa. Permeances were obtained by the ratio of permeation fluxes and transmembrane pressure difference (see equation (II.3)).

Measurement of single gas permeances at fixed temperatures

After discriminating the transport mechanisms, membranes with the desired microporous structure are distinguished. Some permeation fluxes of defect-free membranes of pure N_2, H_2, He, O_2, and CO_2 at fixed temperatures were measured for different transmembrane pressure drops to determine their permeances and corresponding ideal selectivities. The experimental procedure adopted was similar to that for measurement of pure N_2 permeance at room temperature. However, the results obtained overlapped those from PPT experiments, and thus have been canceled.

3.2 Mixture separation

Even though single gas permeation and ideal selectivities are fundamental to evaluate membranes quality, its primary aim is the separation of mixtures. In this work, the capability of membranes to perform real separations was examined. Some binary mixtures were studied at different temperatures. The separation factors obtained were determined and compared with those of single gases.

In order to quantify the separation of binary mixtures, an on-line gas chromatograph (GC) was included on the experimental set-up to analyze the streams composition. The arrangement of the experimental apparatus used to perform binary mixture separations is schematically represented in Figure V.11.

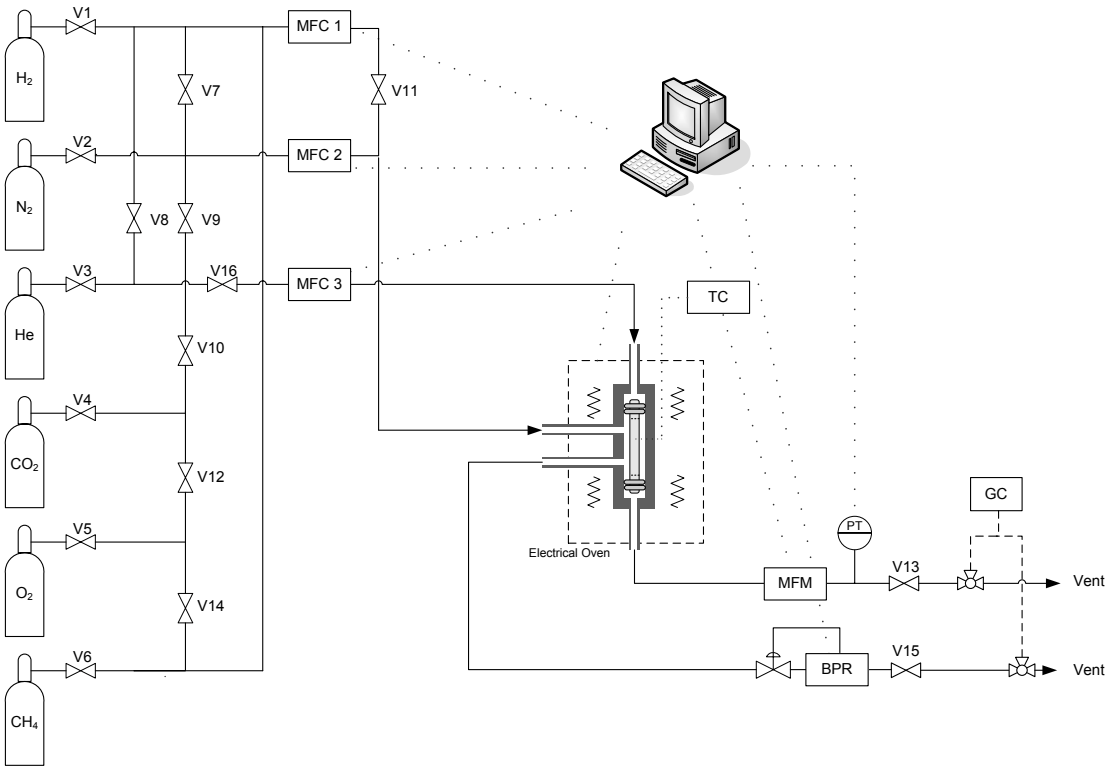

Figure V.11 – Layout of experimental apparatus for mixtures separation.

Similarly to single gas permeation experiments, the membrane was hold inside the module, with both ends sealed with viton o-rings, and placed inside the oven to keep the operation temperature at the desired value. The feed mixture was generated by mixing two pure component streams whose individual flow rates were regulated by two MFC's. The retentate side was opened to carry out the separation. Both feed and permeate sides were kept at atmospheric pressure while a sweep gas was used to increase the driving force; the permeate partial pressure was manipulated by varying the sweep gas flow rate via the third MFC.

After matching the stationary state, feed, retentate and permeate streams were analyzed by the GC. Two manual three-way valves placed on the permeate and retentate lines allow one to select the streams direction, i.e., toward the atmosphere or toward the GC. A two-position microvolume sample injection valve (VICI) permits the injection of a fixed gas volume to the GC columns. In the load position, the selected stream flows continually through the sample loop into the atmosphere, while the mobile phase (He) flows through to the column. In the injection position, the loop is in line with the column

and the mobile phase injects the content of the loop onto the first column (VP Hayesep D), where the CO_2, whenever present, is retained. The CO_2-free stream is subsequently fed to the second column (VP Molesieve), where the remaining permanent gases are separated. At this moment, a second two-position valve (VICI) is automatically actuated allowing CO_2 to by-pass the second column. The separated components flow then to the TCD, where the mixture composition is determined. Each analysis was carried out three times.

The permeance of each component and the corresponding separation factors were calculated by equations (II.2) and (II.4), respectively.

VI. Results and Discussion

This chapter presents all experimental and modelling results obtained in this work. Concerning modelling, new expressions for Maxwell-Stefan thermodynamic factors were derived for pure and multicomponent Nitta, Langmuir-Freundlich, and Toth isotherms. Up till now, only relations for Langmuir and dual-site Langmuir have been published, what is a strong limitation since many adsorption systems exhibit distinct behaviours. As it will be shown it is possible to predict the permeation of binary mixtures through zeolite membranes, when equilibrium and diffusivities are known for pure gases.

With respect to experimental results, the dynamic characterization of the microporous membranes is presented, namely: the permeation of single gases and binary mixtures in AM-3, ETS-10, ZSM-5, and zeolite 4A membranes, at fixed and programmed temperature and for several transmembrane pressure drops. Modelling results based on the transport mechanisms described in Chapter III under the framework of the Maxwell-Stefan approach are also presented.

1. New expressions for surface diffusion

New Maxwell-Stefan (MS) thermodynamic factors. The use of different adsorption isotherms gives rise to different thermodynamic correction factors (Krishna and Wesselingh, 1997). When the MS equations are used to describe the permeation of gas mixtures through zeolite membranes, the multicomponent Langmuir isotherm is commonly

adopted by researchers, as firstly presented by Krishna (1990,1993). More recently, thermodynamic correction factors for the dual-site Langmuir model have been also considered (Krishna and Baur, 2003). However, it is clear from the literature that these two isotherms are not always the most appropriate to describe adsorption in zeolites. Therefore, in this work, new expressions for the thermodynamic factors have been developed and tested, specifically for the pure and multicomponent isotherms of Nitta, Langmuir-Freundlich, and Toth, since they are frequently applicable to represent equilibrium in zeolites as well as in the design of several engineering applications. The results obtained have been compared with those provided by the Langmuir model. The new derived expressions are listed in Table VI.1 - equations (VI.1) to VI.7) – whereas the Langmuir equations are given in Chapter III - equations (III.18) and (III.45).

Table VI.1 – Thermodynamic factors derived in this work for single-component and binary mixtures for different isotherms.

Langmuir-Freundlich	
Single-component	
$\Gamma = \frac{n_{\mathrm{LF}}}{1-\theta}$	(VI.1)
Binary mixture	
$\Gamma_{11} = \frac{\theta_2 - 1}{(1/n_{\mathrm{LF},1})(\theta_1 + \theta_2 - 1)}$ $\quad$ $\Gamma_{21} = -\frac{\theta_2}{(1/n_{\mathrm{LF},2})(\theta_1 + \theta_2 - 1)}$ $\Gamma_{22} = \frac{\theta_1 - 1}{(1/n_{\mathrm{LF},2})(\theta_1 + \theta_2 - 1)}$ $\quad$ $\Gamma_{12} = -\frac{\theta_1}{(1/n_{\mathrm{LF},1})(\theta_1 + \theta_2 - 1)}$	(VI.2)
Nitta	
Single-component	
$\Gamma = \frac{1-\theta(1-n_{\mathrm{N}})}{1-\theta}$	(VI.3)
Binary mixture	
$\Gamma_{11} = \frac{\theta_1(1-n_{\mathrm{N},1}) + \theta_2 - 1}{\theta_1 + \theta_2 - 1}$ $\quad$ $\Gamma_{12} = -\frac{\theta_1 n_{\mathrm{N},1}}{\theta_1 + \theta_2 - 1}$	(VI.4)

$$\Gamma_{22} = \frac{\theta_2\left(1-n_{\mathrm{N},2}\right)+\theta_1-1}{\theta_1+\theta_2-1} \qquad \Gamma_{21} = -\frac{\theta_2 n_{\mathrm{N},2}}{\theta_1+\theta_2-1}$$

Toth

Single-component

$$\Gamma = \frac{\theta^{-\mathrm{t}}}{\theta^{-\mathrm{t}}-1} \tag{VI.5}$$

Binary mixture

$$\Gamma_{11} = \frac{t_2\left[-1-2\left(b_1p_1\right)^{t_1}-\left(b_2p_2\right)^{t_2}-\left(b_1p_1\right)^{2t_1}-\left(b_1p_1\right)^{t_1}\left(b_2p_2\right)^{t_2}\right]}{\Omega\left[-t_2\left(b_1p_1\right)^{t_1}+\left(b_1p_1\right)^{t_1}t_1-t_2\right]} \tag{VI.6}$$

$$\Gamma_{12} = b_1p_1\,\Omega^{\frac{2+t_2}{t_2}}t_2^2\left(b_2p_2\right)^{t_2}\Bigg/\Bigg[p_2b_2\Bigg(\Omega^{\frac{-2(1+t_2)}{t_2}}t_2^2+2\Omega^{\frac{-2(1+t_2)}{t_2}}t_2^2\left(b_1p_1\right)^{t_1}+\Omega^{\frac{-2(1+t_2)}{t_2}}t_2^2\left(b_2p_2\right)^{t_2}+$$
$$\Omega^{\frac{-2(1+t_2)}{t_2}}t_2^2\left(b_1p_1\right)^{2t_1}+\Omega^{\frac{-2(1+t_2)}{t_2}}t_2^2\left(b_1p_1\right)^{t_1}\left(b_2p_2\right)^{t_2}-\Omega^{\frac{-2(1+t_2)}{t_2}}\left(b_1p_1\right)^{t_1}t_1t_2-\Omega^{\frac{-2(1+t_2)}{t_2}}\left(b_1p_1\right)^{2t_1}t_1t_2-$$
$$\Omega^{\frac{-2(1+2t_2)}{t_2}}\left(b_2p_2\right)^{t_2}t_2\left(b_1p_1\right)^{t_1}t_1-2\Omega^{\frac{-2(1+2t_2)}{t_2}}\left(b_2p_2\right)^{t_2}t_2\left(b_1p_1\right)^{2t_1}t_1-2\Omega^{\frac{-2(1+2t_2)}{t_2}}\left(b_2p_2\right)^{2t_2}t_2\left(b_1p_1\right)^{t_1}t_1-$$
$$\Omega^{\frac{-2(1+2t_2)}{t_2}}\left(b_2p_2\right)^{t_2}t_2\left(b_1p_1\right)^{3t_1}t_1-2\Omega^{\frac{-2(1+2t_2)}{t_2}}\left(b_2p_2\right)^{2t_2}t_2\left(b_1p_1\right)^{2t_1}t_1-\Omega^{\frac{-2(1+2t_2)}{t_2}}\left(b_2p_2\right)^{3t_2}t_2\left(b_1p_1\right)^{t_1}t_1\Bigg)\Bigg]$$

$$\Gamma_{21} = b_2p_2\,\Omega^{\frac{2+t_2}{t_2}}t_2\left(b_1p_1\right)^{t_1}t_1\Bigg/\Bigg[p_1b_1\Bigg(\Omega^{\frac{-2(1+t_2)}{t_2}}t_2^2+2\Omega^{\frac{-2(1+t_2)}{t_2}}t_2^2\left(b_1p_1\right)^{t_1}+\Omega^{\frac{-2(1+t_2)}{t_2}}t_2^2\left(b_2p_2\right)^{t_2}+$$
$$\Omega^{\frac{-2(1+t_2)}{t_2}}t_2^2\left(b_1p_1\right)^{2t_1}+\Omega^{\frac{-2(1+t_2)}{t_2}}t_2^2\left(b_1p_1\right)^{t_1}\left(b_2p_2\right)^{t_2}-\Omega^{\frac{-2(1+t_2)}{t_2}}\left(b_1p_1\right)^{t_1}t_1t_2-\Omega^{\frac{-2(1+t_2)}{t_2}}\left(b_1p_1\right)^{2t_1}t_1t_2-$$
$$\Omega^{\frac{-2(1+2t_2)}{t_2}}\left(b_2p_2\right)^{t_2}t_2\left(b_1p_1\right)^{t_1}t_1-2\Omega^{\frac{-2(1+2t_2)}{t_2}}\left(b_2p_2\right)^{t_2}t_2\left(b_1p_1\right)^{2t_1}t_1-2\Omega^{\frac{-2(1+2t_2)}{t_2}}\left(b_2p_2\right)^{2t_2}t_2\left(b_1p_1\right)^{t_1}t_1-$$
$$\Omega^{\frac{-2(1+2t_2)}{t_2}}\left(b_2p_2\right)^{t_2}t_2\left(b_1p_1\right)^{3t_1}t_1-2\Omega^{\frac{-2(1+2t_2)}{t_2}}\left(b_2p_2\right)^{2t_2}t_2\left(b_1p_1\right)^{2t_1}t_1-\Omega^{\frac{-2(1+2t_2)}{t_2}}\left(b_2p_2\right)^{3t_2}t_2\left(b_1p_1\right)^{t_1}t_1\Bigg)\Bigg]$$

$$\Gamma_{22} = \Big[-t_2-2t_2\left(b_1p_1\right)^{t_1}-2\left(b_2p_2\right)^{t_2}t_2-t_2\left(b_1p_1\right)^{2t_1}-2\left(b_1p_1\right)^{t_1}\left(b_2p_2\right)^{t_2}t_2-t_2\left(b_2p_2\right)^{2t_2}+$$
$$\left(b_1p_1\right)^{t_1}t_1+t_1\left(b_1p_1\right)^{2t_1}+\left(b_1p_1\right)^{t_1}t_1\left(b_2p_2\right)^{t_2}\Big]/\left[\Omega\left(-t_2\left(b_1p_1\right)^{t_1}+\left(b_1p_1\right)^{t_1}t_1-t_2\right)\right]$$

$$\Omega = 1+\left(b_1p_1\right)^{t_1}+\left(b_2p_2\right)^{t_2} \tag{VI.7}$$

The calculation of the thermodynamic correction factors require differentiation of the isotherms explicitly written in terms of fugacity or partial pressure (equation (III.43)). While Nitta multicomponent isotherm (equation (III.52)) is given directly in terms of partial pressure, and the multicomponent Langmuir and Langmuir-Freundlich isotherms (equations (III.44) and (III.58)) are easily inverted, the multicomponent Toth isotherm (equations (III.61) - (III.63)) is not so straightforward because of the complexity introduced by exponent t. In order to overcome such limitation, the isotherm equation in fractional loading-form was differentiated with respect to the partial pressures and the inverse functions obtained following calculus relations. Hence, taking into account that $\theta_i = \theta_i(p_i, p_j)$ and $\theta_j = \theta_j(p_i, p_j)$, the following system of differential equations is obtained:

$$\begin{cases} d\theta_1 = \left(\dfrac{\partial\theta_1}{\partial p_1}\dfrac{\partial p_1}{\partial\theta_1} + \dfrac{\partial\theta_1}{\partial p_2}\dfrac{\partial p_2}{\partial\theta_1}\right)d\theta_1 + \left(\dfrac{\partial\theta_1}{\partial p_1}\dfrac{\partial p_1}{\partial\theta_2} + \dfrac{\partial\theta_1}{\partial p_2}\dfrac{\partial p_2}{\partial\theta_2}\right)d\theta_2 \\ d\theta_2 = \left(\dfrac{\partial\theta_2}{\partial p_1}\dfrac{\partial p_1}{\partial\theta_1} + \dfrac{\partial\theta_2}{\partial p_2}\dfrac{\partial p_2}{\partial\theta_1}\right)d\theta_1 + \left(\dfrac{\partial\theta_2}{\partial p_1}\dfrac{\partial p_1}{\partial\theta_2} + \dfrac{\partial\theta_2}{\partial p_2}\dfrac{\partial p_2}{\partial\theta_2}\right)d\theta_2 \end{cases} \tag{VI.8}$$

and solved using Cramer's rule to get the desired inverse partial derivatives:

$$\begin{aligned} \left(\frac{\partial p_1}{\partial\theta_2}\right)_{\theta_1} &= -\left(\frac{\partial\theta_1}{\partial p_2}\right)_{p_1} \Big/ D \\ \left(\frac{\partial p_2}{\partial\theta_2}\right)_{\theta_1} &= \left(\frac{\partial\theta_1}{\partial p_1}\right)_{p_2} \Big/ D \\ \left(\frac{\partial p_1}{\partial\theta_1}\right)_{\theta_2} &= \left(\frac{\partial\theta_2}{\partial p_2}\right)_{p_1} \Big/ D \\ \left(\frac{\partial p_2}{\partial\theta_1}\right)_{\theta_2} &= -\left(\frac{\partial\theta_2}{\partial p_1}\right)_{p_2} \Big/ D \end{aligned} \tag{VI.9}$$

where

$$D \equiv \left(\frac{\partial\theta_1}{\partial p_1}\right)_{p_2}\left(\frac{\partial\theta_2}{\partial p_2}\right)_{p_1} - \left(\frac{\partial\theta_1}{\partial p_2}\right)_{p_1}\left(\frac{\partial\theta_2}{\partial p_1}\right)_{p_2} \quad . \tag{VI.10}$$

Pure and multicomponent isotherms for methane/ethane/silicalite-1 systems. The validity of the new equations proposed in Table VI.1 was assessed using experimental data taken from literature for the separation of ethane/methane mixtures with a silicalite-1 membrane (van de Graaf *et al.*, 1999). The isotherms for both methane/silicalite-1 and ethane/silicalite-1 systems were obtained by fitting data reported by Zhu *et al.*, (1998) whose values are listed in Tables VI.2 and VI.3 for 303, 338, and 373 K.

Table VI.2 - Single component adsorption data for methane in silicalite-1 at 303, 338, and 373 K (from Zhu *et al.* (1998)).

303 K		338 K		373 K	
P (10^5 Pa)	q (mol/kg)	P (10^5 Pa)	q (mol/kg)	P (10^5 Pa)	q (mol/kg)
0.104	0.045	0.097	0.026	0.306	0.037
0.142	0.065	0.127	0.035	0.415	0.050
0.172	0.078	0.171	0.041	0.495	0.060
0.200	0.088	0.206	0.047	0.564	0.067
0.254	0.116	0.262	0.058	0.665	0.080
0.294	0.136	0.310	0.072	0.737	0.089
0.393	0.180	0.405	0.093	0.820	0.098
0.477	0.214	0.490	0.108	0.902	0.105
0.547	0.243	0.552	0.121	1.011	0.117
0.641	0.280	0.655	0.145	1.102	0.129
0.707	0.304	0.720	0.156	1.504	0.171
0.789	0.335	0.800	0.174	1.998	0.221
0.829	0.354	0.883	0.187	2.498	0.266
0.876	0.371	0.986	0.207	2.997	0.309
0.918	0.386	1.104	0.230	3.503	0.349
0.980	0.406	1.501	0.297	4.003	0.388
1.092	0.445	1.999	0.380	4.502	0.424
1.490	0.569	2.498	0.452	5.002	0.457
2.000	0.685	2.998	0.517		
2.500	0.800	3.498	0.580		
2.999	0.898	4.003	0.634		
3.505	0.981	4.503	0.684		
4.017	1.056	5.003	0.731		
4.505	1.121				
5.004	1.175				

Table VI.3 – Single component adsorption data for ethane in silicalite-1 at 303, 338, and 373 K (from Zhu *et al.* (1998)).

303 K		338 K		373 K	
P (10^5 Pa)	q (mol/kg)	P (10^5 Pa)	q (mol/kg)	P (10^5 Pa)	q (mol/kg)
0.033	0.220	0.051	0.147	0.023	0.038
0.054	0.405	0.079	0.208	0.054	0.064
0.086	0.548	0.102	0.255	0.085	0.088
0.106	0.666	0.122	0.296	0.101	0.111
0.134	0.768	0.149	0.346	0.120	0.129
0.154	0.839	0.188	0.422	0.143	0.146
0.193	0.953	0.227	0.480	0.193	0.187
0.233	1.041	0.305	0.597	0.224	0.219
0.318	1.172	0.371	0.688	0.313	0.280
0.388	1.254	0.444	0.758	0.387	0.332
0.450	1.318	0.549	0.848	0.452	0.379
0.558	1.385	0.618	0.906	0.552	0.443
0.631	1.429	0.726	0.962	0.626	0.484
0.724	1.469	0.826	1.023	0.726	0.536
0.827	1.507	0.965	1.083	0.830	0.582
0.973	1.553	1.108	1.159	0.972	0.646
1.109	1.592	1.502	1.275	1.101	0.707
1.508	1.652	2.003	1.366	1.501	0.836
2.004	1.696	2.511	1.430	2.002	0.958
2.506	1.720	3.006	1.478	2.498	1.046
3.007	1.740	3.508	1.515	3.000	1.117
3.509	1.753	4.009	1.548	3.501	1.174
4.010	1.766			4.009	1.225

In Table VI.4, the parameters for Langmuir, Nitta, Langmuir-Freundlich, and Toth isotherms are listed together with the corresponding absolute average relative deviations found $(AARD)$. It is worth noting that our optimization involved simultaneously the experimental data for the three temperatures available, by taking into account the relations of Chapter III for the temperature dependence of the intrinsic parameters, i.e. equations (III.17), (III.50), (III.55), (III.56), (III.57) and (III.60). The reference temperature was set $T_o = 303$ K. This approach was adopted in order to reduce the number of parameters and to allow the estimation of equilibrium at different temperatures. In the particular case of the Langmuir and Nitta models, the saturation loadings are usually set constant (e.g., Do (1998)), although some authors consider their variation too (e.g., van de Graaf *et al.,*

(1999)). In this work, the q_{sat} temperature dependence was assumed to be similar to those of the Langmuir-Freundlich and Toth equations ((III.57); the parameter n_N of the Nitta isotherm was the unique considered $T-$independent; for the multicomponent Toth expression, an approach similar to that of Lamia *et al.* (2009) was adopted while taking $t_T = t_{ethane}$.

It is clear from the small *AARDs* obtained (1.67 – 2.98%) that all equations are able to represent equilibrium data with similar and high accuracies within the ranges of temperature and pressure studied. For the reference temperature, Langmuir-Freundlich and Toth isotherms are found to practically reduce to the Langmuir model, especially for ethane, as the corresponding heterogeneity parameters are nearly unity (see equations (III.54)and (III.59)). Similar results were obtained by Abdul-Rehman *et al.* (1990) and Buss and Heuchel (1997), which were attributed to the high surface homogeneity as well as the channel-like pore geometry of silicalite-1, where interactions between adsorbate molecules can only occur to a small extent.

The fitted Q for each adsorption isotherm are analogous, namely 10.797–14.697 kJ/mol for methane and 26.552–28.323 kJ/mol for ethane, although they do not have to be necessarily identical, since for Langmuir Q_L is the isosteric heat of adsorption, while for the other isotherms it is only a measure of the adsorption heat.

Concerning the multicomponent equilibrium for the methane/ethane/silicalite-1 system, it has been estimated in this work from the pure gas isotherms. Accordingly, the parameters from Table VI.4 have been directly substituted in equations (III.44), (III.52), (III.58), and (III.63) to get Langmuir, Nitta, Langmuir-Freundlich, and Toth models, respectively. In Figure VI.1 the equilibrium predictions at 303 K are shown. In the calculations the saturation capacity of each component in the binary mixture was fixed equal to that of ethane for thermodynamic consistency, following the van de Graaf *et al.*'s approach (van de Graaf *et al.*, 1999).

Table VI.4 – Single-component isotherm parameters.

				Langmuir			**(eq. III.16)**
	b_o (Pa^{-1})	Q_L (kJ/mol)		$q_{sat,o}$ (mol/kg)	χ_L		*AARD* (%)
CH_4	2.218×10^{-6}	14.697		2.243	1.221		1.67
C_2H_6	5.256×10^{-5}	28.323		1.857	0.378		1.94
				Langmuir-Freundlich			**(eq. III.54)**
	b_o (Pa^{-1})	Q_{LF} (kJ/mol)	$1/n_o$	α_{LF}	$q_{sat,o}$ (mol/kg)	χ_{LF}	*AARD* (%)
CH_4	2.855×10^{-6}	11.401	1.057	7.543×10^{-17}	1.969	2.119	1.79
C_2H_6	5.463×10^{-5}	26.542	1.047	2.756×10^{-15}	1.832	0.633	2.57
				Nitta			**(eq. III.51)**
	n	b_o (K.Pa^{-1})		Q_N (kJ/mol)	$q_{sat,o}$ (mol/kg)	χ_N	*AARD* (%)
CH_4	0.638	4.446×10^{-6}		13.097	1.720	1.663	1.90
C_2H_6	0.939	5.552×10^{-5}		27.872	1.832	0.438	2.98
				Toth			**(eq. III.59)**
	b_o (Pa^{-1})	Q_T (kJ/mol)	t_o	α_T	$q_{sat,o}$ (mol/kg)	χ_T	*AARD* (%)
CH_4	2.832×10^{-6}	10.797	1.386	3.135×10^{-17}	1.637	2.291	1.72
C_2H_6	5.050×10^{-5}	27.236	1.061	2.396×10^{-16}	1.831	0.535	2.04

According to Figure VI.1a, the predicted methane concentration in silicalite-1 decreases considerably as ethane pressure increases. This is due to competition effects, i.e., since ethane is preferentially adsorbed, the amount of available sites for methane adsorption is reduced and consequently its surface concentration decreases. In contrast, the same behaviour was not observed for ethane (Figure VI.1b), once the presence of methane in the binary mixture does not significantly influence its adsorption equilibrium. It is also evident from Figure VI.1 that all predicted binary isotherms exhibit a similar trend. However, for methane some deviations result from the different equations. For instance, Nitta predicts higher concentration values in the solid, while Langmuir provides the smaller ones. For ethane adsorption, the extended Nitta equation predicts slightly higher loadings while the remaining three perform similarly.

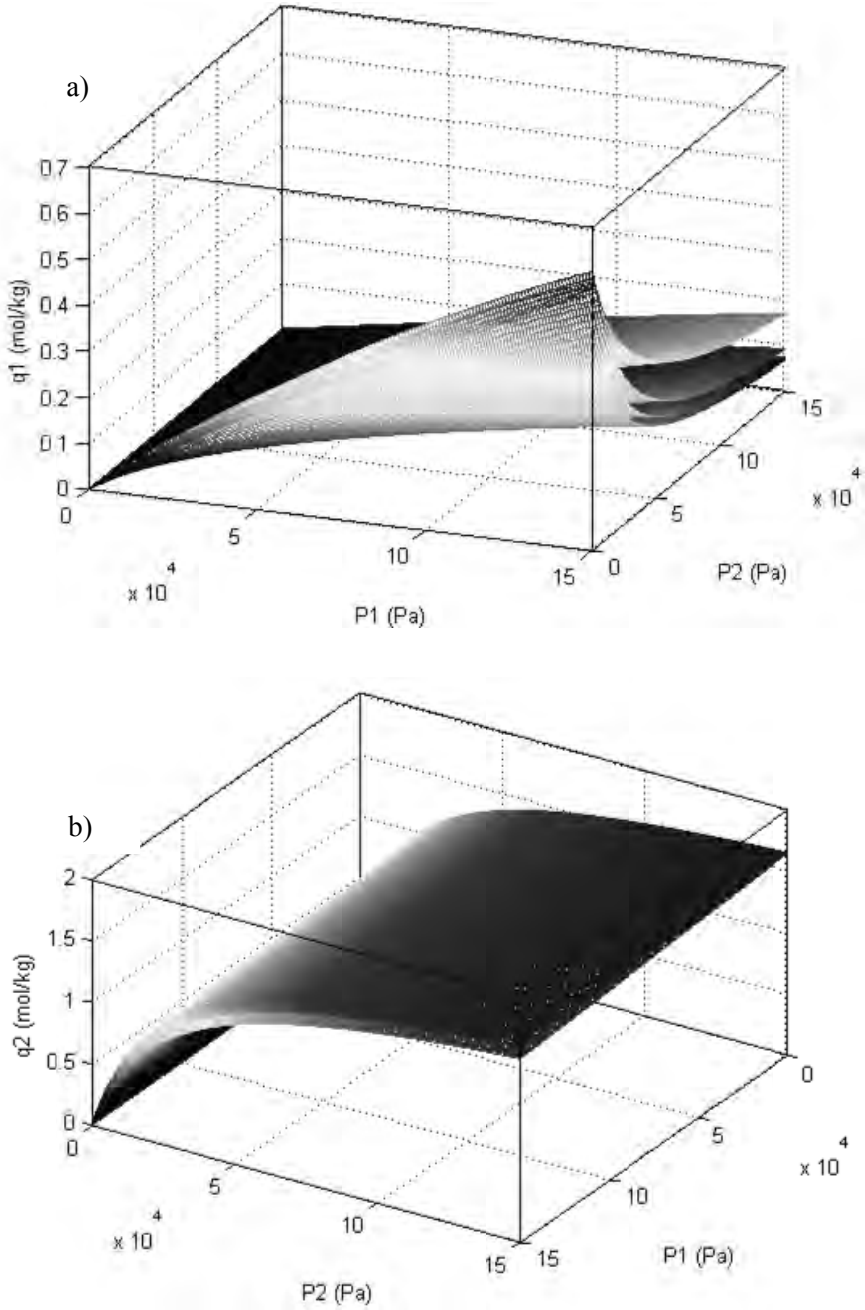

Figure VI.1 – Prediction of binary methane(1)/ethane(2) adsorption equilibrium at 101.3 kPa for (a) methane and (b) ethane, using different isotherm models: Nitta, Toth, Langmuir-Freundlich, and Langmuir isotherms (from upper to lower curves, respectively).

Determination of single MS diffusivities of methane and ethane in a silicalite-1 membrane. In order to predict the separation of methane/ethane mixtures on a silicalite-1 membrane, the individual gas permeations were firstly studied in this work taking into

account the experimental data published by van de Graaf *et al.* (1999), specifically pure gas fluxes for several transmembrane pressure drops at 303 and 373 K. The physical features of the membrane zeolite and support layers are compiled in Table VI.5.

Table VI.5 – Zeolite and support layers parameters.

Surface membrane area, m^2	2.0×10^{-4}
Zeolite layer thickness, m	10×10^{-6}
Zeolite density, g m^{-3}	1.8×10^{6}
Support thickness, m	3.0×10^{-3}
Support porosity	0.2

The single component diffusion parameters of equation (III.15) are $Đ_o^s$ and $E_{a,s}$. These were optimized for each isotherm by substituting the corresponding thermodynamic factors, Γ, given in Table VI.1. Such fittings were carried out by solving simultaneously the MS equations for the zeolite and support layers, in order to determine their corresponding profiles of θ and pressure. The isotherm equations were used to calculate the compositions in the feed/zeolite and zeolite/support interfaces.

The calculated results are graphed in Figure VI.2 as flux *versus* pressure, for both temperatures studied, and the regressed parameters are compiled in Table VI.6. Figure VI.2 shows an approximately linear dependence of methane permeation fluxes on pressure, while ethane fluxes tend to a maximum (monolayer capacity) at 303 K, due to its stronger adsorption strength on the zeolite. All isotherms analysed are able to anticipate this saturation limit for sufficiently high pressures. Accordingly, a good fit was found for ethane using all of them. On the other hand, only Langmuir and Toth predict the expected Henry's law limit at low pressures. Nonetheless, all isotherms describe accurately the methane linear trend, since Nitta and Langmuir-Freundlich almost reduce to the Langmuir model (remember that n_{LF} and t are nearly unity). It may be also observed that at higher temperatures (Figure VI.2b, 373 K) the permeation of methane decreases, while that of ethane increases. Such behaviour inclusively makes methane permeation inferior to ethane.

Besides, ethane fluxes approach the linear limit, in comparison to 303 K, since its adsorption strength decreases with temperature. As previously discussed in Chapter III, the permeation flux of adsorbable molecules may show a typical maximum with temperature, due to the opposing effects that temperature imparts upon diffusivity and adsorption. Moreover, a temperature shift of the maximum may be observed for molecules with increasing adsorption strength, as evidenced for instance by results of Bernal *et al.* (2002) for methane, ethane, propane and *n*-butane in a ZSM-5 membrane. Hence, the decrease of methane flux with temperature may reflect the predominance of the decline of the amount of adsorbed molecules, whereas for ethane the enhancement on diffusivity still prevails in this temperature range.

Table VI.6 – Single-component diffusion parameters fitted to the experimental data of van de Graaf *et al.* (1999) for methane (1) and ethane (2).

	$Đ^{s}_{o,1}$ (m^2/s)	$Đ^{s}_{o,2}$ (m^2/s)	$E_{a,s,1}$ (kJ/mol)	$E_{a,s,2}$ (kJ/mol)
Langmuir	8.743×10^{-9}	1.301×10^{-7}	4.592	16.806
Langmuir-Freundlich	3.395×10^{-9}	1.206×10^{-7}	2.360	16.633
Nitta	6.192×10^{-9}	1.300×10^{-7}	4.574	16.815
Toth	2.143×10^{-9}	1.259×10^{-7}	1.780	16.740

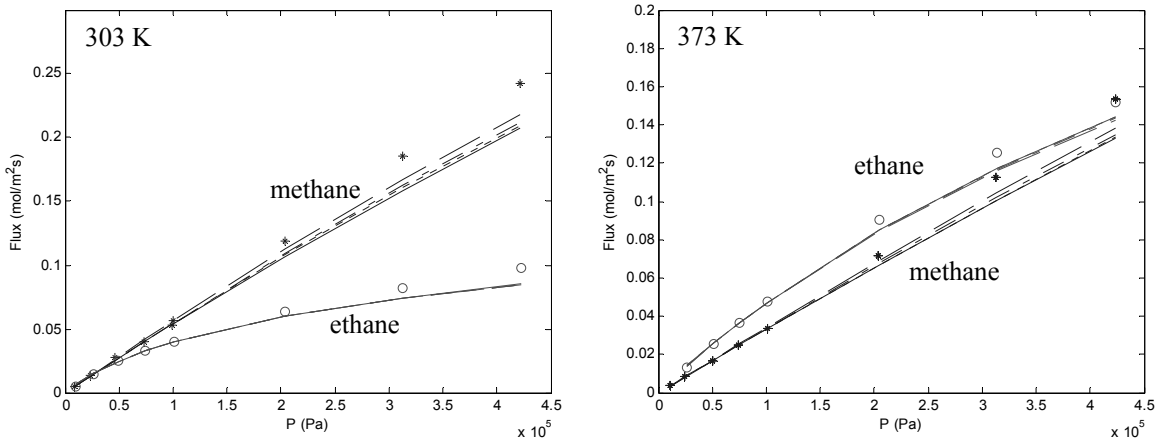

Figure VI.2 – Permeation fluxes of methane and ethane as a function of gas pressure: modelling (this work) and experimental data (van de Graaf *et al.,* 1999). Lines: full lines, Langmuir; dashed lines, Langmuir-Freundlich; dotted lines, Nitta; dash-dotted lines, Toth.

Prediction of binary methane/ethane permeation in a silicalite-1 membrane. Taking into account the estimated binary isotherms and the pure gas diffusivities determined above at 303 and 373 K, the membrane separation of a methane/ethane mixture has been totally predicted at 273, 303, 338, and 373 K, in order to validate the new expressions provided in this work. Our results were compared with the experimental data published by van de Graaf *et al.* (1999) for the silicalite-1 membrane of Table VI.5.

van de Graaf *et al.* (1999) performed experiments with different feed compositions according to the Wicke-Kallenbach technique, i.e. using a constant flow rate of sweep gas (helium) to wash the permeate side. The retentate and permeate sides were well mixed. The counterflux of the sweep gas was considered to be very low at the relatively low temperatures of the experiments (273-373 K), and therefore neglected in their calculations. The authors pointed out that if there was any effect of the sweep gas, it would be lumped in the value of the diffusivity calculated from single-component experiments.

In this work, the prediction of the permeation fluxes was performed without fitting any crossed parameters, by just using the estimated multicomponent isotherms and the Vignes relation (equation (III.42)) for the calculation of the MS surface pair diffusivities $\left(Đ_{ij}^{s}\right)$ from the single ones on the solid $\left(Đ_{i}^{s}\right)$. The resistance of the support layer was included, and the isotherms were once more utilized to calculate the compositions in the feed/zeolite and zeolite/support interfaces. The numerical solution was accomplished by solving simultaneously the generalized MS equations for the zeolite and support layers to obtain their concentration profiles. The resulting ordinary differential equations were integrated using the ode15s function of Matlab.

The calculated results are plotted in Figures VI.3 and VI.4 along with experimental data. Both figures clearly point out the sound predictive capability of the Maxwell-Stefan model combined with the thermodynamic factors derived in this work, since no additional parameter was introduced.

In Figure VI.3, the fluxes of methane and ethane are plotted against ethane partial pressure at 303 K, and emphasizes that all adsorption models give rise to results in good agreement with each other as well as with data points. In this figure, the ethane flux increases by increasing its partial pressure, while methane performs inversely.

Additionally, it should be noted that fluxes predicted adopting Nitta isotherm are slightly higher, while Langmuir equations underestimate them, being such differentiation more evident for methane. This behaviour could be anticipated from the binary isotherms shown in Figure VI.1, where Nitta equation presents the highest values. Nonetheless, equilibrium is still slightly better described by the extended Langmuir and Toth isotherms, although Langmuir-Freundlich and Nitta models also perform quite well. These conclusions are in good agreement with those published by Abdul-Rehman *et al.* (1990), where the Toth model was found to give the best results for the first four alkanes (C1 – C4) adsorption in silicalite-1, for both single component and binary mixtures, being the extended Langmuir equation also adequate for ethane, methane, and ethane/methane adsorption.

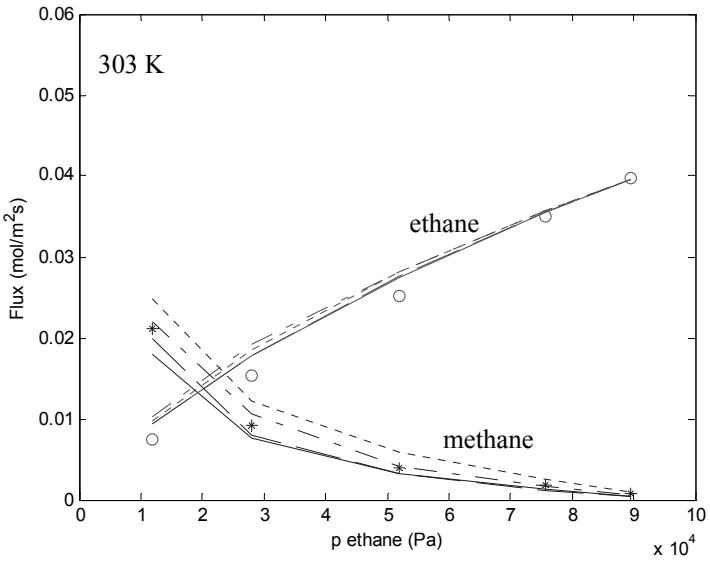

Figure VI.3 – Permeation fluxes of a methane/ethane mixture as function of ethane partial pressure: modelling (this work) and experimental data (van de Graaf *et al.,* 1999). Lines: full lines, Langmuir; dashed lines, Langmuir-Freundlich; dotted lines, Nitta; dash-dotted lines, Toth.

In Figure VI.4, the permeation fluxes of methane and ethane are plotted against temperature for a 1:1 (mol) mixture. These results point out that the binary permeation behaviour may be not solely anticipated by single-component results. In fact, in the case of two adsorbable gases, the most adsorbed one may permeate preferentially through the

zeolitic pores, hindering the diffusion of the second molecule. Accordingly, the methane flux in the binary mixture is smaller. Moreover, as temperature rises, the permeation of ethane decreases after 338 K, since its concentration in silicalite-1 diminishes and leaves more vacant sites available for methane. As in Figure VI.3, the results calculated with the Nitta isotherm overpredict methane behaviour, whereas Langmuir presents systematically inferior values.

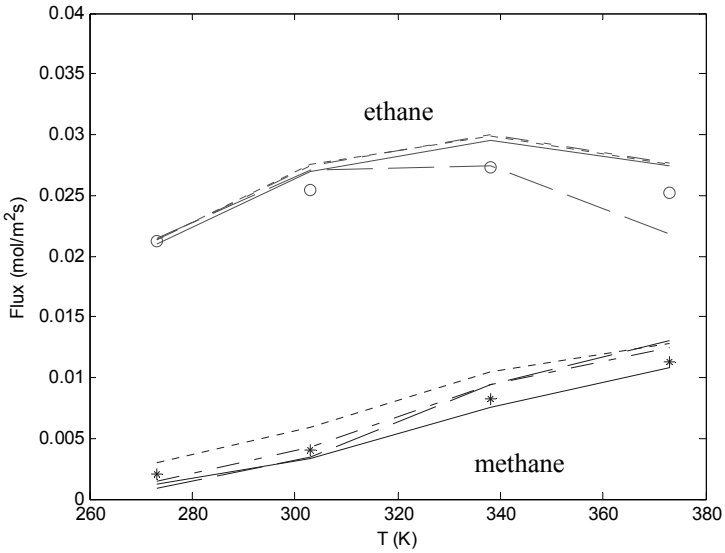

Figure VI.4 – Permeation fluxes of a 1:1 (mol) methane/ethane mixture as function of temperature: modelling (this work) and experimental data (van de Graaf *et al.,* 1999). Lines: full lines, Langmuir; dashed lines, Langmuir-Freundlich; dotted lines, Nitta; dash-dotted lines, Toth.

2. Dynamic characterization of microporous membranes

2.1 Single gas permeation

During this work nineteen microporous membranes were synthesized by CICECO research team, namely nine of titanosilicate AM-3, five of titanosilicate ETS-10, four of zeolite ZSM-5, and a last one of zeolite 4A. All of these membranes were firstly characterized by measuring N_2 permeance at room temperature, in order to investigate the existence of rough defects in their crystalline structure. Generally, permeances of small gases through microporous membranes higher than 10^{-6} mol/m^{2}s.Pa point out rough deficiencies. If gases with kinetic diameters larger than crystal pore size do permeate, the same conclusion may be drawn. The average pore diameter of AM-3, ETS-10, ZSM-5, and zeolite 4A are 0.3, 0.49×0.76, 0.55, and 0.4 nm, respectively, and the kinetic diameter of N_2 is 0.346 nm. Consequently, N_2 permeation flux abnormally high reveal considerable defect density on the membrane structure. Even though the pore dimensions of the several materials studied are different, only membranes with N_2 permeance inferior to 10^{-6} mol/m^{2}s.Pa were considered for further detailed characterization. Please note that the kinetic diameter of N_2 is larger than AM-3 pore diameter, and accordingly no permeance should be detected at all. However, a perfect microporous membrane is difficult to achieve and macro, meso or even microdefects may be always present in real systems. In addition, it is important to note that permeance depends on the membrane thickness (please see equation (II.1)), so comparison between different membranes should be made with caution.

Table VI.7 lists N_2 permeances at room temperature for all membranes studied. According to the above mentioned primary criteria for membranes quality, AM-3-1 membrane was excluded from the detailed characterization, since its N_2 permeance was considerably high. Concerning AM-3-3, AM-3-4, and AM-3-5 membranes, their results are within the typical permeance range ($1-10\times10^{-7}$ mol/m^{2}s.Pa), suggesting good quality membranes, i.e. without a significant amount of large defects. Hence, these membranes were subjected to subsequent detailed characterization, namely permeation at programmed temperature (PPT) experiments using different gases and at several transmembrane

pressure drops. From temperature-permeation curves it is possible to identify the prevailing transport mechanisms involved and subsequently detect defects.

AM-3-7, AM-3-8, AM-3-9, AM-3-10, and AM-3-11 membranes were synthesized after characterization of the first four AM-3 membranes. Their N_2 permeances were measured after a first synthesis and values superior to those of previous three membranes were found. Since membranes exhibiting smaller N_2 permeances are desired, they were submitted to a second synthesis step. After this second crystallization, N_2 permeances were found to be not significantly reduced, being still larger for AM-3-8, AM-3-9, and AM-3-10 membranes. This suggests that a second synthesis can result in a membrane of lower quality. Similar results were obtained by Lin *et al.* (2004) for ETS-10 membranes, which were attributed to the partial dissolution of the first formed ETS-10 layer, hindering a good intergrowth between neighbour crystals. In an attempt to improve the quality of the three above cited membranes a third synthesis step is presently in course.

The nitrogen permeances of the five ETS-10 membranes studied are slightly higher than the reference values range ($>10^{-6}$ mol/m^{2}s.Pa). Similarly to the last five AM-3 membranes, ETS-10-4 and ETS-10-5 membranes were subjected to additional titanosilicate layers deposition. Concerning ETS-10-4 membrane, after the second synthesis its N_2 permeance decreased below the detection limit of the experimental set-up, and accordingly no additional measurements were possible. On the other hand, the permeance of ETS-10-5 membrane was only slightly decreased, and therefore a third synthesis was carried out. After this last crystallization step, N_2 permeance was found be to significantly reduced. Hence, ETS-10-5 membrane was also considered for further characterization.

With respect to the ZSM-5 membranes, only the first one presents an acceptable N_2 permeance, i.e. below 10^{-6} mol/m^{2}s.Pa. In fact, the permeance of ZSM-5-1 membrane was considerably small (5.21×10^{-8} mol/m^{2}s.Pa) indicating probably a noticeable low defects density. Despite the well-established characterization of ZSM-5 membranes, this membrane was subjected to further permeation tests because of its interesting organophilic character, distinct of that of AM-3, ETS-10 and zeolite 4A. Hence, single N_2 and CO_2 permeance measurements at two fixed temperatures were carried out.

A similar procedure was adopted for testing the zeolite 4A membrane quality, resulting in a N_2 permeance of 4.30×10^{-8} mol/m^{2}s.Pa after three crystallization steps. This membrane was thus subsequently submitted to experiments at programmed temperature, in order to detect the transport mechanism involved in gas transport. However, results are not presented since the support started to oxidize.

Table VI.7 – Nitrogen permeances for the various membranes studied in this work, together with permeances of supports used, at room temperature.

Membrane/support	**No. separation layers**	Π **(mol m^{-2}s^{-1}Pa^{-1})**
AM-3-1	1	1.95×10^{-5}
AM-3-3	1	3.14×10^{-8}
AM-3-4	1	1.17×10^{-7}
AM-3-5	1	5.98×10^{-7}
AM-3-7	2	5.16×10^{-6} / 3.36×10^{-6}
AM-3-8	2	2.35×10^{-7} / 1.30×10^{-6}
AM-3-9	2	2.96×10^{-7} / 9.62×10^{-7}
AM-3-10	2	1.22×10^{-6} / 6.38×10^{-6}
AM-3-11	2	4.62×10^{-6} / 1.07×10^{-6}
ETS-10-1	1	2.77×10^{-6}
ETS-10-2	1	3.10×10^{-6}
ETS-10-3	1	1.21×10^{-6}
ETS-10-4	2	4.81×10^{-6} / $<1\times10^{-9}$
ETS-10-5	3	7.10×10^{-6} / 2.07×10^{-6} / 2.26×10^{-8}
ZSM-5-1	1	5.21×10^{-8}
ZSM-5-2	1	3.16×10^{-6}
ZSM-5-3	1	6.26×10^{-6}
ZSM-5-4	1	1.85×10^{-5}
4A	3	1.94×10^{-6} / 1.80×10^{-6} / 4.30×10^{-8}
α-alumina (1900 nm)	-	7.08×10^{-5}
α-alumina (3000 nm)	-	3.56×10^{-4}
Stainless-steel (500 nm)	-	5.73×10^{-5}

The N_2 permeance of three supports used in membranes synthesis, namely two of α-alumina and one of stainless-steel, were measured for comparison (please see Table VI.7). As expected, their permeance is considerably higher, especially those of α-alumina because of their macroporous structure. It is clear from these values that even for more permeable membranes their permeance is significantly reduced after deposition of titanosilicate or zeolite separation layers.

Membranes pre-treatment

Before the dynamic characterization of the membranes, a previous heating and cooling cycle was carried out in order to remove adsorbed compounds. Figure VI.5 shows permeation fluxes as function of transmembrane pressure drop for both ETS-10-1 and AM-3-4 membranes, at room temperature, before and after the heating and cooling cycle up to around 200ºC. Calculated permeances, corresponding to the slope of the linear fitting to experimental data, are indicated in Table VI.8. These figures point out an enhancement of N_2 permeation fluxes. After the thermal treatment the effective pore size becomes large due to the removal of water or other eventually adsorbed molecules, supporting the hydrophilic character of both ETS-10 and AM-3 crystals.

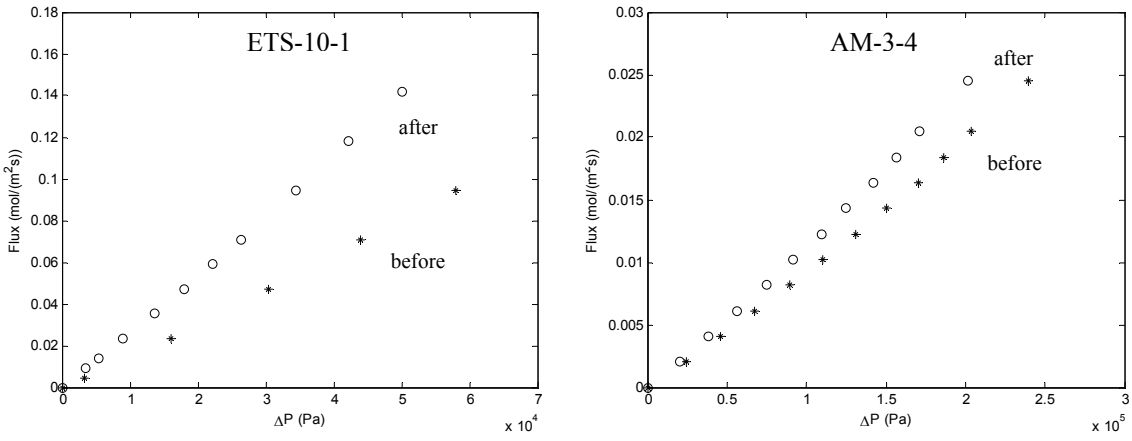

Figure VI.5 – N_2 permeation fluxes at room temperature, before and after the heating and cooling cycle, for ETS-10-1 and AM-3-4 membranes.

Table VI.8 – Nitrogen permeance at room temperature before and after the heating and cooling cycle.

Permeance (mol/m^{2}sPa)		
ETS-10-1	Before heating	1.61×10^{-6}
	After heating	2.77×10^{-6}
AM-3-4	Before heating	9.81×10^{-8}
	After heating	1.17×10^{-7}

ETS-10-3 membrane

The nitrogen permeance of the ETS-10-3 membrane at room temperature, presented in Table VI.7, is clearly outside the typical range ($\Pi = 1.21\times10^{-6}$ mol/(m^{2}sPa)), which may indicate the presence of a significant amount of mesopores and even of large macro-defects on the crystalline structure. Figure VI.6 shows the permeation fluxes of N_2 as function of the transmembrane pressure drop, at 24 and 55ºC, and the corresponding permeances calculated according to equation (II.3). Generally, non-adsorbable gases or gases with linear adsorption isotherms (Henry regime) show a linear relation between permeation flux and pressure gradient across the membrane and so pressure-independent permeances. In contrast, Figure VI.6a evidences a nonlinear dependence of N_2 flux on pressure, which may be attributed to the contribution of viscous flow mechanism to the total permeation. Such contribution is also evidenced by the pressure-dependence of permeance (Figure VI.6b), as well as by permeance decline with increasing temperature (see equation (III.2)).

The main objective of the membranes studied in this work concerns the separation of small gases. Since ETS-10-3 membrane presents a considerably amount of macro-defects, where non-selective viscous mechanism dominates, this membrane would not be suitable for this purpose. Hence, no additional tests were performed with this membrane.

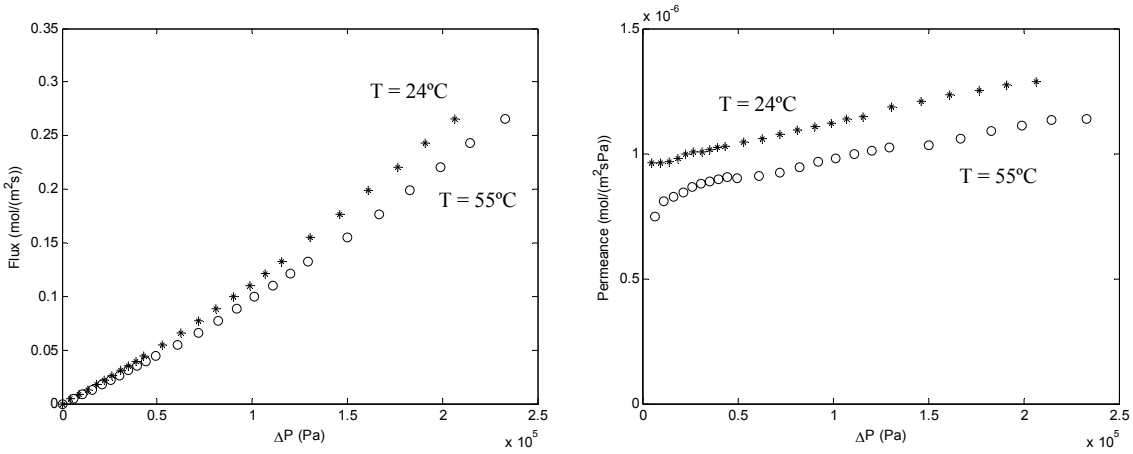

Figure VI.6 – a) N_2 permeation fluxes and b) corresponding permeances of ETS-10-3 membrane at 24 and 55ºC.

ETS-10-5 membrane

The N_2 permeance of ETS-10-5 membrane after the first synthesis step (Table VI.7) was significantly higher than the typical permeance range for micropores ($7.10\times10^{-6} > 10^{-6}$ mol/m^{2}sPa). A permeation at programmed temperature experiment was subsequently carried out in order to verify the existence of macro- and/or mesopores. The obtained results, presented in Figure VI.7a, evidence the expected decrease of the permeance with temperature, confirming the existence of such defects.

A second crystallization was carried out in order to improve membrane quality. After this synthesis, the N_2 permeance has decreased *ca.* three times, which indicates that some large defects were probably fixed. However, the decrease in permeance was not as pronounced as required, and thus a significant amount of defects still existed in the membrane, as supported by the PPT results pictured in Figure VI.7a. Nonetheless, it should be emphasized that the permeance decline after the second synthesis is considerably smoother for the same transmembrane pressure drop (0.5 bar).

After a third titanosilicate layer synthesis, a meaningful decrease in permeance was finally found, i.e., it dropped two orders of magnitude. Accordingly, most of the larger defects presented initially in the ETS-10-4 membrane were possibly eliminated after three synthesis. In this case, the PPT results, presented in Figure VI.7b, reveal a distinct

temperature dependence. In the lower temperature range, the permeance decreases owing to the Knudsen contribution, and eventually to some residual viscous flow through the persisting defects of the titanosilicate layer, while it increases monotonously at higher temperatures due to activated diffusion through micropores. This result indicates that the quality of the membrane was significantly improved. It should be noted that the last PPT run was carried out with a transmembrane pressure drop as high as 5 bar, since for lower driving forces the permeation fluxes were not measurable (values below the detection limit of the equipment).

Similar results were obtained by Xu *et al.* (2005), who employed a multi-stage synthesis method for preparation of NaA membranes and found the best quality membrane after a three-stage synthesis. Tiscornia *et al.* (2005) also obtained a higher quality ETS-10 membrane after a two-step seeded synthesis.

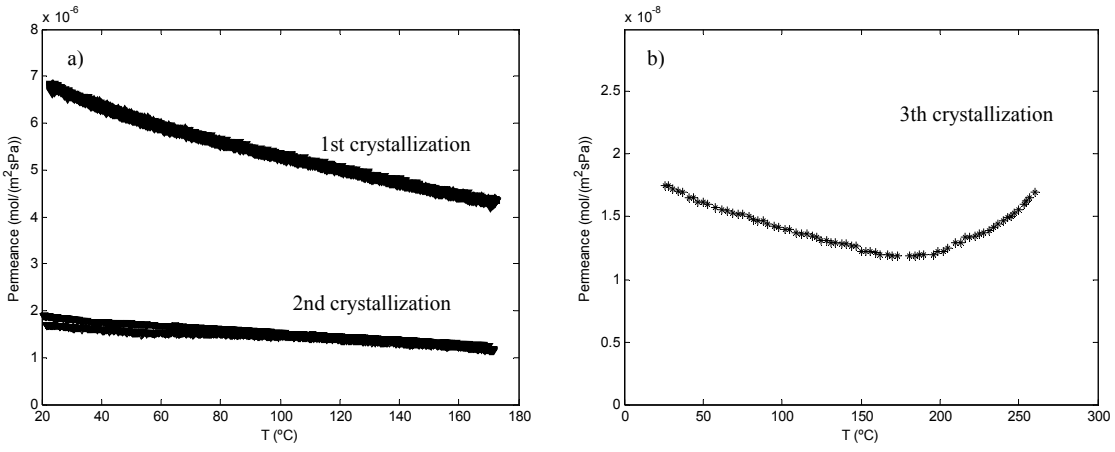

Figure VI.7 – N_2 permeance at programmed temperature of ETS-10-4 membrane a) after the first and second crystallization steps for ΔP = 0.5 bar, and b) after the third crystallization for ΔP = 5 bar.

AM-3-3 membrane

The permeance of He, H_2, N_2, and CO_2 in the AM-3-3 membrane was measured along with temperature. Figure VI.8 shows the PPT results for these gases, measured under the same transmembrane pressure drop of 1 bar. As may be observed, CO_2 and N_2 show similar permeances of $0.2 – 0.4\times10^{-7}$ mol/(m^2sPa), which are significantly lower than those of He and H_2 ($0.7 – 1.2\times10^{-7}$ mol/(m^2sPa)). It should be noted that the permeation of bulkier N_2 and CO_2 molecules may be only attributed to the transport through defects larger than the titanosilicate pores, since the kinetic diameters of these gases (0.364 and 0.33 nm, respectively) are larger than the AM-3 pore size (0.3 nm). In addition, since H_2 and He are smaller than the pore diameter, one could expect the permeance of these molecules to be governed by activated diffusion and display a clear increase with temperature. However, both H_2 and He are small molecules capable of high permeation rates through inter-crystalline defects. Thus, in membranes with significant defect density the effect of permeation through defects could overcome activated contribution in the micropores. Therefore, the descending pattern of this membrane may be considered a reliable indicator of the presence of defects.

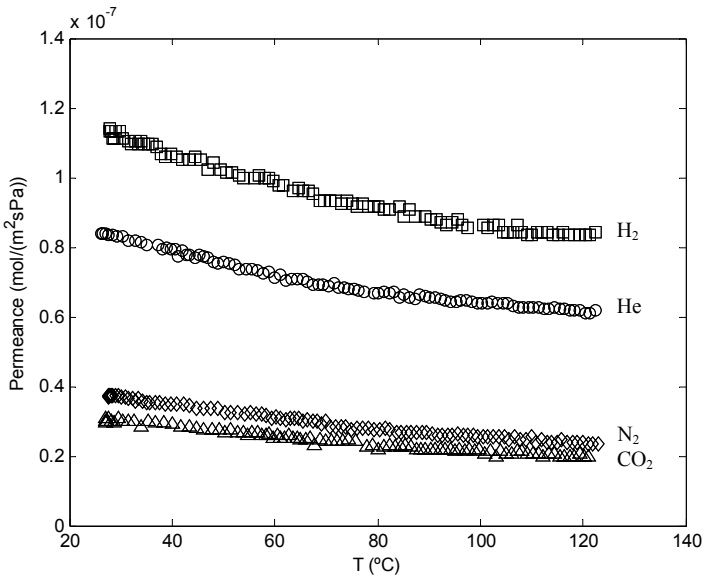

Figure VI.8 – Permeances of He, H_2, N_2 and CO_2 measured at programmed temperature in the AM-3-3 membrane for ΔP = 1 bar.

Figure VI.9 compares the permeance of He, H_2, N_2 and CO_2 obtained for two distinct transmembrane pressure drops: 1 and 2 bar. It is clear that ΔP has only a mild effect on the permeance, especially for He and H_2. However, an increase of the permeance with pressure was found for all the gases, corroborating the contribution of viscous flow to the total permeation. It is important to note that He and H_2 diffusion is less dependent on the pressure, since their transport may occur through micropores and defects also, while N_2 and CO_2 diffuse uniquely through defects given their kinetic diameters larger than AM-3 pore size. Accordingly, the contribution from viscous flow is expected to be more important for N_2 and CO_2.

Figure VI.9a presents two overlapped permeation curves for He at $\Delta P = 2$ bar, being the first one measured only until 120ºC, while the second one was carried out up to 170ºC, and after all the other PPT runs with the remaining gases. The results for the second PPT experiment were consistent with those previously obtained and reveal the predominance of gas transport through macro and/or meso-defects even for higher temperatures. In addition, the membrane is found to be stable during repeated heating and cooling cycles in this temperature range.

The relationship between the permeance of the AM-3-3 membrane and the kinetic diameters and molecular weight of the permeating gases is presented in Figure VI.10. This figure emphasizes a clear permeance dependence on both properties. Moreover, as previously discussed, a pronounced permeance decline may be observed for gases with kinetic diameter superior to the AM-3 pore size, reporting at least some molecular sieving effect (see Figure VI.10a). Observed results also showed a clear trend of decreasing permeance with increasing molecular weight, following the typical behaviour of Knudsen diffusion (see Figure VI.10 b and equation (III.6)).

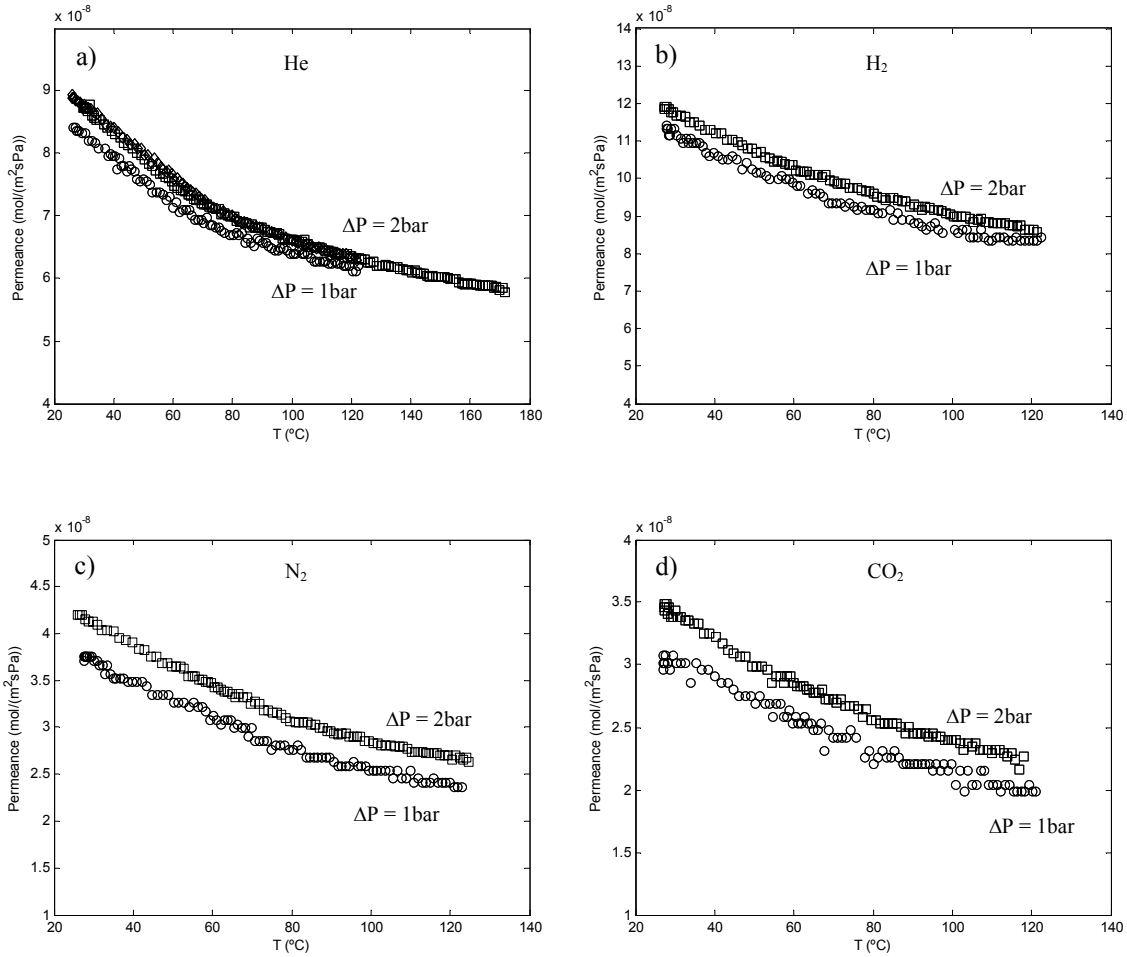

Figure VI.9 – Permeances measured at programmed temperature in the AM-3-3 membrane under ΔP = 1 and 2 bar for a) He, b) H_2, c) N_2 and d) CO_2.

The dominance of the Knudsen mechanism can be further verified in Figure VI.11, where the permeance of the four studied gases shows a linear trend with the inverse of the square root of the molecular weight (see Figure VI.11a), as expected for this transport mechanism (see equation (III.6)). Concerning the viscous flow mechanism, its dependence on gas viscosity implies a dependence on both kinetic diameter and molecular weight. Following, for instance, the method of Chung *et al.* (1984) for estimating gas viscosity, based on the theory of Chapman and Enskog, such dependence may be described by $\eta \propto M^{0.5}/d_k^2$. It is clear from Figure VI.11b that the permeances roughly follow the inverse of the square root of molecular weight multiplied by the corresponding square of kinetic diameter, indicating as well some contribution from viscous flow.

According to the previous results, it may be concluded that gas transport through the AM-3-3 membrane is clearly dominated by both Knudsen and viscous flow mechanisms.

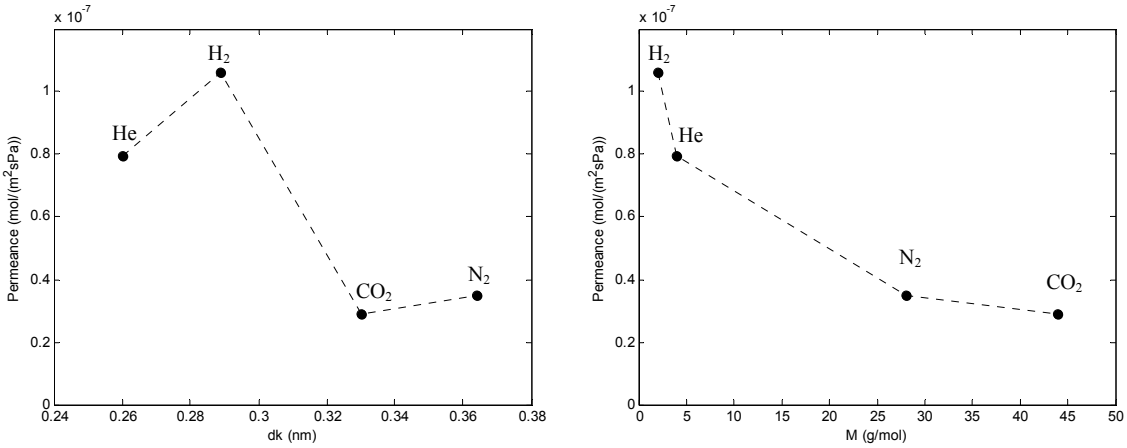

Figure VI.10 – Dependence of He, H_2, N_2 and CO_2 permeances in the AM-3-3 membrane on a) gas molecular diameters (Breck, 1974) and b) molecular weights, for 40ºC and ΔP = 1 bar.

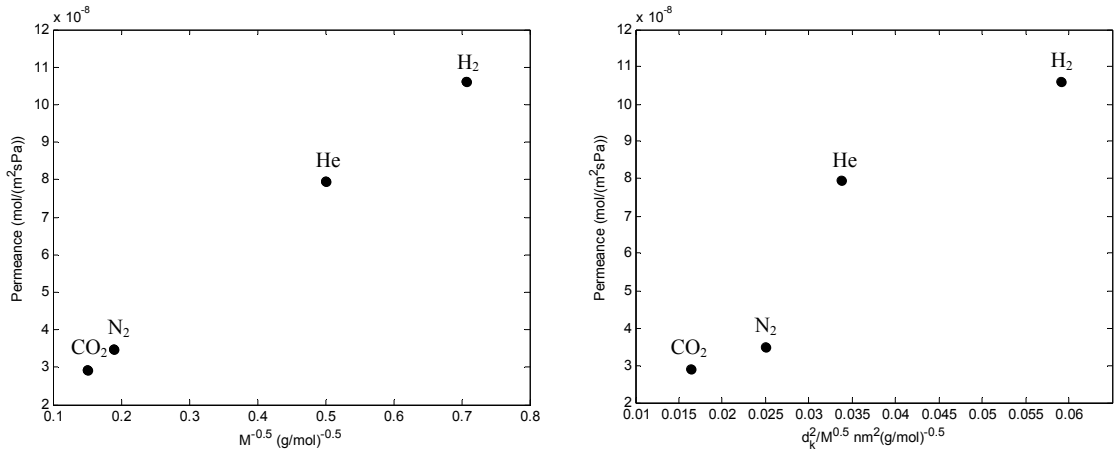

Figure VI.11 – Permeance of He, H_2, N_2, and CO_2 in the AM-3-3 membrane as function of a) the inverse of the square root of their molecular weight and b) the ratio between the square of kinetic diameters and the square root of their molecular weight, for the same operating conditions as in Figure VI.10 (40 ºC and ΔP = 1 bar).

Figure VI.12 shows the ideal selectivities of H_2/CO_2, H_2/N_2, He/CO_2 and He/N_2, He/H_2 and N_2/CO_2 calculated based on the permeance data for 40, 70, 100, and 120ºC. For comparison, the corresponding values calculated from Knudsen diffusion were compiled in Table VI.9. It may be observed that ideal selectivities for all binary systems are quite similar to those for Knudsen mechanism, which is in total accordance with the previous discussion (see Figure VI.11). Moreover, ideal selectivities relative to gases with similar kinetic diameter and molecular weight, namely for He/H_2 and N_2/CO_2, are close to unity and almost independent of temperature. In contrast, ideal selectivity for gases with more distinct kinetic diameters and molecular weight (for H_2/CO_2, H_2/N_2, He/CO_2 and He/N_2) are higher, evidencing at least a small contribution from molecular sieving. Moreover, these increase slightly with temperature.

Table VI.9 – Knudsen selectivities.

He/CO_2	He/N_2	N_2/CO_2	He/H_2	H_2/N_2	H_2/CO_2	H_2/O_2	CO_2/O_2
3.32	2.65	1.25	1.41	3.74	4.69	4.00	0.85

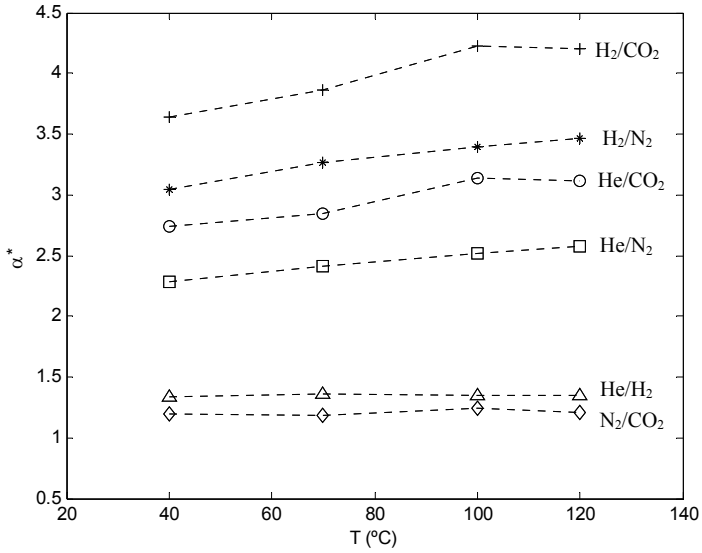

Figure VI.12 – Ideal selectivities for several binary systems as function of temperature in AM-3-3 membrane.

Experimental data for single gas permeation were modelled based on single component transport mechanisms described in Chapter III. Transport through macro- and meso-defects was described by both Knudsen and viscous flow, while micropore diffusion was assumed to occur by activated gaseous mechanism. Previous studies (Lin *et al.*, 1997) have revealed that N_2 is practically non-adsorbed on AM-3. Since permeation results do not evidence the contribution of surface diffusion (i.e. the presence of a minimum followed by a maximum in the $\Pi - T$ curve), for the remaining gases it was not taken into account.

Equation (III.26) was adopted to fit the experimental data of Figure VI.8, by taking $\Pi_s = 0$ as aforementioned. A geometric factor, g_{sup}, was included in order to take the support effect into account. The membrane geometrical parameters for Knudsen and viscous flow mechanisms were considered equal for all gases, since they only depend on membrane features. In contrast, for activated diffusion one distinct constant accounting for geometrical parameters was fixed for molecules capable to permeate AM-3 pores (H_2 and He) and another one for molecules larger than AM-3 pore diameter (N_2 and CO_2). This distinction is due to the fact that H_2 and He, and N_2 and CO_2 diffuse through different microporous pathways, i.e., AM-3 structural pores and larger intercrystalline micropores.

Figure VI.13 shows model results together with experimental data. The calculated parameters are compiled in Table VI.10. The figure points out the reliable agreement between modelling and experimental data, corresponding to $AARD = 5.9\%$, being the higher deviations found for the lower temperature range. The different contributions of each individual transport mechanism for H_2 permeation are illustrated in Figure VI.14. As may be observed, H_2 permeance takes place mainly by Knudsen diffusion, with a minor contribution from viscous flow. Besides, as expected from the decreasing trend of permeance against temperature, the activated gaseous diffusion is not significant. These results are in total agreement with the previous discussion.

The optimized parameter of the activated diffusion of molecules larger than AM-3 pore size, i.e. N_2 and CO_2, is one order of magnitude inferior to that of H_2 and He (1.719×10^{-11} *versus* 2.148×10^{-10}), due to the relative sizes of the molecules and the permeated pores. With respect to the activation energies, the small values found for N_2 and CO_2 (1.7 and 4.0 kJ/mol, respectively) in relation to those of H_2 and He (13.3 and 11.0

kJ/mol, respectively) rely upon the average pore diameters where diffusion occurs, namely the inter and intracrystalline micropores of the AM-3 membrane. In particular, $E_{a,g}(H_2) > E_{a,g}(He)$ reflects the same relation between their kinetic diameters, since both molecules prevail on the same type of pores.

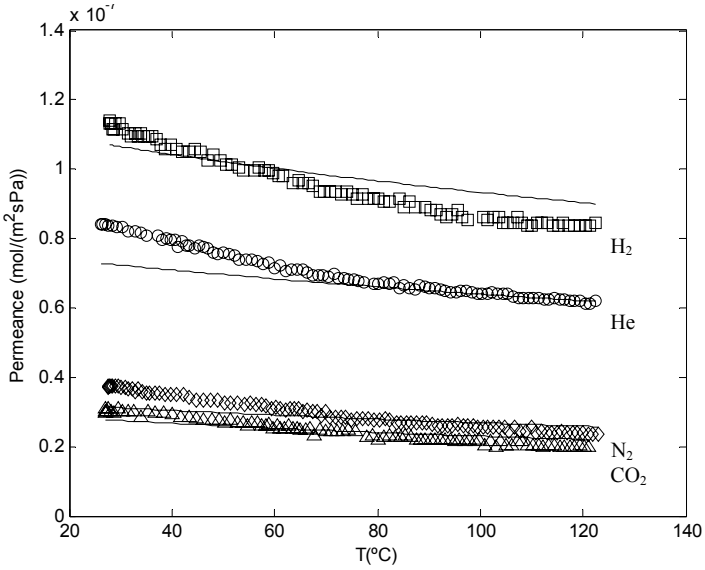

Figure VI.13 – Modelling and experimental results for permeation of H_2, He, N_2, and CO_2 in AM-3-3 membrane (ΔP = 1 bar).

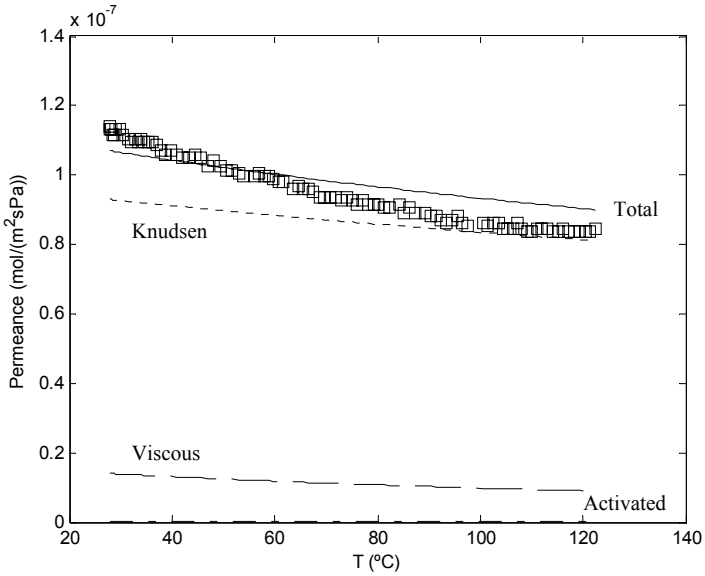

Figure VI.14 – Contributions of different transport mechanism for H_2 permeation in AM-3-3 membrane (ΔP = 1 bar).

Table VI.10 – Model parameters for H_2, He, N_2, and CO_2 diffusion in AM-3-3 membrane.

$g_{sup}\frac{\varepsilon d_p^2}{32\tau\delta\Re}$ $(m\,mol\,K/J)$	$g_{sup}\frac{\varepsilon d_p}{3\tau\delta}\left(\frac{8}{\pi\Re}\right)^{0.5}$ $(mol\,K/J)^{0.5}$	$g_{sup}\frac{l_d}{Z\delta}\left(\frac{8}{\pi\Re}\right)^{0.5}$ $(mol\,K/J)^{0.5}$	$E_{a,g}(kJ/mol)$			
			H_2	He	N_2	CO_2
2.309×10^{-16}	7.244×10^{-8}	1.719×10^{-11} (N_2 and CO_2) 2.148×10^{-10} (H_2 and He)	13.3	11.0	1.7	4.0

AM-3-4 membrane

The effect of temperature and pressure on the permeation of the AM-3-4 membrane was investigated by measuring the N_2 permeation flux for several transmembrane pressure drops at 25, 100, and 140 ºC.

Figure VI.15 presents the obtained N_2 fluxes and the corresponding permeances along with the transmembrane pressure drop. As may be observed, the N_2 permeance decreases with increasing temperature, as expected for both Knudsen and viscous mechanisms. In addition, it follows a linear pressure-dependence, which is characteristic of the viscous flow mechanism (see equation (III.2)). Once more, permeation at programmed temperature experiments, under two distinct transmembrane pressure drops (1 and 2 bar), were performed in order to identify the prevailing transport mechanisms.

PPT results, shown in Figure VI.16, are in good agreement with those obtained for fixed temperatures, i.e., the N_2 permeance decreases over all the temperature range studied, being enhanced with the transmembrane pressure difference. Such results denunciate a significant amount of macro-defects on the AM-3-4 membrane structure. Accordingly, no additional characterization tests were carried out on this membrane, since it is not suitable for desired separations.

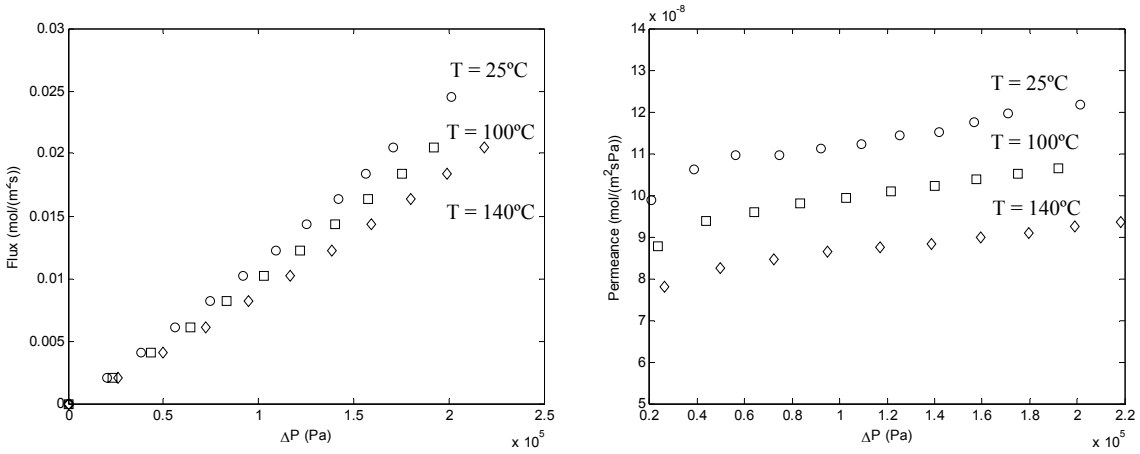

Figure VI.15 – a) N_2 permeation flux and b) corresponding permeances along with the transmembrane pressure drop for the AM-3-4 membrane, at 25, 100 and 140ºC.

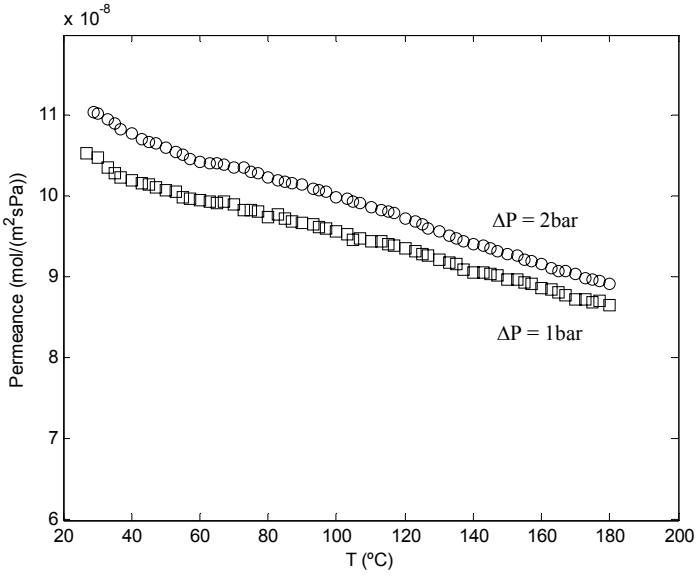

Figure VI.16 – Effect of temperature and pressure on the N_2 permeance of the AM-3-4 membrane.

AM-3-5 membrane

The permeance of several gases through AM-3-5 membrane was continuously measured along with temperature. Figure VI.17 illustrates the PPT results for H_2, N_2, CO_2 and O_2, through the AM-3-5 membrane at ΔP = 0.2 bar. Also in this case, gases with kinetic

diameters larger than AM-3 pore size, i.e. N_2, CO_2, and O_2, were found to permeate the membrane, indicating the presence of defects larger than AM-3 structural pores. In contrast, due to their smaller dimensions, H_2 molecules are able to easily diffuse through AM-3 pores as well as through larger defects and, accordingly, their permeance is considerably higher.

Figure VI.17 shows an initial plateau in the H_2 permeance, followed by a subsequent monotonous increase with temperature. This behaviour is frequently found for diffusion of small permanent gases through real microporous membranes, and can be explained by the simultaneous occurrence of distinct transport mechanisms. At lower temperatures, Knudsen and viscous flow through macro and/or meso-defects may prevail, whereas at higher temperatures transport occurs via activated gaseous diffusion through micropores. Although a significant density of defects may be present, the permeance increase with temperature indicates a preponderance of activated permeation through the microporous titanosilicate layer and, therefore, a lower concentration of defects may be admitted. Such increasing trend is expected to be more pronounced at higher temperatures.

Concerning N_2, CO_2 and O_2 diffusion, their permeance was found to be less dependent on temperature. This may be due to an equilibration between the competitive mechanisms discussed above. Given this behaviour, at least some defects are expected to be of a size roughly similar to those of N_2, CO_2 and O_2 molecules. However, the activated diffusion eventually present in such micro-defects may be not as significant as for H_2 diffusion, and thus not important enough to prevail in the temperature range studied. Moreover, based on permeation results for these gases on microporous zeolite-type materials, their activation energy for diffusion is expected to be larger than that of H_2, and, accordingly, higher temperatures are required to allow them to overcome the pore structure restrictions. In fact, this behaviour is frequently reported in the literature for permeation through microporous membranes. For instance, Aoki *et al.*, (1998) reported N_2 and CO_2 permeances unchanged with temperature up to 100ºC through an A-type zeolite membrane. Poshusta *et al.*, (1998) presented the permeation results of several gases through a SAPO-34 membrane and showed N_2 and CO_2 permeances considerably less temperature-dependence exhibiting a slight minimum. Bernal (2002) presented almost temperature-

independent results for permeation of H_2 through a ZSM-5 membrane, and permeation of N_2 through MOR and ZSM-5 membranes.

Figure VI.18 shows the effect of the transmembrane pressure drop on H_2 permeation. It is clear from this figure that the H_2 permeance is only slightly influenced by pressure, indicating the presence of some large defects. However, the extent of such defects cannot be surely deduced from these results once the ΔP values studied are not sufficiently different. Nonetheless, experiments for higher fluxes, i.e. for conditions where permeances are much superior, could not be carried out due to set-up limitations.

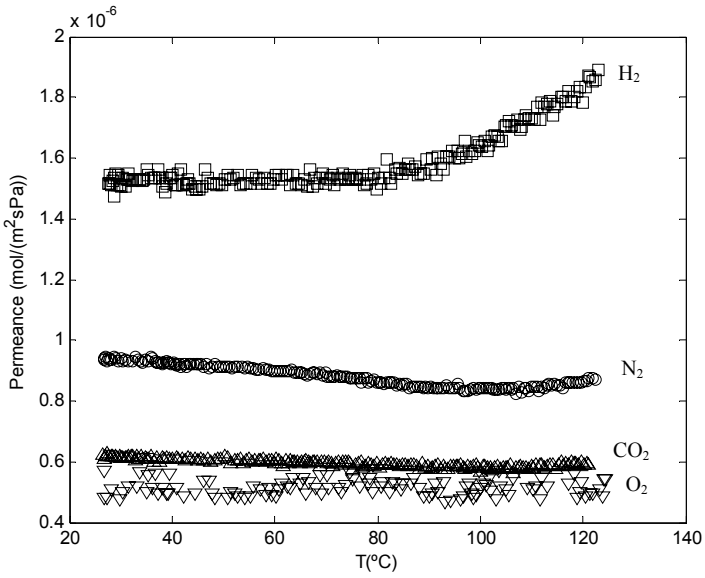

Figure VI.17 – Permeance of H_2, N_2, CO_2, and O_2 at programmed temperature of AM-3-5 membrane for ΔP = 0.2 bar.

The dependence of permeances on kinetic diameter and molecular weight of permeating gases are pictured in Figure VI.19a and VI.19b. As may be observed, in general no specific relationships were found between permeances and kinetic diameters or molecular weights. However, the permeance of the smaller H_2 molecules stills detaches from the remaining gases, indication some contribution from molecular sieving effect. The permeances of gases larger that AM-3 pores are not greatly dependent on the molecular

size, since the aperture of defects is larger than the size of these molecules. Concerning molecular weight, permeances decrease with increasing M , except for the heaviest CO_2, which permeates faster than O_2.

The dependence of permeation on the molecular weight of diffusing gases was further investigated by representing their permeances against the inverse of square root of molecular weights (see Figure VI.20). As expected, in this case permeances did not perfectly scale with the square root of their molar mass ratios. Besides, a linear dependence on the ration between the square of kinetic diameter and the square root of molecular weight, as expected for the viscous mechanism, was not found as well. Based in these results one may conclude that neither the Knudsen mechanism nor the viscous one may be assumed predominant.

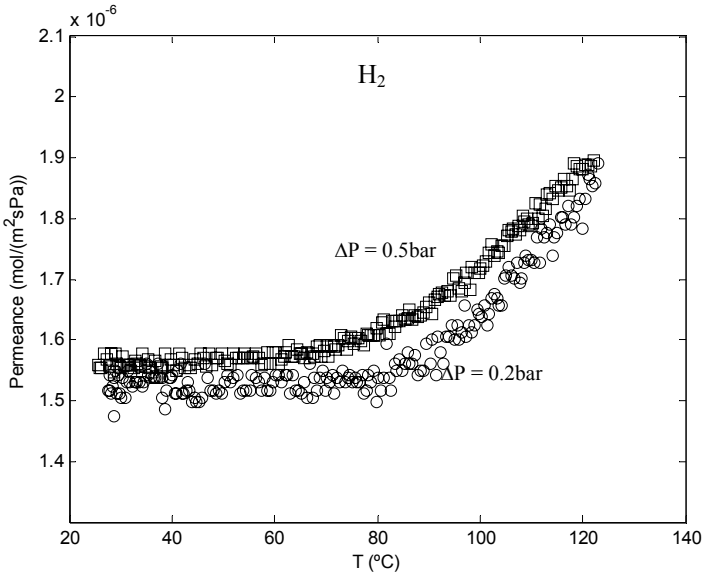

Figure VI.18 – Permeance of H_2 at programmed temperature of AM-3-5 membrane under ΔP = 0.2 and 0.5 bar.

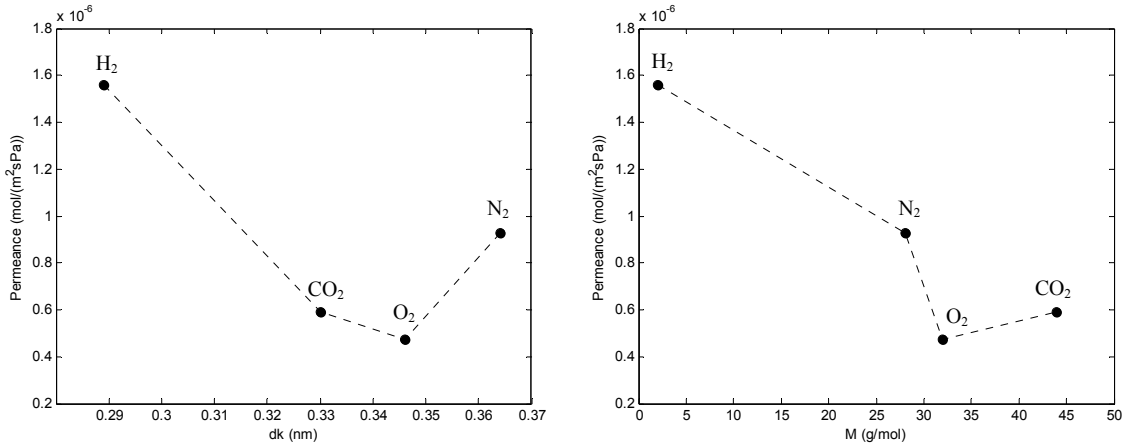

Figure VI.19 – Dependence of H_2, N_2, O_2, and CO_2 permeances in the AM-3-5 membrane on a) gas kinetic diameters and b) molecular weights, for 40ºC and $\Delta P = 0.2$ bar.

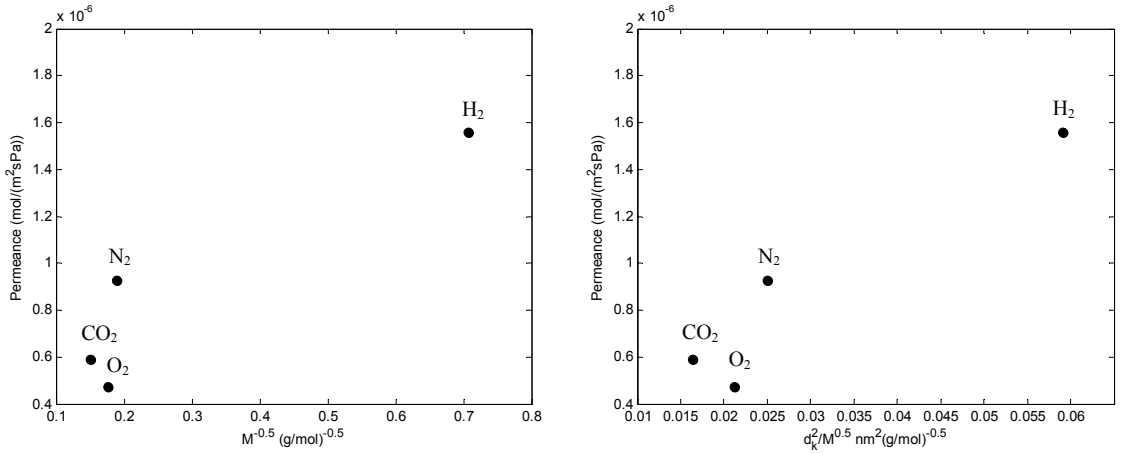

Figure VI.20 – Permeance of H_2, N_2, O_2, and CO_2 in the AM-3-5 membrane a) as function of the inverse of the square root of their molecular weight and b) in function of the ratio between the square of kinetic diameter and the inverse of the square root of their molecular weight, for the same operating conditions as in Figure VI.19 (40 ºC and $\Delta P = 0.2$ bar).

The effect of the presence of water within AM-3 framework was evaluated by carrying out PPT experiments after the membrane humidification. For this purpose, a water-saturated stream of H_2 and CO_2 was flowed through the membrane during 1 hour, at 80ºC. Figure VI.21 shows the PPT results for H_2 and CO_2 before and after the membrane humidification run, carried out with dry H_2 and CO_2 streams. Results show a pronounced

decrease of both H_2 and CO_2 permeances after humidification, probably due to the blockage of titanosilicate pores or inter-crystalline pores. This is a totally expectable result given the high hydrophilic character of AM-3 crystals. Besides, the activated tendency was improved for both gases. This may be due to the blockage of some inter-crystalline defects, which could allow an earlier prevalence of activated diffusion for lower temperatures. In addition, the removal of water molecules by increasing temperature may be also responsible for the remarkable increase of H_2 and CO_2 permeances for higher temperatures.

The beneficial effect of water in hydrophilic membrane separations has been investigated by Sebastian *et al.* (2008) for the separation of H_2 from N_2 in the presence of moisture using a microporous titanosilicate AM-2 membrane. In their study, a $H_2O/H_2/N_2$ mixture was fed to the membrane with a water relative pressure of 0.7, which is high enough to ensure capillary condensation of water in inter-crystalline defects. It was found that unlike other zeolitic membranes, moisture did not seem to permeate through the intrinsic micropores of AM-2 but used the inter-crystalline defects existing in the membrane where it was capillary condensed. This gave rise to a tremendous increase of the H_2/N_2 selectivity (from close to 50 to more than 800) in the presence of a sufficient high partial pressure of water. However, no significant effect was found when using a hydrophilic mordenite membrane, once its micropores are large enough to allow the passage of water.

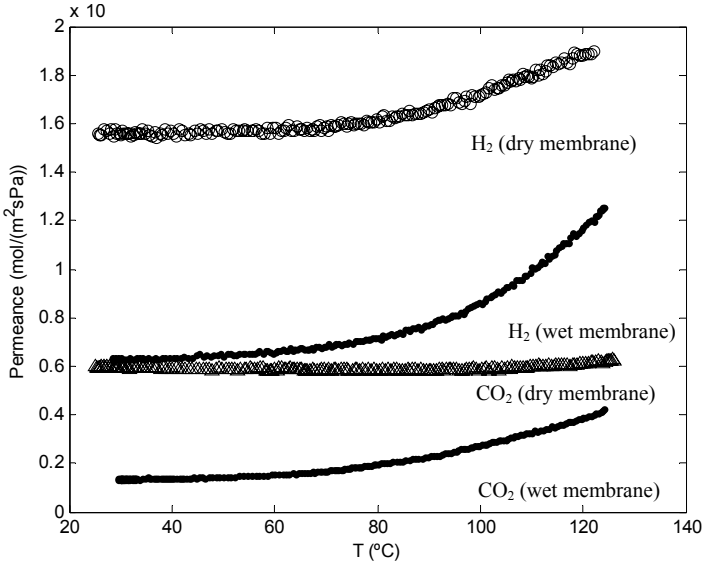

Figure VI.21 – Permeance of H_2 and CO_2 as function of temperature after AM-3-5 membrane humidification (same operating conditions as those of PTP runs in Figure VI.17); results obtained before humidification are also presented for comparison.

The dependence of ideal selectivities with temperature is illustrated in Figure VI.22. By comparison with values of Table VI.9, it is found that ideal selectivities for CO_2/O_2 and N_2/CO_2 are slightly higher and ideal selectivities for H_2/N_2 and H_2/CO_2 are inferior to those of the Knudsen diffusion. These results corroborate the presence of some defects in the membrane. However, given the higher selectivity values, they may be assumed to be present in less extent than for the previously studied membranes. Concerning the temperature effect, both N_2/CO_2, and CO_2/O_2 ideal selectivities decrease with temperature, since CO_2 permeance increases faster than that of N_2, and O_2 increases faster than that of CO_2. The ideal selectivity of H_2/CO_2 and H_2/N_2 show a relatively pronounced increasing trend with temperature, given the activated diffusion of H_2 through smaller AM-3 micropores.

The ideal selectivities for H_2/CO_2 before and after the membrane humidification are compared in Figure VI.22b. This figure clearly points out an expected enhancement in the ideal selectivity after humidification. However, such enhancement tends to vanish with increasing temperature, because of the removal of water molecules responsible for the blockage of some inter-crystalline pores.

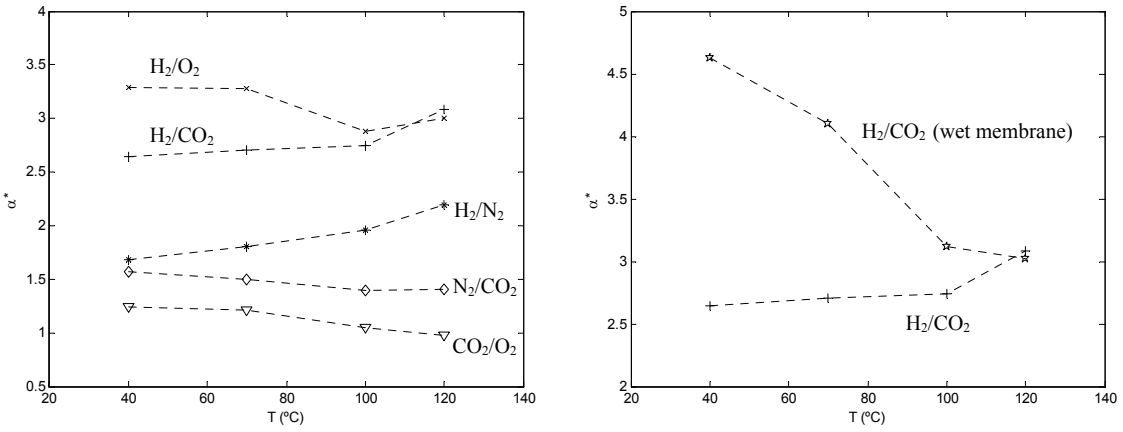

Figure VI.22 – Ideal selectivities for several binary systems in the AM-3-5 membrane as function of temperature.

It is important to note that although the permeations at programmed temperature evidence the better quality of the AM-3-5 membrane in comparison with AM-3-3 membrane, its permeances are around one order of magnitude superior, which could denunciate a higher density of large defects. Such disagreement may be attributed to differences of the thickness and pore size distributions. In order to roughly elucidate this feature, the ratios between the permeances of both membranes at 40ºC for H_2, N_2, and CO_2 were calculated. Assuming viscous or Knudsen flow, equations (III.2) and (III.6) show that this ratio reduces to $\Pi_{\text{AM–3–5}}/\Pi_{\text{AM–3–3}} = \delta_{\text{AM–3–3}}/\delta_{\text{AM–3–5}} \times \left(d_{\text{p,AM–3–5}}/d_{\text{p,AM–3–3}}\right)^{1-2}$, which for H_2, N_2, and CO_2 gives 14, 27, and 21, respectively. These values are close inside the same order of magnitude and so the higher permeances in AM-3-5 membrane may be ascribed essentially to its thinner thickness.

Similarly to the AM-3-3 membrane, the permeation data of Figure VI.17 were modelled based on the transport mechanisms discussed in Chapter III. Also for this membrane, surface diffusion was not taken into account. Figure VI.23 shows the good agreement found between modelling and experimental data, corresponding to $AARD = 2.5\%$.

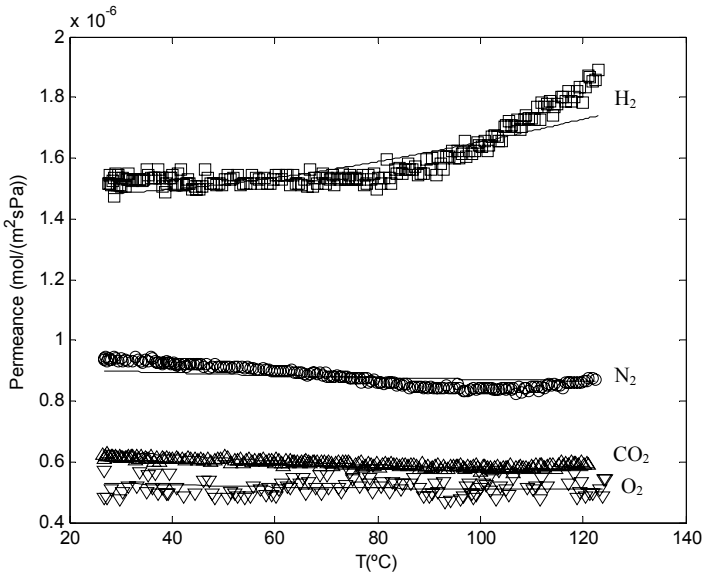

Figure VI.23 – Modelling and experimental results for permeation of H_2, N_2, O_2, and CO_2 in AM-3-5 membrane (ΔP = 0.2 bar).

The contributions of each individual transport mechanism for H_2 permeation, considering $\Pi_s = 0$, are illustrated in Figure VI.24. As for the previously discussed Figure VI.20, a predominance of a particular transport mechanism was not observed. In fact, Figure VI.24 evidences an identical contribution of Knudsen and viscous flow to the transport through defects. Besides, the activated gaseous diffusion is considerable for the total transport, being more important at higher temperatures, as expected.

Table VI.11 compiles the calculated model parameters. Also in this case, the activated diffusion parameter of molecules larger than AM-3 pore size, i.e. N_2, CO_2, and O_2, is one order of magnitude inferior to that of H_2 (4.916×10^{-6} *versus* 1.769×10^{-5}). Besides, they are significantly higher than those of the AM-3-3 membrane, corroborating the sound contribution of activated diffusion for transport through this membrane. This result is also consentaneous with the increasing trend of the $\Pi - T$ curves. Likewise AM-3-3 membrane, the activation energies found for the molecules larger than AM-3 pore size (3.0, 4.6, and 5.5 kJ/mol for N_2, CO_2, and O_2, respectively) are smaller than that of H_2 (10.0 kJ/mol), reflecting distinct diffusing pathways. Furthermore, the calculated activation energies are very close for both membranes.

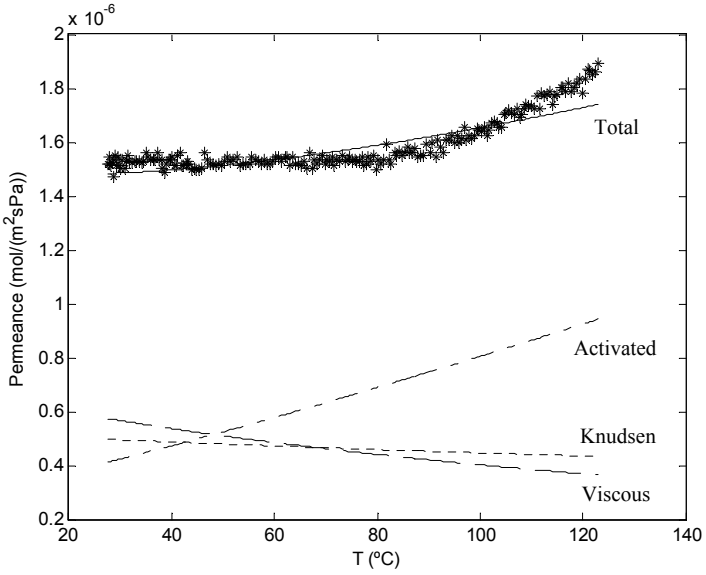

Figure VI.24 – Contribution of each transport mechanism for H_2 permeation in AM-3-5 membrane (ΔP = 0.2 bar).

Table VI.11 – Model parameters for H_2, N_2, CO_2, and O_2 diffusion in AM-3-5 membrane.

$g_{sup}\frac{\varepsilon d_p^2}{32\tau\delta\Re}$	$g_{sup}\frac{\varepsilon d_p}{3\tau\delta}\left(\frac{8}{\pi\Re}\right)^{0.5}$	$g_{sup}\frac{l_d}{Z\delta}\left(\frac{8}{\pi\Re}\right)^{0.5}$	$E_{a,g}$ (kJ/mol)			
(m mol K/J)	$(\text{mol K/J})^{0.5}$	$(\text{mol K/J})^{0.5}$	H_2	N_2	CO_2	O_2
1.285×10^{-14}	3.869×10^{-7}	4.916×10^{-6} (N_2, CO_2, O_2) 1.769×10^{-5} (H_2)	10.0	3.0	4.6	5.5

The obtained results point out a meaningful H_2 transport through AM-3-5 micropores and, accordingly, surface diffusion may be expected to occur, particularly at low temperatures. Hence, experimental data for H_2 were modelled taking this mechanism into account also (equation III.26). For this purpose, the parameters corresponding to the Knudsen and viscous mechanisms listed in Table VI.11 were fixed, while those for diffusion through micropores were fitted to the H_2 data. Figure VI.25 illustrates the model results together with the contributions of each mechanism. It is clear that the model performs quite better as confirmed by the smaller deviation obtained $(AARD = 1.1\%)$. Nonetheless, it should be noted that a higher number of parameters was fitted, which also

affords to the enhanced model results. The model parameters obtained are presented in Table VI.12. As may be noted, the activation energy for diffusion was ca. two times higher than that obtained assuming $\Pi_s = 0$ (21.6 and 10.0 kJ/mol, respectively). This is an expected result since a superior activation energy increases the permeation sensibility on the temperature, being able to interpret the visible acceleration of the curve after approximately 80ºC (see Figure VI.25).

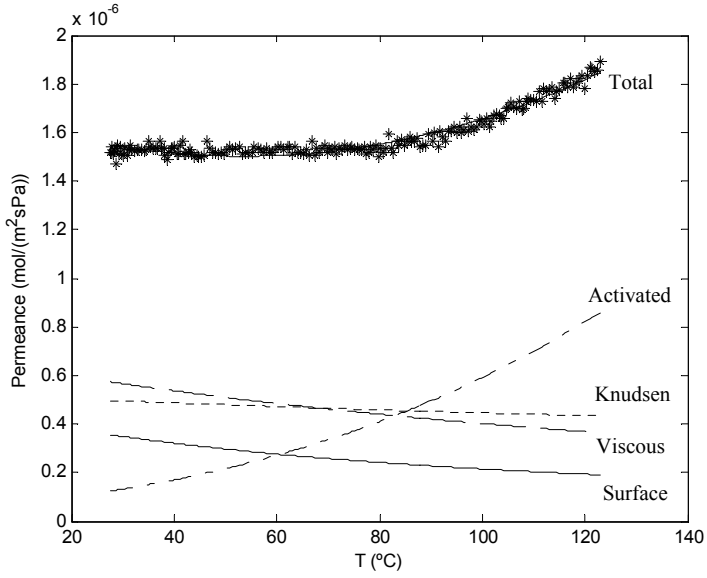

Figure VI.25 – Contribution of each transport mechanism for H_2 permeation in AM-3-5 membrane (ΔP = 0.2 bar).

Table VI.12 – Model parameters for H_2 diffusion in AM-3-5 membrane, after taking surface diffusion into account.

$g_{sup}\frac{\rho}{\delta}D_s^0 K_0$ $\left(kg/m^3 s^2\ Pa\right)$	$g_{sup}\frac{l_d}{Z\delta}\left(\frac{8}{\pi\Re}\right)^{0.5}$ $\left(mol\,K/J\right)^{0.5}$	$\Delta H_{ads} - E_{a,s}$ $\left(kJ/mol\right)$	$E_{a,g}$ $\left(kJ/mol\right)$
2.680×10^{-8}	5.349×10^{-4}	6.465×10^{3}	21.6

ZSM-5-1 Membrane

Figure VI.26 shows the fluxes of nitrogen and carbon dioxide in the ZSM-5-1 membrane as function of transmembrane pressure drop at 30ºC. Results correspond to one experimental run. The permeances of both gases at 30ºC and 100ºC are represented in Figure VI.27. In Figure VI.26, the flux of nitrogen depends linearly on ΔP $\left[N_i(\text{molm}^{-2}\text{s}^{-1}) = 5.211 \times \Delta P(\text{kPa})\right]$, which means the viscous flow mechanism is absent. Therefore, the membrane does not exhibit macropores or other rough defects. In fact, the permeation of non-adsorbable gases in micro and mesopores is directly proportional to ΔP. Such behavior is also evidenced in Figure VI.27a. The permeance of N_2 increases with temperature, which supports the activated nature of gaseous diffusion in small micropores. This result suggests that the transport is not controlled by Knudsen mechanism in mesopores, since in this case Π_{N_2} would decrease with increasing T.

In contrast to N_2, the flux of CO_2 deviates from previous behavior due to adsorption effects. As seen in Figure VI.26, the flux deviates clearly from the linear trend expected at low ΔP. Figure VI.27 corroborates this finding as the permeances of CO_2 vary with ΔP, a typical result for adsorbable gases. Such trend is more pronounced at lower temperatures, since adsorption decreases with increasing temperature. Furthermore, as ΔP is raised, Π_{CO_2} becomes nearly constant because the surface concentration tends toward saturation and the surface diffusion stabilizes. It is important to conclude that in this range of operation the surface diffusion is more significant than the activated gaseous diffusion, while Π_{CO_2} decreases with increasing temperature.

The calculated ideal selectivity, $\alpha^*_{\text{CO}_2/\text{N}_2}$, was plotted against ΔP at both temperatures in Figure VI.27b. $\alpha^*_{\text{CO}_2/\text{N}_2}$ decreases with transmembrane pressure drop because CO_2 permeance decreases whereas that of N_2 does not change significantly with pressure. Concerning the temperature effect, ideal selectivity shows the expected trend, i.e. it decreases with increasing temperature, since the adsorption load is reduced.

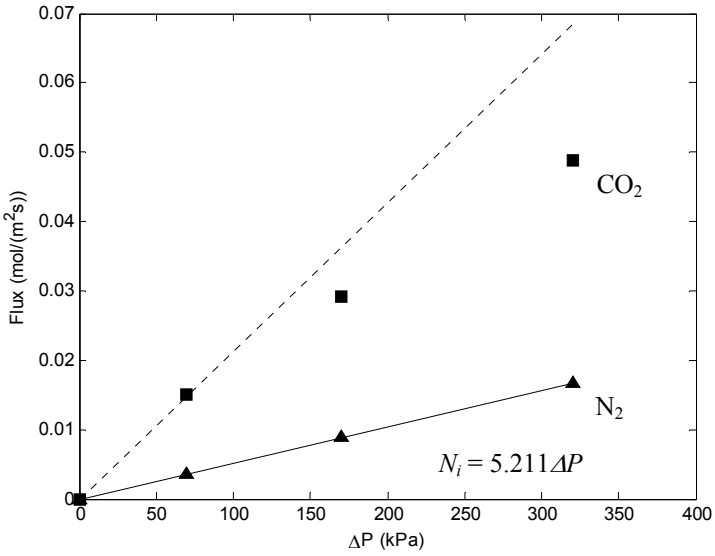

Figure VI.26 – Fluxes of pure N_2 and CO_2 in ZSM-5-1 membrane against transmembrane pressure drop at 30ºC. Symbols: Experimental data; Lines: – linear fitting; -- linear fitting at low pressure.

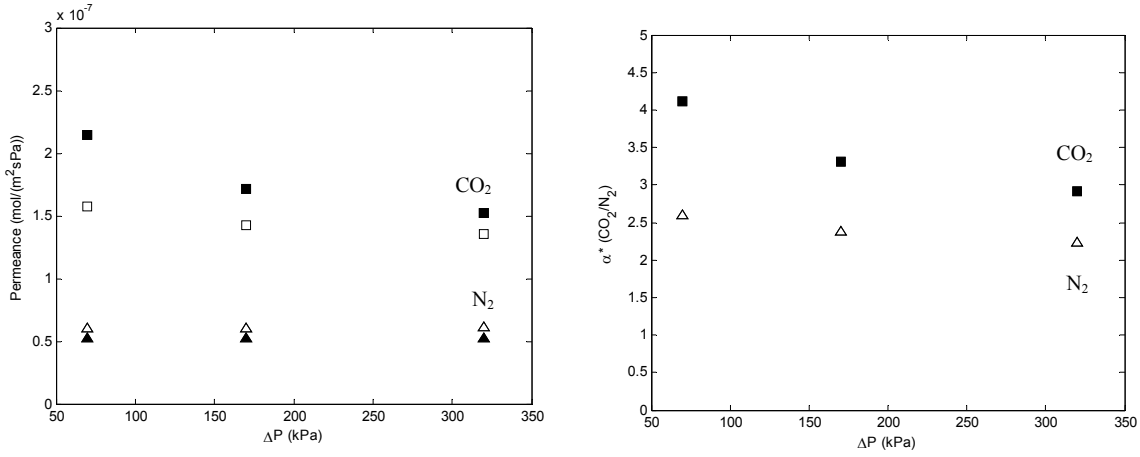

Figure VI.27 – Single permeances of N_2 and CO_2 and corresponding ideal selectivities in ZSM-5-1 membrane *versus* ΔP at 30ºC (close symbols) and 100ºC (open symbols).

2.2 Separation of binary mixtures

The performance of a membrane to separate a given binary mixture could be anticipated by knowing its quality. According to the previously discussed results for AM-3, ETS-10, 4A zeolite, and ZSM-5 membranes, a significant density of defects was found for most of them, which may give rise to non-selective transport. Nonetheless, the contribution of large

defects to permeation seems to be minor for both AM-3-3 and AM-3-5 membranes. Therefore, the separation of binary mixtures was carried out in this work using both AM-3-3 and AM-3-5 membranes.

Due to the large molecular diameters of N_2, CO_2, and O_2 relative to the pore size of AM-3 structure, the separation of these molecules from H_2-containing mixtures on AM-3 membranes is expected to occur based on molecular sieving. Accordingly, for such binary mixtures, high separation factors could be ideally predicted. However, due to the presence of macro and meso-defects, the desired sieving mechanism is weakened and selectivities diminish.

Permeation of equimolar binary mixtures of H_2/CO_2, N_2/CO_2 and H_2/N_2 were measured at three temperatures, while feed and sweep gas (helium) flow rates were fixed. Figure VI.28 shows the separation factors for both AM-3-3 and AM-3-5 membranes. They are around 1 and 1.6 and do not change significantly with temperature, except for H_2/CO_2/AM-3-5. These results are in accordance with the conclusions drawn from the pure gas permeation, being attributed to non-selective transport through large defects, which do not allow an efficient separation.

Concerning AM-3-3 membrane, the separation factors for N_2/CO_2 are quite similar to the corresponding ideal selectivity values (see Figure VI.12), while for H_2/CO_2 they are lower. Also for AM-3-5 membrane, the separation factors for H_2-containing mixtures were lower than ideal selectivities, whereas for N_2/CO_2 similar values were found. These results may be due to difficulties in the quantification of H_2 concentration, since H_2 and He (reference gas for TCD of the GC) have similar thermal conductivities (0.1706 and 0.1502 W/(m.K), respectively) and therefore the intensity of the TCD signal is very weak. The H_2 quantification is fundamental for the investigation of membranes capable to separate H_2-containing mixtures. Hence, our research team is presently trying to overcome such limitation.

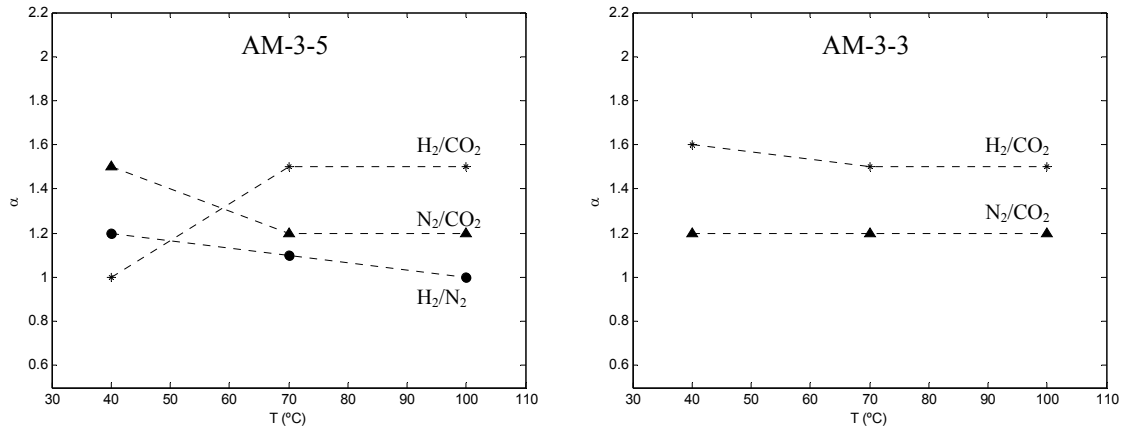

Figure VI.28 – Separation factors for AM-3-5 and AM-3-3 membranes as function of temperature. Values for equimolar mixtures and $\Delta P = 0$.

VII. Conclusions and Future Work

Conclusions

The dynamic characterization of zeolite membranes by gas permeation experiments is an indispensible tool for the complete assessment of their quality. After the structural characterization, these tests allow us to detect the existence of macro, meso and even microdefects in new synthesized membranes. After that, the preparation conditions may be continuously optimized to obtain good quality membranes. This has been the motivation for this dissertation.

In order to carry out permeation essays with pure gases and mixtures, an experimental set-up has been designed, assembled, and tested. With relation to pure gases, the main targets were the measurement of permeances at constant temperature, by varying the transmembrane pressure drop, and permeances at programmed temperature, by fixing the driving force. With respect to mixtures, the determination of the components mole fractions in the permeate and retentate demanded a GC which has been coupled later. In the whole, H_2, He, N_2, CO_2, and O_2 have been utilized.

In this work, nineteen membranes and three different supports have been studied, namely nine of AM-3, five of ETS-10, four of ZSM-5, and one of 4A-zeolite, and two supports of α-alumina, and one of stainless-steel. A first exploratory test with nitrogen at room temperature has detected fifteen membranes with rough defects, which induced us to perform a second deposition on six of them, and a third crystallization onto the two membranes. (The reference criterion for rejection was permeances higher than 10^{-6}

mol/m^{2}s.Pa). For instance, the ETS-10 membranes no. 4 and 5 reduced their permeances from 4.81×10^{-6} to less than 1×10^{-9}, and 7.10×10^{-6} to 2.26×10^{-8} mol/m^{2}s.Pa, respectively. On the contrary, AM-3-8, AM-3-9, and AM-3-10 membranes exhibited an apparently contradictory result, since Π values increased from 2.35×10^{-7} to 1.30×10^{-6}, 2.96×10^{-7} to 9.62×10^{-7}, and 1.22×10^{-6} to 6.38×10^{-6} mol/m^{2}s.Pa, respectively, attributed to the partial dissolution of the first formed titanosilicate layer, hindering a good intergrowth between neighbour crystals.

After the above mentioned essays, the most promising AM-3-3, AM-3-4, and AM-3-5 membranes were elected for further studies. The AM-3-4 membrane has been investigated with N_2 at different pressure drops at 25, 100 and 140ºC, but the results revealed it embodied a significant number of defects. Actually, the permeances at constant temperature increased with increasing ΔP, which denoted viscous flow through macropores.

The experimental observations registered for the AM-3-3 membrane with H_2, He, N_2, and CO_2 told that the prevailing transport mechanisms were viscous flow and Knudsen diffusion. The $\Pi - T$ curves were monotonously decreasing, which is typical of both contributions. Furthermore, the dominance of the Knudsen mechanism was verified by the linear trend found between permeances and the inverse of the square root of the molecular weight. Concerning the viscous flow contribution, its dependence on gas viscosity implies a subsequent relationship with kinetic diameter and molecular weight, which for Chapman-Enskog based equations is $\eta \propto M^{0.5}/d_k^2$. The measured permeances roughly followed $\Pi \propto d_k^2/M^{0.5}$, indicating some contribution from viscous flow, once Π_v is inversely proportional to viscosity.

The study of the AM-3-5 membrane with pure H_2, N_2, CO_2, and O_2 pointed out it contains not only macro and mesodefects, but also intercrystalline micropores. Actually, the constant permeances of N_2, CO_2, and O_2 over temperature must rely on the necessary existence of an activated diffusion to compensate the lowering viscous and Knudsen components. Since the kinetic diameters of N_2, CO_2, and O_2 are larger than the intracrystalline pores of AM-3, this proves the membrane have significant intercrystalline micropores. The hydrogen permeation exhibited the desired exponential behaviour with

temperature, since its small diameter superimposes the intracrystalline activated diffusion which overlaps the negative contribution of viscous and Knudsen fluxes. Modelling corroborated this phenomenological conclusion, showing that the last mechanisms were equivalent in magnitude and always descent, whereas the activated gaseous diffusion increased significantly with increasing temperature.

The ZSM-5 is known to adsorb CO_2. This fact gives rise to a distinct permeating behaviour, because the permeances decrease with increasing ΔP in view of the fact the surface loading concentrations increase non-linearly. These results were found for CO_2 in ZSM-5-1 membrane, whereas for N_2 a constant permeance was measured.

The calculated ideal selectivities, whose values ranged from ca. 1 to 4.2, have been computed with the individual permeances of the cited gases, allowing us to compare once more the AM-3-3 and AM-3-5 membranes. E.g., for the H_2/CO_2 pair, the AM-3-3 membrane gave α^* between 3.6 and 4.2 for 40–120 ºC, while for AM-3-5 $\alpha^* = 2.6\text{-}3.1$ in the same temperature interval. These results were expected in advance, since the predominance of the non-selective viscous flow in AM-3-5 penalizes the ideal separation factors.

With respect to the experimental selectivities of the H_2-containing mixtures studied, they were unfortunately lower than the ideal ones, which has been attributed to difficulties in the quantification of the H_2. This problem could not be fixed in the short time after the upgrade of the installation for multicomponent mixtures.

In order to increase the selectivities some essays have been carried out with AM-3-5 saturated with water. The measurements clearly emphasized an expected enhancement after humidification (e.g. from 2.6 to 4.6 for H_2/CO_2/AM-3-5), which vanished with increasing temperature, because of the removal of the water molecules responsible for the blockage of some pores.

In this work, modelling has been accomplished on the basis of the generalized Maxwell-Stefan (MS) equations, since it is simultaneously the most physically adequate and elegant approach to deal with multicomponent mixtures. In fact, new models have been derived in this thesis for gas transport across membranes and also for ion-exchange in

microporous zeolite materials. The second application arose naturally in parallel to the main focus of the dissertation, since the titanosilicates have been used in our group for the removal of toxic metals from aqueous solutions, making available interesting data to model.

The gas transport across porous membranes comprehends essentially five contributions: viscous, Knudsen, molecular, activated gaseous and surface diffusions. As has been mentioned above, the existence of macro and mesodefects in microporous materials denunciate the first two or three mechanisms. Interesting and desire contributions are the activated gaseous and surface diffusion. In this topic the knowledge of good multicomponent isotherms, whether predicted from pure models or experimentally measured, is an essential step. In this work, new expressions were derived for the intrinsic MS thermodynamic factors of mono and multicomponent Nitta, Langmuir-Freundlich, and Toth isotherms, in order to enlarge the application of the Maxwell-Stefan equations to the permeation of very dissimilar systems. In fact, the literature only presents equations for pure and binary classical and dual site Langmuir. The new expressions were validated using methane and ethane data from different sources for silicalite-1: equilibrium points for each gas in crystal, pure component fluxes through membrane, and binary fluxes also. From single isotherms, the multicomponent ones have been predicted; using pure permeation data the corresponding diffusion parameters have been optimized; finally, taking into account the Vignes relation, the crossed MS diffusivities have been computed. The new equations proposed here, together with previous parameters from independent experiments, have successfully allowed us to estimate the binary fluxes of methane/ethane through silicalite-1. It is clear from the procedure described that this validation is undoubtedly very stringent. The results obtained pointed out the new models are able to represent data for pure substances and predict binary permeation fairly well and reliably. In comparison with some better results reported for classical Langmuir, following an analogous approach, it should be emphasized our calculations involve four parameters less.

In relation to ion exchange, the MS approach has been adopted due to their well documented advantages over Nernst-Planck relationships, particularly because it takes account of ion-ion and ion-solid interactions. The new model proposed was validated with batch experiments on mercury (II) and cadmium (II) removal from aqueous solution using

ETS-4 microporous titanosilicate. The relevant species are Hg^{2+} or Cd^{2+} and Na^{+} (initially in solution and in ETS-4, respectively), and titanosilicate ionic fixed charges. Results obtained provide good representations of metal ions concentration in solution and solid phase along time. Even the transition from the steep descent to the horizontal branch of C_A/C_{A0} *versus* time curves are well represented, precisely where kinetic curves are most difficult to fit. The predicting ability of our MS based model has been also analyzed, being possible to conclude it performs very well. In effect, good predictions are accomplished with parameters optimized from independent sets of data. Such performance may be attributed to the sound physical principles of Maxwell-Stefan theory.

Future Work

Some suggestions for future work may be raised. It is important to measure isotherms for pure gases and mixtures on titanosilicates due to their importance in the permeation phenomenon. After that, one may predict them by molecular simulations and compare calculations with experimental data. With respect to the experimental work, it is important to study the permeation of additional gases and mixtures as for instance H_2/CH_4 due to its importance. It is crucial to fix the problem of the quantification of hydrogen in the mixtures. Only that will make viable an extension of the experimental programme to wider ranges of operating conditions. As for equilibrium, the prediction of permeances of pure and mixed gases may be accomplished by molecular dynamics simulations, in order to reduce the experimental work load and avoid contact with dangerous molecules. Finally, it is important to test the performance of the proposed MS based model for multicomponent ion exchange, and analyze its behaviour for concentrated solutions, where the Nernst-Planck model is expected to fail.

VIII. References

Abdul-Rehman, H. B., Hasanain, M. A. and Loughlin, K. F. (1990). *Quaternary, ternary, binary, and pure component sorption on zeolites. 1. Light alkanes on linde S-115 silicalite at moderate to high pressures.* Industrial & Engineering Chemistry Research **29**(7), 1525-1535.

Adams, T. M. and Mickalonis, J. (2007). *Hydrogen permeability of multiphase V-Ti-Ni metallic membranes.* Materials Letters **61**(3), 817-820.

Ahmed, I. A. M., Young, S. D. and Crout, N. M. J. (2006). *Time-dependent sorption of Cd^{2+} on CaX zeolite: Experimental observations and model predictions.* Geochimica Et Cosmochimica Acta **70**(19), 4850-4861.

Akamatsu, K., Ohta, Y., Sugawara, T., Kanno, N., Tonokura, K., Hattori, T. and Nakao, S. (2009). *Stable high-purity hydrogen production by dehydrogenation of cyclohexane using a membrane reactor with neither carrier gas nor sweep gas.* Journal of Membrane Science **330**(1-2), 1-4.

Aksu, Z. (2005). *Application of biosorption for the removal of organic pollutants: A review.* Process Biochemistry **40**(3-4), 997-1026.

Aoki, K., Kusakabe, K. and Morooka, S. (1998). *Gas permeation properties of A-type zeolite membrane formed on porous substrate by hydrothermal synthesis.* Journal of Membrane Science **141**(2), 197-205.

Armenante, P. M. and Kirwan, D. J. (1989). *Mass-transfer to microparticles in agitated systems.* Chemical Engineering Science **44**(12), 2781-2796.

Bakker, W. J. W., Kapteijn, F., Poppe, J. and Moulijn, J. A. (1996). *Permeation characteristics of a metal-supported silicalite-1 zeolite membrane.* Journal of Membrane Science **117**(1-2), 57-78.

Bakker, W. J. W., vandenBroeke, L. J. P., Kapteijn, F. and Moulijn, J. A. (1997). *Temperature dependence of one-component permeation through a silicalite-1 membrane.* AIChE Journal **43**(9), 2203-2214.

Barrer, R. M. (1978). Zeolites and Clay Minerals as Sorbents and Molecular

Sieves. New York, Wiley.

Barrer, R. M. and Rees, L. V. (1960). *Self-diffusion of alkali metal ions in analcite.* Transactions of the Faraday Society **56**(5), 709-721.

Bernal, M. P. (2002). Nuevos métodos de preparacíon y caracterizacíon de membranas zeoliticas tipo MFI. Aplicacíon a processos de separacíon y reaccíon/separacíon. *Departamente de Ingeniería Química y Tecnologias des Medio Ambiente*. Zaragoza, Universidad de Zaragoza.

Bernal, M. P., Coronas, J., Menendez, M. and Santamaria, J. (2002). *Characterization of zeolite membranes by temperature programmed permeation and step desorption.* Journal of Membrane Science **195**(1), 125-138.

Bernardo, P., Drioli, E. and Golemme, G. (2009). *Membrane gas separation: A review/state of the art.* Industrial & Engineering Chemistry Research **48**(10), 4638-4663.

Bhattacharya, A. (2007). *Predicting rates of dissolution of polydisperse solids in reactive media.* Chemical Engineering and Processing **46**(6), 573-583.

Biskup, B. and Subotic, B. (2004). *Kinetic analysis of the exchange processes between sodium ions from zeolite A and cadmium, copper and nickel ions from solutions.* Separation and Purification Technology **37**(1), 17-31.

Bitter, J. G. A. (1991). Transport mechanisms in membrane separation processes. New York, Plenum Press.

Bortun, A. I., Bortun, L. N. and Clearfield, A. (1997). *Evaluation of synthetic inorganic ion exchangers for cesium and strontium removal from contaminated groundwater and wastewater.* Solvent Extraction and Ion Exchange **15**(5), 909-929.

Braunbarth, C. M., Boudreau, L. C. and Tsapatsis, M. (2000). *Synthesis of ETS-4/TiO_2 composite membranes and their pervaporation performance.* Journal of Membrane Science **174**(1), 31-42.

Breck, D. W. (1974). Zeolite molecular sieves. New York, John Wiley & Sons.

Brooke, N. M. and Rees, L. V. C. (1969). *Kinetics of ion-exchange .2.* Transactions of the Faraday Society **65**(562P), 2728-2739.

Burggraaf, A. J. (1999). *Single gas permeation of thin zeolite (MFI) membranes: Theory and analysis of experimental observations.* Journal of Membrane Science **155**(1), 45-65.

Burggraaf, A. J. and Cot, L. (1996). Fundamentals of inorganic membranes science and technology. Amsterdam, The Netherlands, Elsevier.

Burggraaf, A. J., Vroon, Z. A. E. P., Keizer, K. and Verweij, H. (1998). *Permeation of single gases in thin zeolite MFI membranes.* Journal of Membrane Science **144**(1-2), 77-86.

Buss, E. and Heuchel, M. (1997). *Adsorption equilibria of methane and tetrafluoromethane and their binary mixtures on silicalite.* Journal of the Chemical Society-Faraday Transactions **93**(8), 1621-1628.

Camarinha, E. D., Lito, P. F., Antunes, B. M., Otero, M., Lin, Z., Rocha, J., Pereira, E., Duarte, A. C. and Silva, C. M. (2009). *Cadmium(II) removal from aqueous solution using microporous titanosilicate ETS-10.* Chemical Engineering Journal **155**(1-2), 108-114.

Caro, J. and Noack, M. (2008). *Zeolite membranes - Recent developments and progress.* Microporous and Mesoporous Materials **115**(3), 215-233.

Caro, J., Noack, M. and Kolsch, P. (2005). *Zeolite membranes: From the laboratory scale to technical applications.* Adsorption-Journal of the International Adsorption Society **11**(3-4), 215-227.

Caro, J., Noack, M., Kolsch, P. and Schafer, R. (2000). *Zeolite membranes - State of their development and perspective.* Microporous and Mesoporous Materials **38**(1), 3-24.

Chanda, M. and Rempel, G. L. (1995). *Sorption of sulfide on a macroporous, quaternized poly(4-vinyl pyridine) in alkaline medium.* Reactive Polymers **24**(3), 203-212.

Chao, P. Y., Chuang, Y. Y., Ho, G. H., Chuang, S. H., Tsai, T. C., Lee, C. Y., Tsai, S. T. and Huang, J. F. (2008). *Study of molecular-shape selectivity of zeolites by gas chromatography.* Journal of Chemical Education **85**(11), 1558-1561.

Chiron, N., Guilet, R. and Deydier, E. (2003). *Adsorption of Cu(II) and Pb(II) onto a grafted silica: isotherms and kinetic models.* Water Research **37**(13), 3079-3086.

Choi, J. H., Kim, S. D., Kwon, Y. J. and Kim, W. J. (2006). *Adsorption behaviors of ETS-10 and its variant, ETAS-10 on the removal of heavy metals, Cu^{2+}, Co^{2+}, Mn^{2+} and Zn^{2+} from a waste water.* Microporous and Mesoporous Materials **96**(1-3), 157-167.

Chung, T. H., Lee, L. L. and Starling, K. E. (1984). *Applications of kinetic gas theories and multiparameter correlation for prediction of dilute gas viscosity and thermal-conductivity.* Industrial & Engineering Chemistry Fundamentals **23**(1), 8-13.

Cincotti, A., Mameli, A., Locci, A. M., Orru, R. and Cao, G. (2006). *Heavy metals uptake by Sardinian natural zeolites: Experiment and modeling.* Industrial & Engineering Chemistry Research **45**(3), 1074-1084.

Coker, E. N. and Rees, L. V. C. (1992). *Ion-exchange in beryllophosphate-G .1. Ion-exchange equilibria.* Journal of the Chemical Society-Faraday Transactions **88**(2), 273-276.

Coker, E. N. and Rees, L. V. C. (2005). *Kinetics of ion exchange in quasi-crystalline aluminosilicate zeolite precursors.* Microporous and Mesoporous Materials **84**(1-3), 171-178.

Coronas, J., Falconer, J. L. and Noble, R. D. (1997). *Characterization and permeation properties of ZSM-5 tubular membranes.* AIChE Journal **43**(7), 1797-1812.

Coronas, J. and Santamaria, J. (1999). *Separations using zeolite membranes.* Separation and Purification Methods **28**(2), 127-177.

Crespo, J. P. and Carrondo, M. (1993). Integration of fermentation and membrane processes. *Membrane Processes in Separation and Purification.* J. P. Crespo and Boddeker. Netherlands, Kluwer Academic Publishers. **272**.

Dabrowski, A., Hubicki, Z., Podkoscielny, P. and Robens, E. (2004). *Selective removal of the heavy metal ions from waters and industrial wastewaters by ion-exchange method.* Chemosphere **56**(2), 91-106.

Decaillon, J. G., Andres, Y., Mokili, B. M., Abbe, J. C., Tournoux, M. and Patarin, J. (2002). *Study of the ion exchange selectivity of layered titanosilicate $Na_3(Na,H)Ti_2O_2[Si_2O_6]_2.2H_2O$, AM-4, for strontium.* Solvent Extraction and Ion Exchange **20**(2), 273-291.

Do, D. D. (1998). Adsorption analysis: Equilibria and kinetics. Singapore, Imperial College Press.

Dolgonosov, A. M., Khamizov, R. K., Krachak, A. N. and Prudkovsky, A. G. (1995). *Macroscopic model for multispecies ion-exchange kinetics.* Reactive & Functional Polymers **28**(1), 13-20.

Dong, J. H., Lin, Y. S. and Liu, W. (2000). *Multicomponent hydrogen/hydrocarbon separation by MFI-type zeolite membranes.* AIChE Journal **46**(10), 1957-1966.

Fang, S. M., Bi, L., Wu, X. S., Gao, H. Y., Chen, C. S. and Liu, W. (2008). *Chemical stability and hydrogen permeation performance of Ni-$BaZr_{0.1}Ce_{0.7}Y_{0.2}O_{3-\delta}$ in an H_2S-containing atmosphere.* Journal of Power Sources **183**(1), 126-132.

Fernandez, M. A. and Carta, G. (1996). *Characterization of protein adsorption by composite silica-polyacrylamide gel anion exchangers .1. Equilibrium and mass transfer in agitated contactors.* Journal of Chromatography A **746**(2), 169-183.

Ferreira, T. R., Lopes, C. B., Lito, P. F., Otero, M., Lin, Z., Rocha, J., Pereira, E., Silva, C. M. and Duarte, A. (2009). *Cadmium(II) removal from aqueous solution using microporous titanosilicate ETS-4.* Chemical Engineering Journal **147**(2-3), 173-179.

Fick, A. (1855a). *On liquid diffusion.* Philosophical Magazine Series 4 **10**, 30-39.

Fick, A. (1855b). *Uber diffusion.* Poggendorff's Annalen der Physik und Chemie **94**, 59-86.

Freemantle, M. (2005). *Membranes for gas separation.* Chemical & Engineering News **83**(40), 49-57.

Gardner, T. Q., Flores, A. I., Noble, R. D. and Falconer, J. L. (2002). *Transient measurements of adsorption and diffusion in H-ZSM-5 membranes.* AIChE Journal **48**(6), 1155-1167.

Gavalas, G. R. (2008). *Diffusion in microporous membranes: Measurements and modeling.* Industrial & Engineering Chemistry Research **47**(16), 5797-5811.

Gebremedhin-Haile, T., Olguin, M. T. and Solache-Rios, M. (2003). *Removal of mercury ions from mixed aqueous metal solutions by natural and modified zeolitic minerals.* Water Air and Soil Pollution **148**(1-4), 179-200.

Gilliland, E. R., Baddour, R. F., Perkinso.Gp and Sladek, K. J. (1974). *Diffusion on surfaces .1. Effect of concentration on diffusivity of physically adsorbed gases.* Industrial & Engineering Chemistry Fundamentals **13**(2), 95-100.

Gilliland, E. R., Baddour, R. F. and Russell, J. L. (1958). *Rates of flow through microporous solids.* AIChE Journal **4**(1), 90-96.

Graham, E. E. and Dranoff, J. S. (1982a). *Application of the Stefan-Maxwell equations to diffusion in ion-exchangers .1. Theory.* Industrial & Engineering Chemistry Fundamentals **21**(4), 360-365.

Graham, E. E. and Dranoff, J. S. (1982b). *Application of the Stefan-Maxwell equations to diffusion in ion-exchangers .2. Experimental results.* Industrial & Engineering Chemistry Fundamentals **21**(4), 365-369.

Guan, G. Q., Kusakabe, K. and Morooka, S. (2001). *Synthesis and permeation properties of ion-exchanged ETS-4 tubular membranes.* Microporous and Mesoporous Materials **50**(2-3), 109-120.

Guan, G. Q., Kusakabe, K. and Morooka, S. (2002). *Separation of nitrogen from oxygen using a titanosilicate membrane prepared on a porous α-alumina support tube.* Separation Science and Technology **37**(5), 1031-1039.

Guisnet, M. and Giilson, J.-P. (2002). Zeolites for cleaner technologies. London, Imperial College Press.

Gump, C. J., Lin, X., Falconer, J. L. and Noble, R. D. (2000). *Experimental configuration and adsorption effects on the permeation of C-4 isomers through ZSM-5 zeolite membranes.* Journal of Membrane Science **173**(1), 35-52.

Haase, R. (1969). Thermodynamics of irreversible processes. New York, Dover Publications, Inc.

Helfferich, F. (1995). Ion exchange. New York, Dover.

HFPeurope. (2009). *http://www.HFPeurope.org*

Ho, W. S. W. and Sirkar, K. K. (1992). Membrane handbook. London, Kluwer Academic Publishers.

Ho, Y. S. and McKay, G. (1999a). *Pseudo-second order model for sorption processes.* Process Biochemistry **34**(5), 451-465.

Ho, Y. S. and McKay, G. (1999b). *The sorption of lead(II) ions on peat.* Water Research **33**(2), 578-584.

Hogendoorn, J. A., Veen, A. J. V. d., Stegen, J. H. G. V. d., Kuipers, J. A. M. and Versteeg, G. F. (2001). *Application of the Maxwell-Stefan theory to the membrane electrolysis process: model development and simulation.* Computers and Chemical Engineering **25**, 1251-1265.

Hsieh, H. P. (1996). Inorganic membranes for separation and reaction. Netherlands, Elsevier.

Inglezakis, V. J., Loizidou, M. D. and Grigoropoulou, H. P. (2002). *Equilibrium and kinetic ion exchange studies of Pb^{2+}, Cr^{3+}, Fe^{3+} and Cu^{2+} on natural clinoptilolite.* Water Research **36**(11), 2784-2792.

Jackson, R. (1977). Transport in porous catalysts. Amsterdam, Elsevier.

Jaroniec, M. (1984). Physical Adsorption on Heterogeneous Solids. *Fundamentals of Adsorption.* A. L. Myers, Belfort, G. New York, Engineering Foundation, 239-248.

Jeong, H. K., Krohn, J., Sujaoti, K. and Tsapatsis, M. (2002). *Oriented molecular sieve membranes by heteroepitaxial growth.* Journal of the American Chemical Society **124**(44), 12966-12968.

Kapteijn, F., Moulijn, J. A. and Krishna, R. (2000a). *The generalized Maxwell-Stefan model for diffusion in zeolites: Sorbate molecules with different saturation loadings.* Chemical Engineering Science **55**(15), 2923-2930.

Kapteijn, F., van de Graaf, J. M. and Moulijn, J. A. (2000b). *One-component permeation maximum: Diagnostic tool for silicalite-1 membranes?* AIChE Journal **46**(5), 1096-1100.

Kita, H., Li, X., Nagamatsu, T. and Tanaka, K. (2007). *Synthesis of long-term acid-stable zeolite membranes and their application to esterification reactions*. Fourth International Zeolite Membrane Meeting, Zaragoza, Spain.

Knudsen, M. (1909). *Die gesetze der molekularströmung und der inneren reibungsströmung der gase durch röhren.* Annalen der Physik (Leipzig) **28**, 75-130.

Koros, W. J. (1995). *Membranes: Learning a lesson from nature.* Chemical Engineering Progress **91**(10), 68-81.

Koros, W. J. (2004). *Evotving beyond the thermat age of separation processes: Membranes can lead the way.* AIChE Journal **50**(10), 2326-2334.

Koudsi, U. Y. and Dyer, A. (2001). *Sorption of Co-60 on a synthetic titanosilicate analogue of the mineral penkvilksite-20 and antimonysilicate.* Journal of Radioanalytical and Nuclear Chemistry **247**(1), 209-219.

Kraaijeveld, G., Sumberova, V., Kuindersma, S. and Wesselingh, H. (1995). *Modeling electrodialysis using the Maxwell-Stefan description.* Chemical Engineering Journal and the Biochemical Engineering Journal **57**(2), 163-176.

Krishna, R. (1990). *Multicomponent surface-diffusion of adsorbed species - A description based on the generalized Maxwell-Stefan equations.* Chemical Engineering Science **45**(7), 1779-1791.

Krishna, R. (1993). *Problems and pitfalls in the use of the Fick formulation for intraparticle diffusion.* Chemical Engineering Science **48**(5), 845-861.

Krishna, R. (2009). *Describing the diffusion of guest molecules inside porous structures.* Journal of Physical Chemistry C **113**, 19756-19781.

Krishna, R. and Baur, R. (2003). *Modelling issues in zeolite based separation processes.* Separation and Purification Technology **33**(3), 213-254.

Krishna, R. and Baur, R. (2004). *Analytical solution of the Maxwell-Stefan equations for multicomponent permeation across a zeolite membrane.* Chemical Engineering Journal **97**, 37-45.

Krishna, R. and Paschek, D. (2000). *Separation of hydrocarbon mixtures using zeolite membranes: A modelling approach combining molecular simulations with the Maxwell-Stefan theory.* Separation and Purification Technology **21**(1-2), 111-136.

Krishna, R. and Paschek, D. (2002). *Verification of the Maxwell-Stefan theory for diffusion of three-component mixtures in zeolites.* Chemical Engineering Journal **87**, 1-9.

Krishna, R., Paschek, D. and Baur, R. (2004). *Modeling the occupancy dependence of diffusivities in zeolites.* Microporous and Mesoporous Materials **76**(1-3), 233-246.

Krishna, R., Smit, B. and Vlugt, T. J. H. (1998). *Sorption-induced diffusion-selective separation of hydrocarbon isomers using silicalite.* Journal of Physical Chemistry A **102**(40), 7727-7730.

Krishna, R. and Wesselingh, J. A. (1997). *Review article number 50 - The Maxwell-Stefan approach to mass transfer.* Chemical Engineering Science **52**(6), 861-911.

Kulov, N. N., Nikolaishvili, E. K., Barabash, V. M., Braginski, L. N., Malyusov, V. A. and Zhavoronkov, N. M. (1983). *Dissolution of solid particles suspended in agitated vessels.* Chemical Engineering Communications **21**(4-6), 259-271.

Kuznicki, S. M. (1989). Large-pored crystalline titanium molecular sieve zeolites USA, Engelhard Corporation (Edison, NJ). **4853202**

Lagergren, S. (1898). *About the theory of so-called adsorption of soluble substances* Kungliga Svenska Vetenskapsakademiens. Handlingar **24**, 1-39.

Lamia, N., Granato, M. A., Gomes, P. S. A., Grande, C. A., Wolff, L., Leflaive, P., Leinekugel-le-Cocq, D. and Rodrigues, A. E. (2009). *Propane/propylene separation by simulated moving bed II. Measurement and prediction of binary adsorption equilibria of propane, propylene, isobutane, and 1-butene on 13X zeolite.* Separation Science and Technology **44**(7), 1485-1509.

Lawton, W. H. and Sylvestre, E. A. (1971). *Elimination of linear parameters in nonlinear regression.* Technometrics **13**(3), 461-481.

Levan, M. D. and Vermeulen, T. (1981). *Binary Langmuir and Freundlich Isotherms for Ideal Adsorbed Solutions.* Journal of Physical Chemistry **85**(22), 3247-3250.

Li, S. G., Falconer, J. L., Noble, R. D. and Krishna, R. (2007). *Modeling permeation of CO2/CH4, CO2/N-2, and N-2/CH4 mixtures across SAPO-34 membrane with the maxwell-stefan equations.* Industrial & Engineering Chemistry Research **46**(12), 3904-3911.

Liberti, L., Boari, G. and Passino, R. (1978). *Chloride-sulfate exchange on anion resins - Kinetic investigations .2. Particle diffusion rates.* Desalination **25**(2), 123-134.

Lin, Z., Rainho, J. P., Rocha, J. and Carlos, L. D. (2006). *Preparation of photoluminescent materials from a lanthanide-doped microporous titanosilicate precursor.* Advanced Materials Forum Iii, Pts 1 and 2 **514-516**, 123-127.

Lin, Z., Rocha, J., Brandao, P., Ferreira, A., Esculcas, A. P., deJesus, J. D. P., Philippou, A. and Anderson, M. W. (1997). *Synthesis and structural characterization of microporous umbite, penkvilksite, and other titanosilicates.* Journal of Physical Chemistry B **101**(36), 7114-7120.

Lin, Z., Rocha, J., Navajas, A., Tellez, C., Coronas, J. Q. and Santamaria, J. (2004). *Synthesis and characterisation of titanosilicate ETS-10 membranes.* Microporous and Mesoporous Materials **67**(1), 79-86.

Liu, Y. L., Du, H. B., Xu, Y. H., Ding, H., Pang, W. Q. and Yue, Y. (1999). *Synthesis and characterization of a novel microporous titanosilicate with a structure of penkvilksite-1M.* Microporous and Mesoporous Materials **28**(3), 511-517.

Liu, Y. L., Du, H. B., Zhou, F. Q. and Pang, W. Q. (1997). *Synthesis of a new titanosilicate: an analogue of the mineral penkvilksite.* Chemical Communications(15), 1467-1468.

Lopes, C. B., Otero, M., Coimbra, J., Pereira, E., Rocha, J., Lin, Z. and Duarte, A. (2007). *Removal of low concentration Hg^{2+} from natural waters by microporous and layered titanosilicates.* Microporous and Mesoporous Materials **103**(1-3), 325-332.

Lopes, C. B., Otero, M., Lin, Z., Silva, C. M., Rocha, J., Pereira, E. and Duarte, A. C. (2009). *Removal of Hg^{2+} ions from aqueous solution by ETS-4 microporous titanosilicate - Kinetic and equilibrium studies.* Chemical Engineering Journal **151**(1-3), 247-254.

Lv, L., Wang, K. and Zhao, X. S. (2007). *Effect of operating conditions on the removal of Pb^{2+} by microporous titanosilicate ETS-10 in a fixed-bed column.* Journal of Colloid and Interface Science **305**(2), 218-225.

Manson, E. A. and del Castillo, L. F. (1985). *The role of viscous flow in theories of membrane transport.* Journal of Membrane Science **23**, 199-220.

Manson, E. A. and Lonsdale, H. K. (1990). *Statistical mechanical theory of membrane transport.* Journal of Membrane Science **51**, 1-81.

Mathews, A. P. and Weber, W. J. (1980). *Mathematical-Modeling of Adsorption in Multicomponent Systems.* Abstracts of Papers of the American Chemical Society **180**(Aug), 7-Inde.

Merkel, T. C., Freeman, B. D., Spontak, R. J., He, Z., Pinnau, I., Meakin, P. and Hill, A. J. (2002). *Ultrapermeable, reverse-selective nanocomposite membranes.* Science **296**(5567), 519-522.

Miller, S. A., Amber, C. M., Bennet, R. C., Dahlstrom, D. A., Darji, J. D., Emmet, R. C., Gray, J. B., Gurnham, C. F., Jacobs, L. J., Klepper, R. P., Michalson, A. W., Oldshue, J. Y., Silverblatt, C. E., Smith, J. C. and Todd, D. B. (1984). Liquid-solid systems. *Perry's Chemical Engineers' handbook.* R. H. Perry and D. Green. Singapore, McGrow-Hill.

Misic, D. M., Sudo, Y., Suzuki, M. and Kawazoe, K. (1982). *Liquid-to-particle mass-transfer in a stirred batch adsorption tank with non-linear isotherm.* Journal of Chemical Engineering of Japan **15**(1), 67-70.

Mulder, M. (1997). Basic principles of membrane tecnology. Dordrecht, The Netherlands, Kluwer Academic Publishers.

Myers, A. L. and Prausnitz, J. M. (1965). *Thermodynamics of mixed gas adsorption.* AIChE Journal **11**, 121-130.

Namasivayam, C. and Senthilkumar, S. (1998). *Removal of arsenic(V) from aqueous solution using industrial solid waste: Adsorption rates and equilibrium studies.* Industrial & Engineering Chemistry Research **37**(12), 4816-4822.

Nishiyama, N., Gora, L., Teplyakov, V., Kapteijn, F. and Moulijn, J. A. (2001). *Evaluation of reproducible high flux silicalite-1 membranes: Gas permeation and separation characterization.* Separation and Purification Technology **22-23**, 295-307.

Nitta, T., Shigetomi, T., Kurooka, M. and Katayama, T. (1984). *An Adsorption-Isotherm of Multi-Site Occupancy Model for Homogeneous Surface.* Journal of Chemical Engineering of Japan **17**(1), 39-45.

Okamoto, K., Fujii, M., Okamyo, S., Suzuki, H., Tanaka, K. and Kita, H. (1995). *Gas permeation properties of poly(ether imide) segmented copolymers.* Macromolecules **28**(20), 6950-6956.

Okazaki, M., Tamon, H. and Toel, R. (1981). *Interpretation of surface flow phenomenon of adsorbed gases by hopping model.* AIChE Journal **27**(2), 262-270.

Pakizeh, M., Omidkhah, M. R. and Zarringhalam, A. (2007). *Study of mass transfer through new templated silica membranes prepared by sol-gel method.* International Journal of Hydrogen Energy **32**(12), 2032-2042.

Paschek, D. and Krishna, R. (2000). *Monte Carlo simulations of self- and transport-diffusivities of 2-methylhexane in silicalite.* Physical Chemistry Chemical Physics **2**(10), 2389-2394.

Patzay, G. (1995). *A simplified numerical solution method for the Nernst-Planck multicomponent ion exchange kinetics model.* Reactive & Functional Polymers **27**(1), 83-89.

Pavel, C. C., Popa, K., Bilba, N., Cecal, A., Cozma, D. and Pui, A. (2003). *The sorption of some radiocations on microporous titanosilicate ETS-10.* Journal of Radioanalytical and Nuclear Chemistry **258**(2), 243-248.

Pavel, C. C., Vuono, D., Catanzaro, O. L., De Luca, P., Bilba, N., Nastro, A. and Nagy, J. B. (2002). *Synthesis and characterization of the microporous titanosilicates ETS-4 and ETS-10.* Microporous and Mesoporous Materials **56**(2), 227-239.

Pinto, N. G. and Graham, E. E. (1987). *Characterization of ionic diffusivities in ion-exchange resins.* Industrial & Engineering Chemistry Research **26**(11), 2331-2336.

Poshusta, J. C., Tuan, V. A., Falconer, J. L. and Noble, R. D. (1998). *Synthesis and permeation properties of SAPO-34 tubular membranes.* Industrial & Engineering Chemistry Research **37**(10), 3924-3929.

Powell, C. E. and Qiao, G. G. (2006). *Polymeric CO_2/N_2 gas separation membranes for the capture of carbon dioxide from power plant flue gases.* Journal of Membrane Science **279**(1-2), 1-49.

Rand, D. A. J. and Dell, R. M. (2008). Hydrogen energy – Challenges and prospects. Cambridge, RSC Publishing.

Rautenbach, R. and Albrecht, R. (1989). Membrane process. Aachen, West Germany, John Wiley & Sons.

Reddad, Z., Gerente, C., Andres, Y. and Le Cloirec, P. (2002). *Adsorption of several metal ions onto a low-cost biosorbent: Kinetic and equilibrium studies.* Environmental Science & Technology **36**(9), 2067-2073.

Rees, L. V. C., Bruckner, P. and Hampson, J. (1991). *Sorption of N2, CH4 and CO2 in silicalite-1.* Gas Separation and Purification Technology **5**, 67-75.

Rocha, J. and Anderson, M. W. (2000). *Microporous titanosilicates and other novel mixed octahedral-tetrahedral framework oxides.* European Journal of Inorganic Chemistry(5), 801-818.

Rodriguez, J. F., de Lucas, A., Leal, J. R. and Valverde, J. L. (2002). *Determination of intraparticle diffusivities of Na^+/K^+ in water and water/alcohol mixed solvents on a strong acid cation exchanger.* Industrial & Engineering Chemistry Research **41**(12), 3019-3027.

Rodriguez, J. F., Valverde, J. L. and Rodrigues, A. E. (1998). *Measurements of effective self-diffusion coefficients in a gel-type cation exchanger by the zero-length-column method.* Industrial & Engineering Chemistry Research **37**(5), 2020-2028.

Romero, J., Gijiu, C., Sanchez, J. and Rios, G. M. (2004). *Unified approach of gas, liquid and supercritical solvent transport through microporous membranes.* Chemical Engineering Science **59**(7), 1569-1576.

Ruthven, D. M. (1984). Principles of adsorption and adsorption processes. New York, Wiley.

Samson, E. and Marchand, J. (1999). *Numerical solution of the extended Nernst-Planck model.* Journal of Colloid and Interface Science **215**(1), 1-8.

Schiesser, W. E. (1991). The numerical method of lines. USA, Academic Press.

Sebastian, V., Lin, Z., Rocha, J., Tellez, C., Santamaria, J. and Coronas, J. (2006). *Synthesis, characterization, and separation properties of Sn- and Ti-silicate umbite membranes.* Chemistry of Materials **18**(10), 2472-2479.

Sebastian, V., Lin, Z., Rocha, J., Tellez, C., Santamaria, J. and Coronas, J. (2008). *Improved Ti-silicate umbite membranes for the separation of H_2.* Journal of Membrane Science **323**(1), 207-212.

Sebastian, V., Lin, Z., Rocha, J., Tellez, C., Santamaria, J. S. and Coronas, J. (2005). *A new titanosilicate umbite membrane for the separation of H-2.* Chemical Communications(24), 3036-3037.

Seidel, A. and Carl, P. S. (1989). *The Concentration-Dependence of Surface-Diffusion for Adsorption on Energetically Heterogeneous Adsorbents.* Chemical Engineering Science **44**(1), 189-194.

Shao, L., Low, B. T., Chung, T. S. and Greenberg, A. R. (2009). *Polymeric membranes for the hydrogen economy: Contemporary approaches and prospects for the future.* Journal of Membrane Science **327**(1-2), 18-31.

Sips, R. (1948). *On the Structure of a Catalyst Surface.* Journal of Chemical Physics **16**(5), 490-495.

Skoulidas, A. I. and Sholl, D. S. (2001). *Direct tests of the Darken approximation for molecular diffusion in zeolites using equilibrium molecular dynamics.* Journal of Physical Chemistry B **105**(16), 3151-3154.

Skoulidas, A. I. and Sholl, D. S. (2002). *Transport diffusivities of CH_4, CF_4, He, Ne, Ar, Xe, and SF_6 in silicalite from atomistic simulations.* Journal of Physical Chemistry B **106**(19), 5058-5067.

Skoulidas, A. I., Sholl, D. S. and Krishna, R. (2003). *Correlation effects in diffusion of CH_4/CF_4 mixtures in MFI zeolite. A study linking MD simulations with the Maxwell-Stefan formulation.* Langmuir **19**(19), 7977-7988.

Slater, M. J. (1991). Principles of ion exchange technology. Great Britain, Butterworth-Heinemann.

Smit, B. and Maesen, T. L. M. (2008). *Molecular simulations of zeolites: Adsorption, diffusion, and shape selectivity.* Chemical Reviews **108**(10), 4125-4184.

Smith, T. G. and Dranoff, J. S. (1964). *Film diffusion-controlled kinetics in binary ion exchange.* Industrial & Engineering Chemistry Fundamentals **3**(3), 195-200.

Szostak, R. (1989). Molecular sieves principles of synthesis and identification. New York, Van Nostrand Reinhold.

Tavolaro, A. and Drioli, E. (1999). *Zeolite membranes.* Advanced Materials **11**(12), 975-996.

Taylor, R. and Krishna, R. (1993). Multicomponent mass transfer. New York, John Wiley & Sons, Inc.

Tiscornia, I., Irusta, S., Pradanos, P., Tellez, C., Coronas, J. and Santamaria, J. (2007). *Preparation and characterization of titanosilicate Ag-ETS-10 for propylene and propane adsorption.* Journal of Physical Chemistry C **111**(12), 4702-4709.

Tiscornia, I., Lin, Z., Rocha, J., Tellez, C., Coronas, J. and Santamaria, J. (2005). *Preparation of titanosilicate ETS-10 and vanadosilicate AM-6 membranes.* Molecular Sieves: From Basic Research to Industrial Applications, Pts a and B **158**, 423-430.

Treybal, R. E. (1981). Mass-transfer operations. Singapore, McGraw-Hill International Editions.

Trgo, M., Peric, J. and Medvidovic, N. V. (2006a). *A comparative study of ion exchange kinetics in zinc/lead - modified zeolite-clinoptilolite systems.* Journal of Hazardous Materials **136**(3), 938-945.

Trgo, M., Peric, J. and Medvidovic, N. V. (2006b). *Investigations of different kinetic models for zinc ions uptake by a natural zeolitic tuff.* Journal of Environmental Management **79**(3), 298-304.

Uhlhorn, R. J. R., Keizer, K. and Burggraaf, A. J. (1992). *Gas-transport and separation with ceramic membranes .1. Multilayer diffusion and capillary condensation.* Journal of Membrane Science **66**(2-3), 259-269.

Valverde, J. L., De Lucas, A., Carmona, M., Gonzalez, M. and Rodriguez, J. F. (2004). *A generalized model for the measurement of effective diffusion coefficients of heterovalent ions in ion exchangers by the zero-length column method.* Chemical Engineering Science **59**(1), 71-79.

Valverde, J. L., De Lucas, A., Carmona, M., Gonzalez, M. and Rodriguez, J. F. (2005). *Model for the determination of diffusion coefficients of heterovalent ions in macroporous ion exchange resins by the zero-length column method.* Chemical Engineering Science **60**(21), 5836-5844.

van de Graaf, J. M., Kapteijn, M. F. and Moulijn, J. A. (1998a). *Methodological and operational aspects of permeation measurements on silicalite-1 membranes.* Journal of Membrane Science **144**(1-2), 87-104.

van de Graaf, J. M., Kapteijn, M. F. and Moulijn, J. A. (1998b). Zeolitic membranes *Structured Catalysts and Reactors.* J. A. Moulijn and A. Cybulski. New York, Dekker.

van de Graaf, J. M., Kapteijn, M. F. and Moulijn, J. A. (1999). *Modeling permeation of binary mixtures through zeolite membranes.* AIChE Journal **45**(3), 497-511.

van den Broeke, L. J. P., Bakker, W. J. W., Kapteijn, F. and Moulijn, J. A. (1999a). *Binary permeation through a silicalite-1 membrane.* AIChE Journal **45**(5), 976-985.

van den Broeke, L. J. P., Bakker, W. J. W., Kapteijn, F. and Moulijn, J. A. (1999b). *Transport and separation properties of a silicalite-1 membrane - I. Operating conditions.* Chemical Engineering Science **54**(2), 245-258.

van den Broeke, L. J. P., Kapteijn, F. and Moulijn, J. A. (1999c). *Transport and separation properties of a silicalite-1 membrane: II. Variable separation factor.* Chemical Engineering Science **54**, 259-269.

van der Stegen, J. H. G., van der Veen, A. J., Weerdenburg, H., Hogendoorn, J. A. and Versteeg, G. F. (1999). *Application of the Maxwell-Stefan theory to the transport in ion-selective membranes used in the chloralkali electrolysis process.* Chemical Engineering Science **54**(13-14), 2501-2511.

Varshney, K. G., Gupta, P. A. and Tayal, N. (2003). *Kinetics of ion exchange of alkaline earth metal ions on, acrylamide cerium(IV) phosphate: A fibrous ion exchanger.* Colloids and Surfaces B-Biointerfaces **28**(1), 11-16.

Varshney, K. G. and Pandith, A. H. (1999). *Forward and reverse ion-exchange kinetics for some alkali and alkaline earth metal ions on amorphous zirconium(IV) aluminophosphate.* Langmuir **15**(22), 7422-7425.

Vignes, A. (1966). *Diffusion in binary solutions - Variation of diffusion coefficient with composition.* Industrial & Engineering Chemistry Fundamentals **5**(2), 189-199.

Wankat, P. C. (1994). Rate-controlled separations. Great Yarmouth, Blackie Academic & Professional.

Wesselingh, J. A., Vonk, P. and Kraaijeveld, G. (1995). *Exploring the Maxwell-Stefan description of ion-exchange.* Chemical Engineering Journal and the Biochemical Engineering Journal **57**(2), 75-89.

Wicke, E. and Kallenbach, R. (1941). *Die oberflachen diffusion von kohldioxid in aktiven kohlen.* Kolloid Z **97**, 135-151.

Xiao, J. R. and Wei, J. (1992a). *Diffusion mechanism of hydrocarbons in zeolites .1. Theory.* Chemical Engineering Science **47**(5), 1123-1141.

Xiao, J. R. and Wei, J. (1992b). *Diffusion mechanism of hydrocarbons in zeolites .2. Analysis of experimental-observations.* Chemical Engineering Science **47**(5), 1143-1159.

Xu, X. C., Bao, Y., Song, C. S., Yang, W. S., Liu, J. and Lin, L. W. (2005). *Synthesis, characterization and single gas permeation properties of NaA zeolite membrane.* Journal of Membrane Science **249**(1-2), 51-64.

Yang, M., Crittenden, B. D., Perera, S. P., Moueddeb, H. and Dalmon, J. A. (1999). *The hindering effect of adsorbed components on the permeation of a non-adsorbing component through a microporous silicalite membrane: The potential barrier theory.* Journal of Membrane Science **156**(1), 1-9.

Yang, R. T. (1987). Gas Separation by Adsorption Processes. USA, Butterworth Publishers.

Yardim, M. F., Budinova, T., Ekinci, E., Petrov, N., Razvigorova, M. and Minkova, V. (2003). *Removal of mercury (II) from aqueous solution by activated carbon obtained from furfural.* Chemosphere **52**(5), 835-841.

Yilmaz, B., Shattuck, K. G., Warzywoda, J. and Sacco, A. (2006). *Controlling crystal orientation in microporous titanosilicate ETS-4 films by secondary growth method.* Journal of Materials Science **41**(10), 3135-3138.

Yon, C. M. and Turnock, P. H. (1971). *Multicomponent Adsorption in Molecular*

Sieves. AIChE J. Symp. Ser **67**(117), 75-83.

Yu, M., Falconer, J. L., Noble, R. D. and Krishna, R. (2007). *Modeling transient permeation of polar organic mixtures through a MFI zeolite membrane using the Maxwell-Stefan equations.* Journal of Membrane Science **293**, 167-173.

Zah, J., Krieg, H. M. and Breytenbach, J. C. (2007). *Single gas permeation through compositionally different zeolite NaA membranes: Observations on the intercrystalline porosity in an unconventional, semicrystalline layer.* Journal of Membrane Science **287**(2), 300-310.

Zhang, F.-S., Nriagu, J. O. and Itoh, H. (2005). *Mercury removal from water using activated carbons derived from organic sewage sludge.* Water Research **39**, 389-395.

Zhu, W., Kapteijn, F. and Moulijn, J. A. (2000). *Adsorption of light alkanes on silicalite-1: Reconciliation of experimental data and molecular simulations.* Physical Chemistry Chemical Physics **2**(9), 1989-1995.

Zhu, W., van de Graaf, J. M., van den Broeke, L. J. P., Kapteijn, F. and Moulijn, J. A. (1998). *TEOM: A unique technique for measuring adsorption properties. Light alkanes in silicalite-1.* Industrial & Engineering Chemistry Research **37**(5), 1934-1942.

Zhu, W. D., Hrabanek, P., Gora, L., Kapteijn, F. and Moulijn, J. A. (2006). *Role of adsorption in the permeation of CH_4 and CO_2 through a silicalite-1 membrane.* Industrial & Engineering Chemistry Research **45**(2), 767-776.